Universität Bremen

Fachbereich 1
Physik / Elektrotechnik

Institut für Biophysik

Dynamics of Morphological Cell States

Dissertation zur Erlangung des akademischen Grades
Doktor der Naturwissenschaften
(Dr. rer. nat.)

Malte Ohmstede, M. Sc.

Betreuer & Erstgutachter:	Prof. Dr. Hans-Günther Döbereiner
Zweitgutachter:	Prof. Dr. Joachim Rädler

Eingereicht am:	21.07.2023
Verteidigt am:	28.09.2023

"Science knows no country, because knowledge belongs to humanity, and is the torch which illuminates the world."

– Louis Pasteur

Abstract

Cellular proliferation greatly depends on the intake of extracellular material. One very distinct method of such endocytosis is a process known as macropinocytosis. During this process, large circular waves of newly polymerized actin form into cup-like, three dimensional structures, protruding the cellular membrane upwards from the lamellipodium. Such structures are known as Circular Dorsal Ruffles (CDRs).

These transient and dynamic rings of intense actin polymerization typically last for several minutes and span over diameters in the micrometer range. Upon finalization of the structure, recruited motor proteins facilitate a contraction of the upper rim, enclosing material inside of the structure in a large vesicle of cellular membrane.

Stimulation of cells to express these CDRs is facilitated by exposing cells to so-called growth factors. These growth factors trigger a signaling cascade within the cell, leading to recruitment of several key proteins involved in actin polymerization to assemble into the aforementioned circular shape.

In this thesis, the focus will be laid on how the expression of CDRs depends on the concentration of added growth factors and how individual cells react to such stimuli. As will be shown, a primary effect of increased stimulant concentration is a trend towards expression of longer lasting, less motile CDRs. The effect of stimulation on individual cells actively expressing CDRs is, counterintuitively, a reduction in CDR activity, while previously inactive cells are stimulated to begin expressing CDRs as would be expected. Here, the amount of live single cell data acquired during the study plays an important role in identification of such patterns due to the large variance of cellular processes inherent to biological systems, as well as the inability to determine protein concentrations within cells during experiments.

A crucial consideration for performed experiments was generation of large datasets per experiment. This was facilitated by utilizing a microfluidic perfusion system in conjunction with microcontact printing, forcing cells into predetermined shapes an locations on the provided substrate. These methods in combination with usage of sophisticated image processing algorithms allowed for extraction of a dataset of significant size. Usage of statistical methods such as clustering, allowed for deeper insights into behavior of cells and yielded similarities of cellular behavior to excitable reaction-diffusion systems.

Contents

List of Figures

List of Tables

Acronyms

ADP Adenosine diphosphate. 12
Arp Actin Related Protein. 11, 13, 14, 20
ATP Adenosine triphosphate. 12

CDR Circular Dorsal Ruffle. viii, 4–9, 11, 12, 14, 15, 17–21, 23–29, 35, 41, 42, 47, 50, 51, 54, 55, 65–77, 79–85, 87–90, 94, 95, 103–106, 116
CLI Command Line Interface. 101, 102
CNN Convolutional Neural Network. 55, 94, 103, 106
CPU Central Processing Unit. 58
CSV Comma Separated Values. 98

DGVF Directional Gradient Vector Flow. 56, 57
DIC Differential Interference Contrast. 51
DMEM Dulbecco's Modified Eagles Medium. 41, 45, 47, 49, 58, 59, 83, 94, 109, 110
DOI Digital Object Identifier. 97

ECM Extracellular Matrix. 42
EGF Epidermal Growth Factor. 19

FBS Fetal Bovine Serum. 41, 79
FDO FAIR Digital Object. 97
FFT Fast Fourier Transform. 54
FHN FitzHugh-Nagumo. 7, 24–26, 28
FN Fibronectin. 4, 41, 42, 51, 54, 79, 87, 102, 110, 111
FOV Field of View. 51, 94, 102

GAP GTPase-Activating Protein. 13
GDI Guanine Nucleotide Dissociation Inhibitors. 13
GDP Guanosine diphosphate. 13
GEF Guanine Nucleotide Exchange Factor. 13
GPU Graphics Processing Unit. 58, 95
GTP Guanosine triphosphate. 13
GUI Graphical User Interface. 101–104
GVF Gradient Vector Flow. 55–57

HDF5 Hierarchical Data Format 5. 101, 102, 104–106
HGF Hepatocyte Growth Factor. 19
hPDGF Human Platelet Derived Growth Factor. viii, 6–8, 19, 25, 42, 47, 48, 50, 58, 59, 65–75, 79–86, 88, 89, 112–115

PBS Phosphate Buffered Saline. 109, 110, 112
PC Phase Contrast. 51, 56
PCA Principal Component Analysis. 59, 60, 79–81
PDMS Polydimethylsiloxane. 51, 110, 111
PIP_2 Phosphatidylinositol (4,5)-bisphosphate. 14, 20
PIP_3 Phosphatidylinositol (3,4,5)-trisphosphate. 14, 19, 20, 24, 26
PLL-g-PEG Poly-L-Lysine graft Poly Ethylene Glycol. 42, 110–112
PTFE Polytetrafluoroethylene. 43, 44

ROI Region of Interest. 54, 102

RTK Receptor Tyrosine Kinase. 14, 15, 19–21, 66, 88

WASP Wiskott-Aldrich Syndrome Protein. 13

ZVI Zeiss Vision Image. 101, 102, 104, 106

Acknowledgements

I would like to thank **Prof. Dr. Hans-Günther Döbereiner** for supervising my work, giving me a great amount of freedom to experiment and come up with ideas, as well as support and guidance when needed. The many discussions pushed me into the right directions and made me learn many new things.

I would also like to thank **Prof. Dr. Joachim Rädler** for being the second examiner of this thesis.

Special thanks go to the current and former members of the Döbereiner Lab. Especially **Erik Bernitt**, who drew me into the subject of circular dorsal ruffles during early studies played a big role in learning how to evaluate microscopy images using a computer. I thank **Christina Oettmeier, Adrian Fessel, Julia Lange, Merthe Schwachenwald, Anna Maria Piorecka-Ecken** and **Jonghyun Lee** for always being open to discuss topics related or unrelated to work. Without the help of **Anja Bammann** in the laboratory, most of this work would not have been possible. This is, of course, not excluding all other current and former colleagues at the Biophysics Institute in Bremen whom I thank for being the friendly and open people that they are, especially **Shruti Kulkarni**, since we both helped each other to keep up our spirits while writing at the same time.
I would like to thank my family, especially my parents, for always supporting me in pursuing my goals.
Very special thanks go to my elderly dog, Lotte, who always forced me to go out and get some fresh air and increased my dopamine levels by demanding to be pet while I was working from home. Especially during the final writing phase of the thesis she always managed to lift my spirits at the right times.

Part I

Introduction

Chapter 1

Introduction

Eucaryotic cells rely on various mechanisms to take up extracellular material. Sophisticated proteins embedded into the plasma membrane function as a control of what material can enter the cell and what remains outside (Alberts et al., 2015). Some of these proteins act as a controlled channel for ions to enter the cell — one prime example of this function are the voltage gated ion channels in neurons — others trigger vast signaling cascades within the cell, when activated with the proper ligand (Alberts et al., 2015; Hoon, Wong, and C.-G. Koh, 2012). This list is, however not complete and many other ways of endocytosis exist.

An example of such a mechanism relying on a complex signaling protein network is the so-called "Macropinocytosis", which was first observed by Warren Lewis in 1931 when he inspected time-lapse film micrographs of an adherent macrophage cell culture (King and Robert R. Kay, 2019). Lewis initially named this process "Pinocytosis", a word creation from neo-latin involving the term "pino" meaning "to drink", however it was later renamed to the aforementioned term Macropinocytosis. This mechanism facilitates intake of large amounts of extracellular fluid into the cell. Internalization is hereby performed, by forming a ring-shaped actin structure which pushes the cellular plasma membrane upwards into a cup (Gerisch et al., 2009). This cup is then closed at the top by recruiting motor proteins to the rim of the cup and triggering a contraction of it, which subsequently creates a vesicle of extracellular fluid engulfed by the plasma membrane (Swanson, 2008). This vesicle is then transported towards the nucleus and finally broken down in order to utilize the content for cell proliferation.

Crucial proteins involved in the signaling cascade leading to the formation of such actin rings will be presented in Chapter 2. A large amount of proteins involved in general regulation of the actin cytoskeleton is involved in macropinocytosis and locally accumulates in a circular shape. How this circular shape is formed in detail is, however, not yet well understood, as will be further discussed in Section 1.1 and the following chapters investigating the cytoskeleton and actin waves.

The underlying phenomenon creating the aforementioned cup are circular actin waves on the cellular lamellipodium (Buccione, Orth, and M. a. McNiven, 2004; Hoon, Wong, and C.-G. Koh,

2012). These ring-shaped actin waves, which protrude vertically from cells are also known as CDRs,[1] and are the main research target of this thesis. These actin rings typically protrude multiple micrometers upwards from the cell, span many micrometers in diameter and last for several minutes before they close and create the aforementioned vesicle (King and Robert R. Kay, 2019; Swanson, 2008). Figure 1.1 shows a simplified sketch of the cross section of a CDR. As

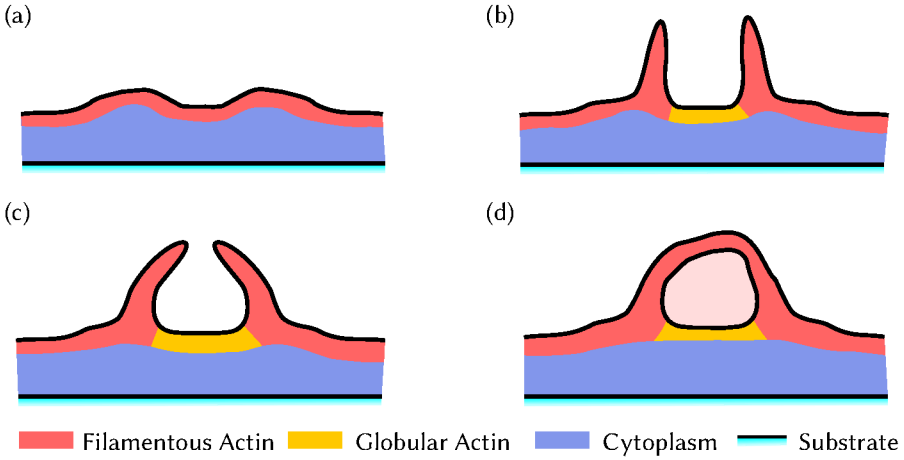

Figure 1.1: Sketch of steps involved in a CDR protruding out of the cell surface and collapsing into a large vesicle. (a) Initialization process of ruffle formation. (b) Fully protruding actin structures pushing the membrane upwards from the dorsal side of the cell. The inside of the CDR surrounded by the actin protrusions displays a significantly lower concentration of filamentous actin than the surrounding. (c) Collapsing of the protrusions, bowing towards the inside of the CDR. (d) Formation of a vesicle by joining the cellular membrane around the enclosed extracellular material.

will be described in Chapter 3, the function of CDRs is not solely the creation of large vesicles. During the process, the actin cytoskeleton is rearranged and membrane bound receptors are internalized (Hoon, Wong, and C.-G. Koh, 2012; Lyashenko et al., 2020). This internalization of receptors is used by the cell in order to reduce sensitivity to external stimulation by, e.g. growth factors (Lyashenko et al., 2020). Since fibroblasts react to such stimuli with increased proliferation and motility during wound healing it is desirable by the organism to regulate the rate of response in order to prevent uncontrolled cellular growth (Pierce et al., 1991).
Figure 1.2 shows a typical time-lapse of a CDR expressed by a cell spread into a pre-determined shape controlled by a stamped circular Fibronectin (FN) micropattern, which will be briefly introduced in Section 1.4 and be explained in more detail in Section 6.2. Clearly visible is the formation of the ring, movement on the cellular lamellipodium, contraction and closure. The formed vesicle is then visible as a bright spot within the cell. As is visible from the dimensions of the CDR, the vesicles formed during this process are comparatively large in volume, with diameters in the micrometer range, rather than nanometers as is typically found in endosomes (King and Robert R. Kay, 2019).

[1] Here the term "dorsal" describes that the protrusion is located on non substrate-facing side of the cell.

Such circular actin based structures and the process of macropinocytosis is found in a vast number of organisms and cell types, which will be further discussed in Section 1.2. A brief introduction into the possibilities of modeling actin rings will be given in Section 1.3. More insight into the current state of research on CDRs will be presented in Section 1.1.

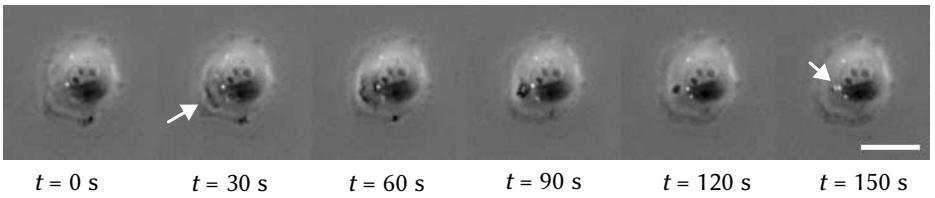

Figure 1.2: Typical timeline of a CDR (location indicated with white arrow in second frame) forming and collapsing over the course of several minutes. The actin ring expands and is reflected by the leading edge of the lamellipodium, as well as the nucleus. After this reflection, the ring contracts and collapses into a large vesicle, indicated by the white arrow in the last frame. Scale bar: 30 µm

State of Research on Circular Dorsal Ruffles 1.1

As already mentioned above, the phenomenon of CDRs was first described by Warren Lewis in 1931 when he discovered it playing a crucial part in a process he coined Pinocytosis which he discovered by means of time-lapse films of macrophages (ibid.). Mellström, Heldin, and Westermark showed in 1988 that CDRs can be stimulated in human foreskin fibroblast cells by adding platelet derived growth factor to the cell medium.

For a long time there was very little progress in reasearch on the phenomenon, however since the early 2000s research has taken up pace. As will be discussed in Section 1.2, CDRs have been observed in increasing numbers of celltypes and amoeboid organisms. Key proteins in the cellular actin regulation pathway were shown to be closely involved in CDR formation. Among those, many actin nucleation factors — will will be further discussed in Section 2.2.1 — Rho-Gtpases — see Section 2.2.2 — and phosphoinositides — Section 2.2.3 — were found to play major roles in the process (Egami et al., 2014; Gerisch et al., 2009; Suetsugu et al., 2003).

Extensive research on the growth factor mediated, receptor triggered signaling pathways involved in the formation of CDRs has provided deeper insights into how cells regulate their actin cytoskeleton in response to external stimuli (Buccione, Orth, and M. a. McNiven, 2004; Hoon, Wong, and C.-G. Koh, 2012; Robert R Kay, Williams, and Paschke, 2018).

Further work on non-circular actin waves uncovered such waves to be deeply ingrained mechanisms in cell functions. Actin waves were shown to play major roles in cell migration, polarization and growth in many different cell types (Allard and Alex Mogilner, 2013; Inagaki and Katsuno, 2017; Ruthel and Banker, 1998; Vicker, 2002). Additionally, recent research showed that cells use this process for regulation of sensitivity to these external stimuli (Lyashenko et al., 2020).

The possibility of modeling actin waves using reaction-diffusion systems was discovered with early models by Zeng et al. (Zeng et al., 2011). Bernitt et al. showed that many aspects of CDR dynamics in particular can be simulated using such models (Bernitt and Döbereiner, 2017; Bernitt, C. G. Koh, et al., 2015). This approach was further refined and resulted in a mass conserving bistable model, depending on the total amount of actin (Bernitt, Döbereiner, et al., 2017). Work by Julia Lange confirmed various CDR expression behaviors predicted by the model through reducing the amount of actin available to a cell and comparing results to numerical simulations (Lange, 2019).
Recently, CDRs have been observed in kidney tissue of glomerular podocytes for the first time, ensuring that this phenomenon is indeed present in-vivo and not an artifact of cell culture (Hua et al., 2023).

1.2 Circular Actin Waves in Various Organisms

Multiple different celltypes have been observed expressing CDRs, among which the macrophages are most prominent. Other cell types include fibroblasts, differentiated epithelial cells and, as a recent addition, glomerular podocytes (ibid.). This list is certainly not complete. Essentially, most mammalian cells are able to express CDRs given the proper stimulus (King and Robert R. Kay, 2019).
The model organism used in this thesis are murine embryonic fibroblasts of the line NIH3T3, which is a well established cell line, abundantly available in most biological laboratories and rather robust in cell culture. Fibroblasts are also proven to respond well to stimulation using hPDGF by expressing CDRs, which was initially shown on human foreskin fibroblasts, and later on the used NIH3T3 cell line (Mellström, Heldin, and Westermark, 1988; Zeng et al., 2011).
Extensive research on CDRs is also present in the amoeboid slime mold *Dictyostelium discoideum* (Gerhardt et al., 2014; King and Robert R. Kay, 2019; Swanson, 2008). Since slime molds form their own branch in the phylogenetic tree, separated from mammals, the process of macropinocytosis is thought to have existed at the point of branching, rendering it a very ancient cellular process (King and Robert R. Kay, 2019). Another possible explanation, without any data to back it up and only mentioned here for completeness, would be convergent evolution. However, the usage of the process is too deeply involved in cellular proliferation making it more likely that macropinocytosis evolved early in single cellular organisms.
Macropinocytosis also occurs in many more single celled organisms, including pathogenic ones. Examples for such amoeboid organisms are *Acanthamoeba castellanii* or *Entamoeba histolytica* (Meza and Clarke, 2004; Ostap et al., 2003).
Since cancerous cells, notably Ras-activated tumor cells, were observed to excessively express CDRs, macropinocytosis is thought to be an ancient amoeboid feeding pattern still present in most eukaryotic cells (Bloomfield and Robert R. Kay, 2016). It is suspected in literature, that some cancer cells return to amoeboid feeding patterns in order to proliferate, since this makes them less dependent on the functions of the host organism.

Modeling of Actin Rings 1.3

A large quantity of proteins is involved within the cell in order to form such actin rings, however the complex orchestration of the formation of large ring-shaped actin structures is not yet well understood. An insight into the involved proteins and signaling cascade will be presented in Chapter 3.

Many different properties of CDR expression in cells have been observed in simplified mathematical models such as reaction-diffusion systems. Reaction-diffusion systems have been found to express various characteristics from stable patterns — first shown by Alan Turing (1952) — to traveling waves. As will be discussed in Chapter 4 and especially Section 4.2, aspects of CDRs formation can be described using the FitzHugh-Nagumo (FHN) model (FitzHugh, 1961; Nagumo, Arimoto, and Yoshizawa, 1962), which was shown to be applicable by Bernitt, C. G. Koh, et al. (2015). The FHN model was originally developed to model action potentials in neurons and is therefore not ideal to monitor the complex behavior of actin polymerization. Other modeling approaches exist in literature building on various characteristics of experimental data on CDR formation.

A very specialized bistable reaction-diffusion model, specifically formulated for CDR building on experimentally found asymmetries on the inside and outside of CDRs has been proposed by Bernitt, Döbereiner, et al., 2017, and will be discussed in Section 4.3.

Research Strategy and Aims 1.4

In order to investigate the stimulation characteristics of CDRs in NIH3T3 fibroblast cells, extensive experiments on stimulation of actin waves using hPDGF have been carried out. In order to generate data of single cells in controlled morphologies, a technique called microcontact printing (Bernitt, C. G. Koh, et al., 2015; Théry and Piel, 2009) was used, which is more extensively described in Section 6.2. Figure 1.3 shows how fibroblasts adapt to such circular microcontacts (b) as compared to how they typically spread on a substrate (a). The most striking difference is the uniformity of lamellipodial width in subfigure (b), which greatly improves analysis of CDR motility by providing a quasi one-dimensional path for CDRs to propagate on, since they are reflected by the cell edge and the nucleus as will be introduced in Section 3.2. Since fibroblast cells spreading randomly often contract into elongated shapes with minimal lamellipodium area after the initial spreading phase, this setup allows for longer experiments with greatly increased data output by having more cells in a desirable morphology.

Despite the fibroblast cells not being in their typical morphology, previous research showed no significant difference between randomly spread cells and those spread onto microcontacts and has since been extensively used in the workgroup (Bernitt, C. G. Koh, et al., 2015). The experimental setup used here was tuned towards being able to precisely reproduce the timing of adding a stimulus to the cells using a microfluidic perfusion system. This system, which will be further described in Section 6.3, is able to be programmed for executing multiple consecutive

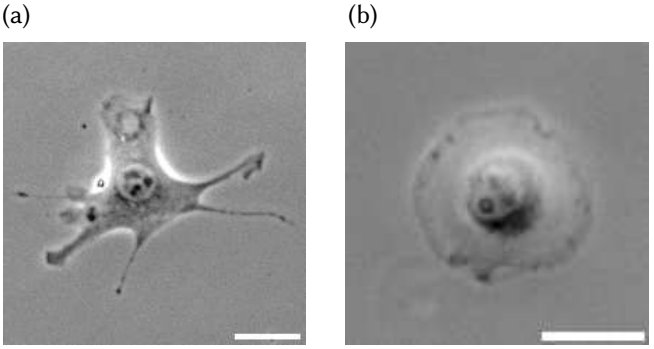

Figure 1.3: Comparison between NIH3T3 fibroblasts spread (a) randomly and (b) on a printed circular substrate with an area of 3000 µm^2. The randomly spread cell in (a) displays a large variation in lamellipodium area available for CDR formation, which greatly varies for each individual cell. The controlled circular shape in (b) aims to provide homogeneous width of the lamellipodium. Scale bars in both subfigures: 30 µm

experiments with the same parameters such as stimulation time, flow rate and recovery times. In contrast to classical stimulation experiments, where the medium is manually replaced using pipettes, this method enables uninterrupted imaging of cells during the entire course of the experiment.
Using this setup, a large amount of single cell data was obtained from experiments. Overall, the number of individual cells analyzed is **2548** with **16 663** CDR events among them. This unprecedented large number of datapoints for this kind of experiment allows for deeper insights into how growth factor stimulation with hPDGF affects cells.
By using statistical methods like cluster analysis and principal component analysis, see Section 6.6, several patterns in cellular dynamics and CDR dynamics were identified and investigated. One major result here is that CDR expression patterns are dependent on the concentration of the external stimulant.

1.5 Outline of the Thesis

The outline of this thesis is split up into four parts. In the introduction part, general and more detailed concepts closely related to the investigated CDRs are presented or reiterated. Split up into their own respective chapters are the actin cytoskeleton in Chapter 2, actin waves in Chapter 3, reaction-diffusion systems in Chapter 4, microfluidics in Chapter 5, as well as a more general presentation of used materials and methods found in Chapter 6.
The second part covers the experimental results, split up into three chapters. Chapter 7 covers a more general approach to how cells react to stimuli, by investigation whether individual cells express CDRs or not after an added stimulus. In Chapter 8, CDRs themselves are inspected in more detail, as to how added growth factors affect duration and traveled distance. A more detailed approach to how individual cells react to hPDGF stimulation is performed in Chapter 9.

Here, each cell is characterized by CDR expression patterns for a certain timeframe by deeper multidimensional statistical analysis. Lastly, Chapter 10 covers a conclusion of the previous result chapters.
The outlook part provides an outlook into possible future experiments for building upon the results obtained during this thesis. Additionally, the role and importance of well documented, open data structures is discussed and why it is deemed important for advancing research on phenomena requiring vast datasets for increasingly accurate results.
Finally, in the appendix, many of the methods introduced in Chapter 6 are discussed in more detail concerning their implementation for the performed data analysis. In addition to this, laboratory protocols, used software and more details on the obtained dataset are presented.

Chapter 2

The Cellular Cytoskeleton

Actin is the most abundant and most well preserved proteins within all cells (Kabsch and Vandekerckhove, 1992). Cells utilize actin not only for their internal structure, i.e. the cytoskeleton, but also for active transport within the cell by attaching motor proteins like myosin to vesicles in order to be transported along long polymerized actin filaments or microtubules. In the scope of this thesis, the fact that the investigated CDRs are actin based makes it vital to reiterate the properties of actin and closely related regulating proteins (Buccione, Orth, and M. a. McNiven, 2004).

As will be described in this chapter, actin is present in it's monomeric globular form or in polymerized form as actin filaments, Section 2.1. Cells are able to orchestrate controlled and directed polymerization of actin filaments through various actin related proteins and signaling pathways, a relevant selection of these will be introduced in the corresponding sub sections of Section 2.2. This controlled polymerization and depolymerization is readily used by cells to reorganize their shape or, in the case of CDRs or lamellipodia, form motile membrane protrusions at specific sites.

Facilitation of membrane protrusions is performed by actin filaments exerting forces on the membrane, described in Section 2.4, hence deforming it. Since single filaments are very thin structures, they are typically assembled into bundles or mesh networks, see Section 2.3. Formation of meshes is performed by proteins like the Actin Related Protein (Arp) 2/3 complex, which can be incorporated into growing filaments, creating branching points for a complimentary filament starting to grow at their location, branched off by an angle of 70° from the initial filament (Mullins, Heuser, and Pollard, 1998).

These actin networks gain additional stability by cross linking single filaments using specific actin binding proteins like filamin or α-actinin which greatly improves stiffness of the actin network (Blanchoin et al., 2014).

2.1 Actin

Actin is the most abundant protein in eukaryotic cells with single cells being estimated to contain 150 µM of globular actin, i.e. monomeric actin, as well as 500 µM of filamentous actin (Koestler et al., 2009). These two different forms of actin are used by the cell to give itself structure.
The basic subunit of actin, called globular actin, or short g-actin, is a 375 amino acid polypeptide (Alberts et al., 2015, p. 898). Each g-actin molecule carries an Adenosine triphosphate (ATP) or Adenosine diphosphate (ADP) molecule, depending on phosphorylation status. The actin molecule has two distinct ends, the plus (also called barbed) end and the minus (also called pointed) end. The phosphorylated monomers carrying an ATP molecule are joined upon polymerization with different rates on the two different ends, where the plus end is faster growing than the minus end (ibid.), with the ATP being hydrolyzed in the process. The individual subunits polymerize in the fashion of joining opposing ends, forming a long polymer which is known as filamentous actin.
The polymerized form of actin is called actin filaments or filamentous actin — short: f-actin. De novo polymerization of individual filaments requires stabilized polymerization nuclei, manufactured by nucleation promoting factors which will be further described in Section 2.2.1. After nucleation, growth of individual filaments happens, as mentioned above, by free actin monomers attaching to the plus or minus end of the filament. With the rate of growth being higher at the plus end, filaments will grow faster on the plus end than on the minus end. This process of constant polymerization on one end and depolymerization on the other end is also referred to as treadmilling (ibid.). Given an availability of free g-actin, filaments will continue to grow until capping proteins bind to the barbed end of the filament, terminating the elongation process. Among these capping proteins, two different classes can be identified. Such proteins either sever and cap the filament, examples for this type are Gelsolin and Severin, or only cap the filament without severing, like CapZ (Carlier and Pantaloni, 1997).
Ensuring filament growth by avoiding capping of growing filaments is regulated by so-called elongation factors, such as formins or Ena/VASP (ibid.).

2.2 Proteins and Lipids involved in Actin Regulation

Since the actin cytoskeleton is an essential part of the cell, a large number of proteins are playing crucial roles in the regulation of actin filament assembly and cross linking into meshworks which will be described in Section 2.3. In this section and the following sub sections, a selection of key proteins closely involved in CDR formation will be presented in order to provide context on the regulatory network underlying the process.

2.2.1 Actin Nucleation Factors

In order to prevent uncontrolled formation of actin filaments in the cell, the proteins profilin and β-thymosin bind to actin monomers in order to inactivate them , rendering the g-actin incapable

of spontaneous polymerization, which in turn enables the cell to utilize actin nucleators to trigger controlled de novo formation of filaments (Blanchoin et al., 2014; Chesarone and Goode, 2009). Among these nucleators exist different types, which trigger a variation of filament growth modes. Linear growth is triggered by, e.g., formins, whereas branched growth is heavily influenced by the Arp2/3 complex (Rottner et al., 2017). The Arp2/3 complexes enable creation of new filaments at an angle of 70° to the existing filament which generates an actin meshwork (Mullins, Heuser, and Pollard, 1998). The meshwork will be described in more detail in Section 2.3.
In order for Arp2/3 to facilitate this branching, it is activated by nucleation promoting factors from the Wiskott-Aldrich Syndrome Protein (WASP)/WAVE family, such as WASP, N-WASP, WAVE1, WAVE2 and WAVE3, which link the upstream regulatory signaling cascade to to the actin cytoskeleton (Higgs and Pollard, 1999; Mullins, Heuser, and Pollard, 1998). A selection of such upstream signals will be presented in Sections 2.2.2 and 2.2.3.

Rho GTPases 2.2.2

An important family of proteins in the signaling cascade of actin polymerization within cells are the small Rho GTPases, where Rho is an abbreviation for **R**as **ho**mologue, which form a subgroup of the Ras family (Egami et al., 2014). These Rho GTPases regulate a multitude of processes in eukaryotic cells, with the most relevant ones in the scope of this work being actin polymerization and actin filament bundling in response to extracellular stimuli (Dam, Bos, and Snel, 2011). Three of the best studied members of the Rho GTPase family are Rho, Rac and Cdc42. Rho regulates the formation of focal adhesions and stress fibers which are used by the cell for attachment to substrates, Rac regulates formation of lamellipodia and membrane ruffles and Cdc42 regulates very thin actin structures calles filopodia (ibid.). The Rho GTPases are not only regulated by upstream signaling events, but also regulate each other, where Cdc42 can activate Rac and Rac can activate Rho (Van Aelst and D'Souza-Schorey, 1997).
Regulation of Rho GTPases closely depends on binding of Guanosine diphosphate (GDP) and Guanosine triphosphate (GTP), where a GDP bound state can be referred to as an inactive state and a GTP bound state as an active state. Activation and deactivation of Rho GTPases is closely controlled by different types of regulatory proteins, such as Guanine Nucleotide Exchange Factors (GEFs), GTPase-Activating Proteins (GAPs) and Guanine Nucleotide Dissociation Inhibitors (GDIs) (Boguski and McCormick, 1993; Van Aelst and D'Souza-Schorey, 1997). The function of GEFs is to activate GTPases by increasing the exchange of bound GDP to GTP, with GAPs increasing the rate of hydrolization of GTP to GDP. Spontaneous turnover of GTP binding GTPases by GAP is closely regulated by GDI which inhibits GAP (Van Aelst and D'Souza-Schorey, 1997).

Phosphoinositides 2.2.3

Phosphoinositides are a family of lipids that play a key role in signal transduction pathways from activated membrane receptors (Balla, 2013). Overall, seven different forms of phosphoinositides

can be found with a variation of phosphorylation states, however the ones most closely involved in the processes to be investigated here are Phosphatidylinositol (4,5)-bisphosphate (PIP_2) and Phosphatidylinositol (3,4,5)-trisphosphate (PIP_3), with PIP_2 being more abundant than the latter (Balla, 2013; King and Robert R. Kay, 2019).
Phosphoinositides are accumulated at the cell membrane and are closely involved in actin regulating signaling cascades (Balla, 2013). PIP_2 in combination with Cdc42 is used to trigger actin polymerization by binding N-WASP, which in turn causes an increase in Arp2/3 recruitment and therefore formation of actin meshworks (Di Paolo and De Camilli, 2006). Upon stimulation with growth factors and consequent activation of Receptor Tyrosine Kinases (RTKs), PIP_2 is increasingly phosphorylated to PIP_3, where turnover of PIP_2 to PIP_3 is regulated by the signaling protein PI3k, while the inverse turnover from PIP_3 to PIP_2 is regulated by PTEN (King and Robert R. Kay, 2019).
Due to their key role in the actin signaling network, phosphoinositides are proven to be closely involved in CDR formation, where it has been observed that there is an intense patch of PIP_3 at the inside of CDRs in both *Dictyostelium discoideum*, as well as mammalian cells (ibid.). This asymmetry of local PIP_2 and PIP_3 concentrations was part of the basis for the bistable reaction-diffusion model proposed by Bernitt, Döbereiner, et al., 2017, which will be introduced in Section 4.3.

2.3 Actin Meshwork

Within the cell, actin filaments are rarely isolated singular filaments, but are organized into bundles or a mesh, giving them additional rigidity as compared to a singular filament. This mesh is generated by multiple cross-linked actin filaments overlaying each other. Proteins such as the Arp2/3 complex are incorporated into single actin filaments and serve as a branching point for a newly polymerized actin filament to form at an angle of 70° from the initial filament (Borisy and Svitkina, 2000). This section will focus on the actin meshwork as it makes up the walls of macropinocytotic cups or CDRs with increased concentrations of Arp2/3 being present at those locations (King and Robert R. Kay, 2019).
With newly formed actin meshwork pushing the membrane upwards from the cell surface, a cup is formed which then encloses extracellular material and is closed by recruitment of myosin motor proteins at the rim which then facilitate contraction of the cup into a closed structure (Swanson, 2008). In order to push the membrane upwards, the newly polymerized actin filaments need to exert forces on the membrane, as will be described in Section 2.4.
By organizing the filaments into a mesh, the cytoskeleton is able to generate a higher forces than by using single filaments. An actin network like this is additionally supported and strengthened by cross linking single filaments. Cross linking is done by specific proteins, linking actin filaments at different lengths by binding to different actin filaments. These ranges span from fimbrin with a range of 10 nm to filamin with a range of 160 nm (Blanchoin et al., 2014). Large

crosslinkers like filamin or α-actinin are present in actin bundles, as well as mesh networks (ibid.).

Force Generation of Actin Filaments 2.4

Actin filaments are able to exert forces on the cell membrane (A. Mogilner and G. Oster, 1996; Alex Mogilner and George Oster, 2003; Peskin, Odell, and G. F. Oster, 1993). The mechanism behind these forces was first described by Peskin, Odell, and G. F. Oster (1993) as a "Brownian ratchet", however more recent work by A. Mogilner and G. Oster (1996) found the initial proposal to be lacking in it's ability to deform the membrane. Through modifications to the initially proposed model, they described the dynamic Brownian ratchet.

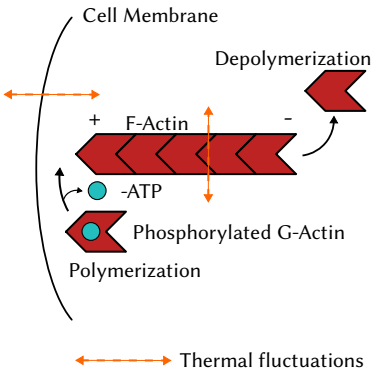

Figure 2.1: Sketch of the working principle of the elastic Brownian ratchet for force generation from actin filaments.

The Brownian ratchet,as introduced by Peskin, Odell, and G. F. Oster (1993), is a system which relies on thermal fluctuations of the cellular membrane. These fluctuations enable globular actin to be attached to the pointed end of an actin filament pushing against the membrane. By polymerizing the filament towards the membrane, an effective force is generated which pushes the membrane outwards. A. Mogilner and G. Oster (1996) showed that fluctuations of the membrane alone are not sufficient for generating the required forces. In their model called "elastic Brownian ratchet", see sketch in Figure 2.1, they assume both the membrane and the actin filament to thermally fluctuate. This combined elastic fluctuation is shown to be able to generate forces sufficiently large for propagating the membrane outwards. Experimental measurements of the stall force of a keratocyte lamellipodium using a microneedle setup determined this force to be approximately 45 nN (Oliver, Dembo, and Jacobson, 1995; Oliver, Lee, and Jacobson, 1994).

Membrane bound actin nucleation factors impact polymerization rates of actin filaments at the leading edge of the lamellipodium or ruffle (Borisy and Svitkina, 2000). In order to achieve directed growth of membrane protrusions, these membrane attached proteins are needed locally to increase f-actin polymerization rates into a given direction. For the case of lamellipodia, this direction can be induced by, e.g. chemotaxis influencing the actin polymerization pathway, causing the cell to move along a chemical gradient. In the case of CDRs, the activated RTKs trigger a higher concentration of the required proteins to be present where the CDR will form, as will be further discussed in Section 3.2.2. Each single filament exerts a small force and can easily be bent due to opposing forces from, e.g. membrane tension, however, the actin mesh described in Section 2.3 as a whole is able to sufficiently deform and move the membrane (ibid.).

Chapter 3

Actin Waves

Actin waves are a large scale phenomenon observed in cells during multiple cellular processes, such as motility or macropinocytosis and can be observed in spreading, migrating or stationary cells (Allard and Alex Mogilner, 2013). These wave like alterations of the actin cytoskeleton differ greatly in length-scale from the typically observed actin treadmilling described in Section 2.1. The general concept of actin waves is presented in Section 3.1. These large actin structures are employed for various different functions within cells, spanning from endocytosis to cell polarization and reorganization of the cytoskeleton. Since such waves utilize the actin which is locally present in the cell in a short timeframe, previously present actin based structures, like stress-fibers and many other general parts of the cytoskeleton, have to be broken up for waves to be able to form. This assumes the total amount of actin to be constant during this timeframe, which is too short for actin synthesis to make any crucial difference (Bernitt, Döbereiner, et al., 2017).

This thesis focuses on a special kind of actin waves, so called Circular Dorsal Ruffle (CDR), which are circular membrane protrusions forming, as the name suggests, on the dorsal side of adherent cells and are further introduced in Section 3.2. They play a crucial role in a process called macropinocytosis, which facilitates large scale internalization of external material into the cell and is a phenomenon observed in unicellular, as well as multicellular organisms and is proposed to stem from amoeboid feeding patterns (King and Robert R. Kay, 2019).

The stimulation dynamics underlying the formation of CDRs will be outlined in Sections 3.2.1 and 3.2.2. Here, stimulation of CDRs via growth factors is presented with a simplified form of the underlying signaling cascade involved after activation of receptors on the cell surface. Despite the underlying signaling cascade being known, the actual protein kinetics involved in forming this comparatively large ring of guided actin polymerization remains unknown and is expected to be related to reaction-diffusion systems, which will be introduced in the next chapter.

3.1 Traveling Actin Waves

Large scale actin waves play a crucial role in cell movement and differ greatly from more passive cell movement induced by treadmilling of the actin machinery (Allard and Alex Mogilner, 2013). These actin waves, travel across the cell as alterations of the actin cytoskeleton at larger length scales (Allard and Alex Mogilner, 2013; Inagaki and Katsuno, 2017). Such wave-like patterns of the actin machinery are observed in spreading, migrating, as well as stationary cells, which implies this process to not only being useful for actively migrating cells, but also for already stationary cells which need to actively reorganize their cytoskeleton (Allard and Alex Mogilner, 2013).
A prime example of very large scale actin waves can be found in cells exhibiting phagocytotic behavior which is closely related to the CDRs investigated in this thesis (Gerisch et al., 2009; King and Robert R. Kay, 2019). What differentiates actin waves observed in phagocytotic behavior and macropinocytosis from their counterpart observable in actively migrating cells is their circular shape, which raises additional questions as to how the proteins involved in formation of such vast actin rings are assembled into a controlled circular shape (Allard and Alex Mogilner, 2013). Additionally, actin waves play a crucial role in polarization of cells by providing a directional assembly-disassembly mechanism within them (Inagaki and Katsuno, 2017). Another observed function of actin waves is active long distance transport of actin and closely associated proteins towards growth cones of axons via a process named axonal actin waves (Ruthel and Banker, 1998).
Due to the large scale of these waves, the typical processes involved in actin regulation do not suffice to fully explain the underlying protein kinetics resulting in such waves, which lead to proposition of underlying reaction-diffusion system like behavior (Bernitt and Döbereiner, 2017; Vicker, 2002; Zeng et al., 2011). This similarity to reaction-diffusion systems will be further described in Chapter 4.

3.2 Circular Dorsal Ruffles

Circular Dorsal Ruffle (CDR) are a specific kind of large circular actin waves protruding several micrometers upwards from the dorsal cell surface, which are closely involved in internalization of extracellular material through the process of macropinocytosis (Hoon, Wong, and C.-G. Koh, 2012; Kerr and Teasdale, 2009; King and Robert R. Kay, 2019). Since macropinocytosis is a process found not only in mammalian cells, but also in, e.g. *dictyostelium discoideum*, it is reasonable to assume it is a very ancient process of endocytosis for cells, the presence in unicellular organisms, as well as multicellular organisms does point to the process existing before these organisms diverged from one another (King and Robert R. Kay, 2019).
Another factor sparking interest in these structures is the fact that some pathogens, like bacteria and viruses, actively exploit the mechanism in order to enter the cells by stimulation CDR formation in order to be internalized, elegantly bypassing the cell membrane (Bloomfield and

Robert R. Kay, 2016). Some examples of such pathogens include bacteria like salmonella, or viruses like for example HIV-1 (Maréchal et al., 2001; Mercer and Helenius, 2009; Rosales-Reyes et al., 2012).
Stimulation of CDRs is typically done by exposing the cell to growth factors, see Section 3.2.1, which triggers a signaling cascade ultimately resulting in formation and closure of the cup like actin structure. An overview of the stimulation process is given in Section 3.2.2. This signaling cascade causes molecules involved the regulation of actin polymerization, as introduced in Section 2.2, to be locally recruited into a circular shape, with an intense patch of Ras and PIP_3 in the center of the forming structure. The dense actin perimeter of a CDR additionally functions as a diffusion barrier, further intensifying the patch by self-amplification (Robert R Kay, Williams, and Paschke, 2018; Welliver et al., 2011; Yoshida et al., 2018).
After this initiation step, actin is increasingly polymerized around the PIP_3 patch, resulting in the CDR pushing the membrane upwards. Finally, myosin is recruited around the rim of the CDR in order to pull the structure together to enclose a vesicle of extracellular material (Swanson, 2008).

3.2.1 Growth Factor Induced Stimulation

The most common form of CDR stimulation in fibroblasts is done by growth factors, which are signaling molecules promoting cell proliferation and migration (Hannink and Donoghue, 1989; Tallquist and Kazlauskas, 2004). Many different growth factors exist, some of which are proven to be involved in stimulation of CDR formation, such as Hepatocyte Growth Factor (HGF), Epidermal Growth Factor (EGF) and Human Platelet Derived Growth Factor (hPDGF) (Antoniades, 1981; Legg et al., 2006; Swanson, 2008). Where hPDGF is the best investigated growth factor in CDR stimulation, hence the focus here will lie on this particular one. The effects of hPDGF are observed to be heavily involved in wound closure, since they stimulate fibroblasts and other cells involved in tissue repair to migrate and proliferate, with blood platelets being the first cells to initiate the repair process at the wound site by secreting hPDGF, hence the name platelet-derived (Pierce et al., 1991; Tallquist and Kazlauskas, 2004).
These growth factors bind to extracellular receptors on the cell membrane, the Receptor Tyrosine Kinase (RTK), which triggers a signaling cascade within the cell, which will be further described in Section 3.2.2. Upon stimulation and CDR formation, the activated RTKs are subsequently internalized from the surface membrane (Orth and M. A. McNiven, 2006). This removal of RTKs from the cell membrane additionally reduces the relative cellular sensitivity to successive stimulation with the same stimulant (Lyashenko et al., 2020). This relative change in sensitivity to external stimuli by endocytosis of receptors is not only observed for growth factors in the context of CDRs and activated RTKs, but also for other receptor-based signaling events implying an importance of such processes in signaling cascades across different biological functions (ibid.).

3.2.2 Stimulation Pathway

Since the overall signaling network underlying CDR formation is highly complex and involves a multitude of positive and negative feedback loops across a series of signaling proteins, a simplified pathway, as proposed by Hoon, Wong, and C.-G. Koh, 2012, is shown in Figure 3.1. This simplified pathway shows the qualitative steps from growth factor stimulation, recruitment of various signaling proteins, over CDR formation and ultimately collapse and redistribution of actin. This simplified graph shows the key proteins involved in the process which have been

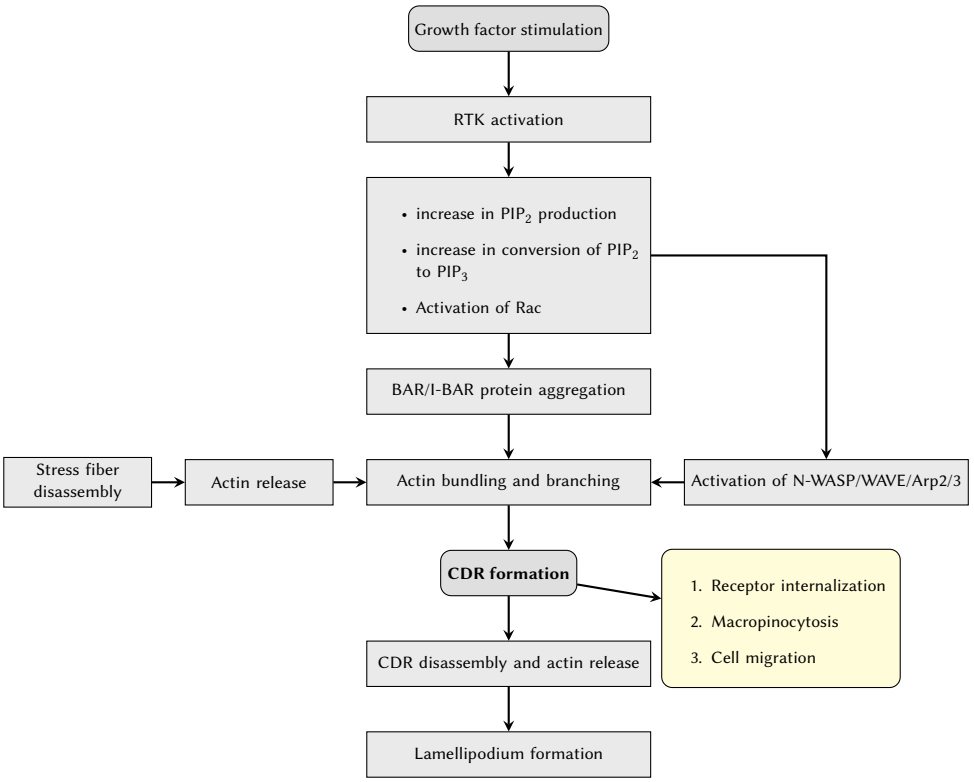

Figure 3.1: Simplified stimulation pathway of CDR formation upon growth factor stimulation. Following the activation of RTKs, an increase in PIP_2 production and higher turnover of PIP_2 to PIP_3 can be observed, along with activation of Rac, N-WASP, WAVE and Arp2/3. Disassembly of present actin stress fibers releases previously bound actin to be available for new actin polymerization. Upon closure and disassembly of the CDR, the re-released actin is then used again to restructure the cytoskeleton. After Figure adapted from Hoon, Wong, and C.-G. Koh, 2012.

introduced in Section 2.2, where the BAR and I-BAR proteins serve as means for membrane deformation.

As is visible from the pathway, an activation of RTKs via growth factors triggers an activation of Rac, an increase in PIP_2 production, as well as increased turnover from PIP_2 to PIP_3. This local increase in PIP_3 production is esepcially prevalent in the central region of the CDR to be formed. Activation of closely actin related proteins, such as N-WASP, WAVE and Arp2/3 in combination with higher local g-actin availability from increased stress fiber disassembly enables

increased formation of new branched actin bundles which will then be locally incorporated into a newly formed CDR. The formed CDR then internalizes activated RTKs and is involved in macropinocytosis or cell migration. After closure of the CDR into a vesicle, the previously recruited actin is released again and used to restructure the cytoskeletal components of the lamellipodium.

Chapter 4

Reaction-Diffusion Systems

The phenomenon of traveling actin waves described in the previous chapter can be theoretically modeled using a variation of different kinds of models. Among these, the usage of reaction-diffusion systems was the first to be proposed, since they are known to be able to express traveling pulses.
The remarkable property of such systems is, that they are able to reproduce phenomena observable in highly complex chemical or biological systems with the model itself being a lot less complex. In the case of actin wave modeling, these reaction-diffusion models abstract away most of the underlying actin signaling machinery, as introduced in Section 2.2.
In the following, the focus will lie on two different reaction-diffusion systems. Section 4.1 begins with a brief introduction of the overall concept of such mathematical models. Section 4.2 introduces the FitzHugh-Nagumo model as one possibility to model CDR behavior. This model was originally formulated in order to model action potentials traveling along the axon of a neuron and is a simplification of the older Hodgkin-Huxley model. Using this model in a two-dimensional form allows for generation of expanding traveling wave pulses.
The second model to be introduced in Section 4.3 is a bistable model specifically formulated for traveling actin waves in CDRs. A specific feature of this model is conservation of the total amount of actin, while transforming it into three different possible sub-species. This model closely mimics the asymmetry of molecular components on the interior and exterior side of a CDR, as described in Section 3.2 and is able to express traveling waves which resemble many experimentally observed behaviors.

4.1 Traveling Waves in Reaction Diffusion Systems

As presented in Section 3.2.2, the underlying protein signaling pathway for the formation of CDRs is highly complex. Nonetheless, it is possible to vastly reduce the complexity in order to formulate model equations approximating actin wave dynamics, a typical approach in physics. Approaches to model such systems thus far have been successful using reaction-diffusion sys-

tems which are well known for their pattern formation potentials (Strogatz and Fox, 1995). Such reaction-diffusion systems combine, as the name suggests, a reaction of some sort, converting one thing into another, with diffusion, causing one or more species to spatially spread out. Chemical reactions can be modeled using reaction-diffusion systems, such as for example the Belousov–Zhabotinsky reaction (Vanag and Epstein, 2004). These models can incorporate many different species reacting with one another.
Modeling of biological phenomena using reaction diffusion systems is a typical approach introduced by Alan Turing (1952). After this fundamental work depicting pattern formation, more research resulted in more complex models, capable of complex patterns.
Various models exhibit traveling waves or wave fronts. In the following, two different models are presented. In Section 4.2, the FitzHugh-Nagumo (FHN) model — an excitable system which exhibits traveling waves — is presented. This model originates from early modeling of action potentials in neurons as a simplification of the Hodgkin-Huxley model.
The other presented model in Section 4.3 is a bistable system which was specifically formulated for CDRs by Bernitt, Döbereiner, et al., 2017. One of it's main features differentiating it from other such models is conservation of total actin in the system. No new actin can be generated or removed, it is only converted between different variants. Additionally, the proposed bistable stimulation characteristic stems from experimental observations of PIP_3 concentrations within or outside a CDR.
A variety of other modeling approaches exist in literature, such as a Rac-Rho antagonism proposed by Zeng et al., 2011, or curved actin polymerization activators inspired by membrane deforming proteins like BAR and I-BAR formulated by Peleg et al., 2011.

4.2 The FitzHugh-Nagumo Model as an Example for Active Media

In the following and as an example of modeling actin waves using reaction-diffusion models as a type of active, excitable medium, the two-dimensional FHN model will be introduced here (Bernitt and Döbereiner, 2017; Bernitt, C. G. Koh, et al., 2015). This model was originally created to describe action potentials in neurons in one dimension and was independently proposed by FitzHugh in 1961 and Nagumo, Arimoto, and Yoshizawa in 1962. FitzHugh originally named the model *Bonhoeffer-Van der Pol oscillator*, but it was later named after the authors of the two papers suggesting the model (FitzHugh, 1961; Nagumo, Arimoto, and Yoshizawa, 1962).
The model itself is described by Equations (4.1) and (4.2):

$$\frac{\partial V}{\partial t} = D\Delta V + V - \frac{V^3}{3} - R + \eta \tag{4.1}$$

$$\frac{\partial R}{\partial t} = \Phi\left(V + a - bR\right) \tag{4.2}$$

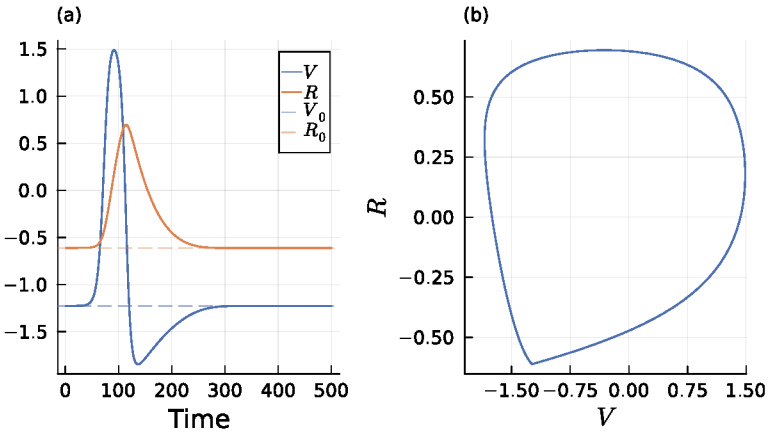

Figure 4.1: Phase cycle of excitation of the FHN model. (a) Values of fields V and R over simulated time. Visible is a steep increase in V, quickly followed by the inhibitor field R. V is then reduced below the initial fixed point value and slowly recovers towards it. The shape an propagation of the V field closely resemble an action potential traveling across an axon. (b) Phase space V vs. R showing the excursion in phase space ending at the fixed point. Parameters used: $D = 0.1, a = 0.8, b = 0.7, \Phi = 0.08$, with fixed point $(V_0, R_0) = (-1.2276, -0.6109)$. Dirichlet boundary conditions were imposed on the simulation domain boundaries.

where V is an activator field and R is an inhibitor field, which in the context of the model's origins were the membrane potential V and a recovery variable R. Further parameters in the model are the constants D, a, b and Φ. Additionally, η represents an external perturbation which can trigger the system.

If the perturbation η is sufficiently large, the system will not return to it's stable fixed point, but will perform an excursion through the (V, R) phase space before returning to it, which closely resembles an action potential traveling along the axon of a neuron, see Figure 4.1. As becomes visible in Figure 4.1 (a), there is a distinct lag between the excitation in the V and R fields, with the recovery field R lagging behind the increase in V. After being dampened by the inhibitor field, the activator field is reduced below the initial starting point and slowly returns to it.

Using the FHN model in it's two-dimensional form, it is possible to obtain propagating circular waves by perturbing the system in it's resting state, using sufficient added noise η. An example of such a traveling wave is shown in Figure 4.2. Here, a circular stimulus in the form of noise is added into the central region of the domain upon initialization of the system. The system is then excited and each perturbed point on the grid is then cycling through the phase space until arriving at the fixed point again. This results in a circular wave traveling outwards from the initial perturbation. Many different observed patterns of CDRs, like periodic waves, wave collision or spiral waves have been reproduced and investigated by using this model with the aforementioned noise-driven excitation (Bernitt, C. G. Koh, et al., 2015). The noise field η can here be interpreted as molecules of a stimulant, like e.g. hPDGF, activating the signaling cascade

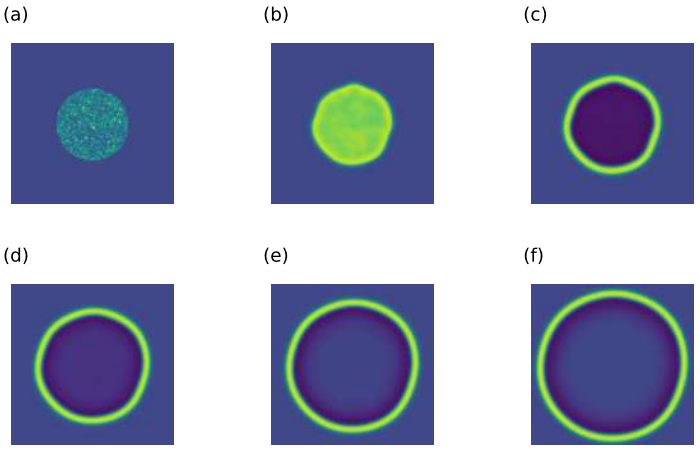

Figure 4.2: Expanding ring as traveling wave from noisy perturbation. Adding a circular, noisy perturbation onto the system at rest in it's fixed point causes formation of a circular wave migrating outwards from the perturbation's location. The space within the previously activated internal region of the ring then returns to the initial fixed point and it is possible to re-introduce a traveling wave by subsequent perturbations.

in a cell (Bernitt, C. G. Koh, et al., 2015).
Despite this generally good performance in modeling CDRs using the FHN model, it does not fully capture the process of expansion from a singular point, followed by contraction and ultimately collapse (Bernitt, Döbereiner, et al., 2017). Therefore, a different model was proposed, specifically designed around experimentally observed changes in dynamics of CDR involved proteins and actin, which will be introduced in the following section.

4.3 Bistability-based Modeling of Actin Waves

Building on the findings using the FHN model, a more advanced reaction diffusion system was developed based on bistability and explicitly formulated for molecular patterns during CDR formation (ibid.). In this model, actin is split into three different species. G being globular, monomeric actin, B being filamentous actin incorporated in a CDR and F being filamentous actin in the cellular cytoskeleton. One main characteristic of this model is that the total amount of actin $A = G + B + F$ is preserved and constant. The individual actin species are then converted into one-another. Assuming the total amount of actin to be constant is only sensible while investigating short time spans, such as the lifetime of a CDR. On longer time spans, the cell will of course generate actin through protein synthesis and remove actin proteins, which would modify the total amount of actin A.
This model mimics the different densities of filamentous actin on the interior and exterior of a CDR, which was described in Section 3.2. In addition, an inhibitor of actin polymerization I is introduced, which combines the experimentally observed activities of Arap1 and PIP_3. By

proposing feedback loops between the suggested actin states, the Equations (4.3) through (4.6) were obtained and describe the model in it's dimensionless form (ibid.):

CDR-incorporated actin

$$\frac{\partial B}{\partial t} = \overbrace{\frac{B^2 G}{1+I}}^{\text{autocat. recruitment and polym.}} - \overbrace{B}^{\text{degradation}} + \overbrace{D_B \nabla^2 B}^{\text{diffusion}} \tag{4.3}$$

Stress fibers and cell cortex

$$\frac{\partial F}{\partial t} = \overbrace{k_{f1}\frac{G}{1+I}}^{\text{polymerization}} - \overbrace{k_{f2}F}^{\text{degradation}} \tag{4.4}$$

Actin monomers

$$\frac{\partial G}{\partial t} = \overbrace{-\frac{B^2 G}{1+I} + B - k_{f1}\frac{G}{1+I} + k_{f2}F}^{conservation} + \overbrace{\nabla^2 G}^{\text{diffusion}} \tag{4.5}$$

Actin inhibitor

$$\frac{\partial I}{\partial t} = \overbrace{k_{i1}B}^{\text{activation}} - \overbrace{k_{i2}I}^{\text{degradation}} + \overbrace{D_I \nabla^2 I}^{\text{diffusion}} \tag{4.6}$$

The inhibitor I is regulated by activation rate k_{i1} coupled to CDR incorporated actin B and auto-degradation rate k_{i2}. In addition, k_{f1} describes the rate of actin polymerization into cytoskeletal actin, with k_{f2} regulating the degradation thereof. The individual components of the model also differ in their diffusion rates, with the cortex actin F being stationary.
The system's fixed points as a function of total actin A read as follows (ibid., supplementary material):

$$B_0^* = 0 \tag{4.7}$$

$$B_{1\pm}^* = \frac{(A-a)}{2} \pm \sqrt{\frac{(A-a)^2}{4} - (1+\alpha)} \tag{4.8}$$

$$F_{0,1\pm}^* = \alpha \frac{A - B_{0,1\pm}^*}{\alpha + (1 + aB_{0,1\pm}^*)} \tag{4.9}$$

$$G_{0,1\pm}^* = A - B_{0,1\pm}^* - F_{0,1\pm}^* \tag{4.10}$$

$$I_{0,1\pm}^* = aB_{0,1\pm}^* \tag{4.11}$$

where $a = \frac{k_{i1}}{k_{i2}}$ and $\alpha = \frac{k_{f1}}{k_{f2}}$ are the ratios of kinetic constants regulating the inhibitor and cortex incorporated f-actin. B_0^* is obviously always stable, while $B_{1\pm}^*$ undergoes bifurcations which yield the model's distinctive features.

The stable point $P_0^* := (B_0^*, F_0^*, G_0^*, I_0^*)$ represents a CDR free state with all actin being incorporated into the cortex or being available as free g-actin monomers (Bernitt, Döbereiner, et al., 2017). The model authors showed that a transition from P_0^* to P_{1+}^* corresponds to CDR formation, with the latter representing the inside of a CDR. Linear stability analysis showed the aforementioned bifurcation to be a finite wavenumber Hopf bifurcation, i.e. the fixed point P_{1+}^* can lose stability to waves.
Some exemplary simulations of the model on domains of different shapes will be shown in the following section in order to visualize the ability to express traveling waves.

4.3.1 Simulated Dynamics of the Bistable Model on Different Domains

Numerical solutions of the model have been calculated on two-dimensional domains with two different shapes in order to visualize the resulting traveling waves. All calculations shown used Dirichlet boundary conditions and were performed using simple two-dimensional lattices and finite differences to approximate the laplacian operator.
Figure 4.3 shows a traveling wave expanding from a localized perturbation in the center of a circular domain. As is visible, the wave initially expands from the center outwards, is then reflected at the domain boundary and contracts back into the location of the initial perturbation. The difference to the previously described FHN model in Section 4.2 is that the bistable model

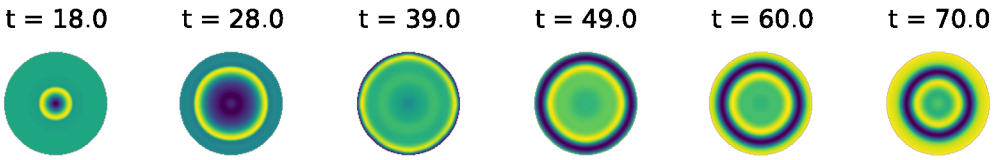

Figure 4.3: Expanding ring on a circular simulation domain for the bistable model for a localized perturbation. The traveling wave expands from the perturbation site, is then reflected at the outer boundary and then contracts back onto it's point of origin. Plotted is the sum of CDR incorporated actin and cortical actin $F + B$ for 6 different timepoints during the simulation. Parameters: $A = 9.67$, $D_b = 0.12$, $D_i = 0$, $k_{i1} = 2.09$, $k_{i2} = 0.53$, $k_{f1} = 2.05$, $k_{f2} = 1.19$

does not return to it's original fixed point and can therefore not be directly re-stimulated (ibid.). Although not directly intended by the model authors, this may be similar to reduced sensitivity to repeated stimuli due to receptor internalization observed in cells, as was described in Section 3.2.1, however this is pure speculation, as receptor activation does not play any role in the model.
Another example using the bistable model is shown in Figure 4.4. Here, the model was simulated on a ring-shaped domain in order to mimic the lamellipodium of a cell spread onto a circular microcontact. Since CDRs can only propagate on the lamellipodium and are reflected by the cell edge and the nucleus, this shape was chosen. The inner white circle here represents the nucleus.

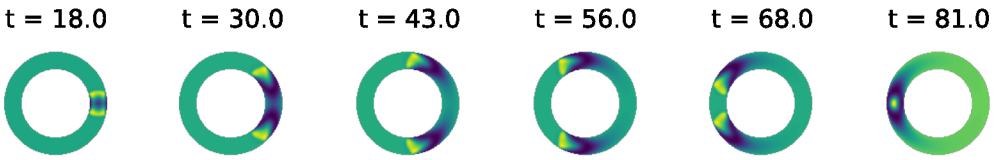

Figure 4.4: Traveling waves on a ring shaped simulation domain for the bistable model for a localized perturbation on one side of the track. This domain shape is supposed to mimic the lamellipodium of a cell on a circular substrate. Here, two individual waves travel from the perturbation site outwards, meeting again at the opposite side of the domain, mutually annihilating each other. Plotted is the sum of CDR incorporated actin and cortical actin $F + B$ for 6 different timepoints during the simulation. Parameters: $A = 9.67$, $D_b = 0.12$, $D_i = 0$, $k_{i1} = 2.09$, $k_{i2} = 0.53$, $k_{f1} = 2.05$, $k_{f2} = 1.19$

Starting from a localized perturbation on the right side of the ring, two waves propagate along the ring until they meet at the opposing side, mutually annihilating each other.
This simulation shows, that such waves do not only expand and retract as shown in the previous figure, but can also travel along a narrow path in a similar fashion as their biological counterparts do.

Chapter 5

Microfluidics

The term microfluidics describes fluid flows in small spatial regimes governed by low Reynolds number physics (Whitesides, 2006). Flows in microfluidic channels, i.e. flow channels with cross sections in the μm^2 regime exhibit certain characteristics which differentiate them from large scale flows. In the regime of low Reynolds numbers the flow is laminar as opposed to turbulent flow.
Microfluidics is not a novel concept, but has distinct advantages over experimenting on cells in petri dishes, such as the ability to controllably replace the medium surrounding the cells without interruption of the imaging process. Usage of microfluidics in life sciences spans from stimulation to so-called lab-on-a-chip concepts (Streets and Huang, 2013), where an entire lab process is put into a microfluidic device or small-scale automated cell culture (Beebe, Mensing, and Walker, 2002), greatly reducing the need for laboratory infrastructure and materials.
Due to the experimental setup relying heavily on microfluidic systems to deliver stimulants to cells during experimentation, this chapter gives a theoretical insight into important concepts of microfluidic perfusion systems in rectangular flow channels which are used in the used experimental setup which will be further described in Section 6.3.

5.1 Microfluidic Flows

The most prominent feature of microfluidics is the predictability of fluidic flows within the flow channel due to the laminarity of the flow. This laminar flow makes fluid transport through a flow channel predictable, since individual layers of fluid are only passively mixed via diffusion, as will be further described in Section 5.3. Knowledge of flow velocities to be expected at cell locations is important for reliable prediction of the experimental setup's effectiveness. For precise stimulation of cells adhering to the walls of a flow channel it is of high importance to be able to determine when the medium surrounding the cells has been replaced with new medium with added stimulant. In order to calculate the minimum time of enabling fluid flow required for the replacement, the combined effects of active fluid replacement via fluid flow and

passive replacement through diffusion must be known. These effects will be investigated in the following sections.

5.1.1 Flow Velocity Profile

The flow velocity profile of pressure driven flow within a flow channel is important, since it gives insight into the variation of conditions within the flow channel. Determination of the flow velocity profile in a given environment is is based on the fundamental Navier-Stokes equation (Bruus, 2008, p. 244):

$$\rho\left(\frac{\partial}{\partial t} + \boldsymbol{v}\cdot\nabla\right)\boldsymbol{v} = -\nabla p + \rho\boldsymbol{g} + \mu\nabla^2\boldsymbol{v} \tag{5.1}$$

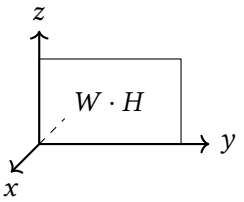

Figure 5.1: The coordinate system used in the following calculations.

Where ρ is the fluid density, p the pressure, $\boldsymbol{g}$ the gravitational acceleration, μ the dynamic viscosity of the fluid and $\boldsymbol{v}$ the flow velocity field. For low flow velocities, as are present in microfluidic systems, the inertia term $\boldsymbol{v}\cdot\nabla\boldsymbol{v}$ can be neglected due to the domination of viscous forces at low Reynolds numbers (ibid., pp. 25-26). The Reynolds number will be further described in Section 5.2. Therefore, Equation (5.1) can be simplified to

$$\rho\frac{\partial\boldsymbol{v}}{\partial t} = -\nabla p + \rho\boldsymbol{g} + \mu\nabla^2\boldsymbol{v}. \tag{5.2}$$

For microfluidic devices with typically simple geometries, this can be further simplified. Assuming constant flow, $\frac{\partial\boldsymbol{v}}{\partial t} = 0$, only parallel to the channel walls in x-direction, $\boldsymbol{v} = v_x(y,z)\cdot\boldsymbol{e}_x$,[1] and a linear pressure drop $p(x) = p_0 - Gx, G = \text{const.}$ along the same direction and neglecting gravitational influences we get

$$G + \mu\nabla^2 v_x(x,y) = 0, \tag{5.3}$$

which describes the flow parallel to the channel walls.
Microfluidic devices typically have rectangular cross sections with $0 \leqslant y \leqslant W$ and $0 \leqslant z \leqslant H$, with W being the channel width and H being the channel height. In order to obtain the flow velocity profile for such rectangular cross sections, Equation (5.3) must be solved for this geometry. Despite the common use of such channel cross sections, no analytical solution to this problem is known in literature. In the following, a quasi-analytical approach to solving the equation as demonstrated by Bruus (ibid.) is reproduced for clarification purposes.
In order to solve (5.3), the first assumption is $W \gg H$ and approximate $W = \infty$. This reduces the problem to flow between plan-parallel plates separated by H in z-direction and allows an

[1] The notation $\boldsymbol{e}_x$ indicates the unit vector along the x-direction.

analytical solution to the problem.
Having infinite extension in y, Equation (5.3) further reduces to a second order derivative in z:

$$G + \mu \frac{\partial^2 v_x}{\partial z^2} = 0 \tag{5.4}$$

This is easily solved by adding the no-slip boundary condition to the problem, $v_x(z = 0) = 0$ and $v_x(z = H) = 0$. This yields the well known solution

$$v_x(z) = \frac{G}{2\mu} z(H - z), \tag{5.5}$$

which is a parabolic velocity profile along the z-direction. Hence, the flow velocity is largest at the channel center. In the scope of cells adhering to the channel bottom, this means the shear stress of fluid flow will be minimal at those locations.
Since $W = \infty$ removes any information about the flow profile at $y = 0$ and $y = W$, a non-analytical approach is needed to further calculate the velocity field in the (y, z) plane.
Solving (5.3) with a sine series of the form (ibid.)

$$v_x(y, z) = \sum_{n=1}^{\infty} \sum_{m=1}^{\infty} a_{nm} \sin\left(\frac{n\pi y}{W}\right) \cdot \sin\left(\frac{m\pi z}{H}\right) \tag{5.6}$$

is an elegant way to avoid extensive numerical calculations. Elimination of series expansion coefficients a_{nm} provides

$$v_x(y, z) = \frac{16G}{\mu\pi^4} \sum_{\text{odd } n,m}^{\infty} \left[nm \left(\frac{n^2}{W^2} + \frac{m^2}{H^2} \right) \right]^{-1} \sin\left(\frac{n\pi y}{W}\right) \cdot \sin\left(\frac{m\pi z}{H}\right) \tag{5.7}$$

Where G is an unknown constant, which can be eliminated by calculating the volumetric flow rate $Q = \iint_A \boldsymbol{v}\, \mathrm{d}\boldsymbol{A}$ and inserting it into (5.7):

$$Q = \frac{64G}{\mu\pi^6} WH \sum_{\text{odd } n,m}^{\infty} \left[n^2 m^2 \left(\frac{n^2}{W^2} \frac{m^2}{H^2} \right) \right]^{-1} \tag{5.8}$$

$$v_x(y, z) = \frac{\pi^2 Q}{4HW} \cdot \frac{\sum_{\text{odd } n,m}^{\infty} \left[nm \left(\frac{n^2}{W^2} + \frac{m^2}{H^2} \right) \right]^{-1} \sin\left(\frac{n\pi y}{W}\right) \cdot \sin\left(\frac{m\pi z}{H}\right)}{\sum_{\text{odd } n,m}^{\infty} \left[n^2 m^2 \left(\frac{n^2}{W^2} \frac{m^2}{H^2} \right) \right]^{-1}} \tag{5.9}$$

Equation (5.9) describes the flow velocity profile in the (y, z) plane scaled with the volumetric flow rate Q, which can be calculated with relatively little computational effort and be verified by experimental data. A numerical approximation of v_x is then achieved by breaking the sums after a sufficient number of steps. The two dimensional flow velocity profile obtained by calculating (5.9) with $H = 3.8\,\mathrm{mm}$, $W = 0.4\,\mathrm{mm}$, $Q = 11\,\mu\mathrm{L/s}$ and the sine series stopped after 100 steps is shown in Figure 5.2. The two dimensional, color-coded velocity field clearly shows a higher

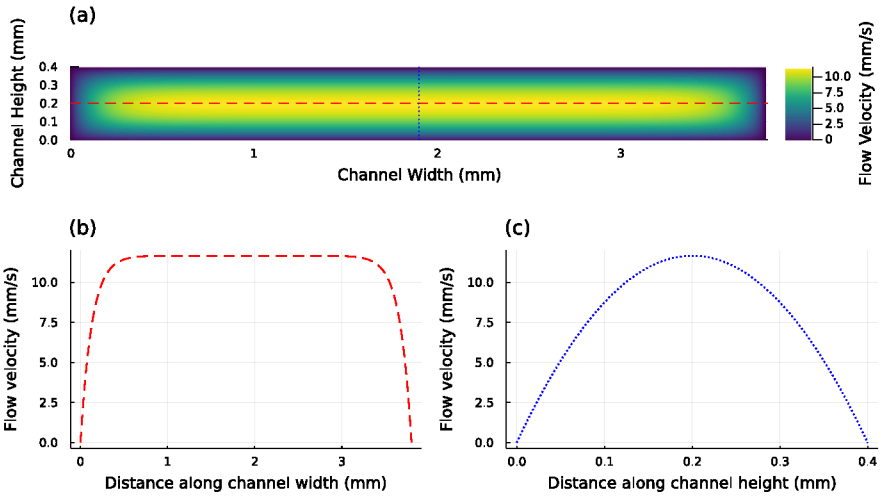

Figure 5.2: Flow velocity profile of a flow channel with rectangular cross section. Shown is the result of Equation (5.9) for $W = 3.8\,\text{mm}$, $H = 0.4\,\text{mm}$, $Q = 0.011\,\text{mL/s}$ — see Section 6.3.3 with the sine series calculated for $N = M = 100$ steps. (a) Two dimensional heatmap of the flow velocity field, (b) Line profile along the channel width as indicated by the red-dashed line, (c) line profile along the channel height as indicated by the blue-dotted line. A significantly higher flow velocity is present closer to the channel center. The profile shown in (c) displays a parabolic flow profile, as was expected from the approximated flow profile between plan-parallel plates in Equation (5.5).

velocity at the channel center than on the edges. Line profiles along the channel width, shown in subplot (b), and the channel height, shown in subplot (c), clearly display the drop in velocity at the channel walls. The line profile in subplot (c) resembles an inverted parabola, as would be expected from the case of plan-parallel plates in Equation (5.5), meaning the approximation $W = \infty$ is sensible at sufficient distances from the channel walls.

5.1.2 Shear Stress at Channel Walls

Shear forced exerted by fluid flow can influence cells. It is therefore required to assess the potential shear forces impacting cells adherent to the channel bottom. Among the undesired effects on cells are unwanted mechanical loads on the cells or an influence on migratory behavior and adhesion (Lu et al., 2004). The shear stress τ_z at the upper and lower channel walls is the derivative of the velocity field v_x with respect to position z multiplied with dynamic viscosity of the fluid μ (ibid.):

$$\tau_z = -\mu \cdot \frac{\mathrm{d}v_x}{\mathrm{d}z} \tag{5.10}$$

With $\tau_z = F_z/A$, the force experienced by a structure of surface area A is then

$$F_z = -\mu A \cdot \frac{\mathrm{d}v_x}{\mathrm{d}z}. \tag{5.11}$$

Recalling the parabolic flow velocity profile, this means shear stress at the channel walls and a few micrometers into the channel will be minimal due to no flow being present at the channel walls. With the nucleus and CDR structures protruding some micrometers from the cell surface into the flow channel, the cells will experience a small force gradient.

Reynolds Number 5.2

The Reynolds number is a measure used to predict flow patterns in different situations. It is defined as the ratio between inertial and viscous forces. The size of the Reynolds number indicates the impact of these two types of forces on the flow situation. Calculation of the Reynolds number is done using

$$\mathrm{Re} = \frac{\text{interial forces}}{\text{viscous forces}} = \frac{\rho \bar{v} L}{\mu}, \tag{5.12}$$

with $\bar{v}$ being the mean flow velocity and L the characteristic length of the flow system, e.g. the channel diameter. For rectangular flow channels which are wetted on all perimeters, the Reynolds number is calculated by (Sharp et al., 2002):

$$\mathrm{Re} = \frac{Q \rho D_H}{A \mu} \tag{5.13}$$

with $D_H = 4 \cdot A/P$ the hydraulic diameter, where A is the cross section and P is the total wetted perimeter. P can be calculated as the overall wetted length along the channel cross section. For a rectangular cross section this is $P = 2W + 2H$. In (5.13), the mean flow velocity $\bar{v}$ has been replaced by the volumetric flow rate Q divided by the channel cross section A. Inserting D_H into (5.13) yields

$$\mathrm{Re} = \frac{2Q\rho}{\mu(W + H)}. \tag{5.14}$$

With the Reynolds number being expressed in this form, it is possible to estimate it's value from experimental measurements, since W, H, μ and ρ are fixed for the experiment and the volumetric flow rate Q being measurable for the experimental setup.
The calculated Reynolds number can then be used to assess, whether the flow system is turbulent or laminar. The range of Reynolds numbers for the onset of turbulent flow in flow channels is rather large in literature, spanning from 1300 to 2400. Avila et al. (2011) determined a critical

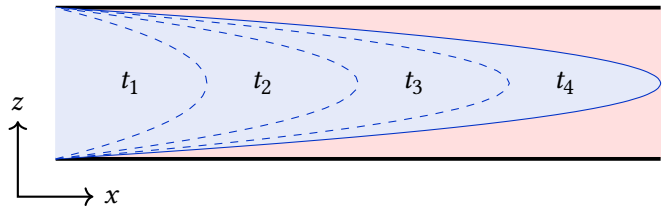

Figure 5.3: Schematic drawing of a new fluid replacing a present fluid in a tube with laminar flow at low Reynolds numbers. Due to parabolic flow velocity profile shown in Section 5.1.1, the new fluid will advance as an elongated parabolic "plug" of replacement fluid along the tube. The timesteps $t_{1..4}$ indicate longer pumping times for higher indices.

transition at around Re = 2300 using numerical calculations, as well as experiments. Hence, for Re $\ll$ 2300 laminarity of flow inside of a microchannel can be assumed.

5.3 Fluid Replacement in Microchannels

With the knowledge gained from the velocity profile calculated in Section 5.1.1, some implications on fluid replacement inside of a microchannel must be assessed. With no flow close to the channel walls, a fluid being flushed in would require infinite time to get sufficiently close to the edges. A schematic drawing of fluid replacement in a tube is shown in Figure 5.3, where for different time steps, a "plug" of new fluid travels along the tube. At the center of the tube, replacement takes place very rapidly, since maximum velocity is to be expected there. However, at the channel walls, the replacement fluid will take very long time to sufficiently replace the fluid previously occupying the channel. This, of course, poses a challenge since the cells being investigated adhere to the bottom of the flow channel. In the following Sections 5.3.1 and 5.3.2, diffusion will be taken into account in order to estimate the approximate volume which is required to sufficiently replace the fluid inside of a flow channel in order to reach the desired treatment concentration at all locations across the channel's diameter.

5.3.1 Combining Diffusion and Flow

For cells adhering to the bottom of a perfusion system channel, this would imply long pumping times before a stimulus could be delivered to the cells. The alleviating effect, which enables sufficiently fast replacement of a fluid inside of a tube is diffusion of molecules from the replacement plug into the fluid present at the channel walls.[2] The underlying principle of particles moving

[2]Or vice versa when a fluid containing a stimulant is to be removed from the flow channel.

from high concentrations to low concentrations is described using Fick's first law (Demtröder, 2008, p. 220):

$$\boldsymbol{J} = -D \cdot \nabla c \tag{5.15}$$

where $\boldsymbol{J}$ is the diffusion flux vector, D is the diffusion constant of the diffusing particle and ∇c the concentration gradient. The minus sign implies a diffusion flux against the concentration gradient. From the schematic in Figure 5.3 follows a very strong concentration gradient between the replacement fluid and the fluid present in the channel. Hence, the diffusion flux will, according to (5.15), be very strong and the fluids will diffuse into each other at the barrier between them. With fluid replacement therefore not only relying on active pumping, but also passive diffusion, the effective replacement timescale will be shorter than anticipated from pure pumping replacement.
In conjunction with the concentration gradient, the diffusion constant D of a particle in a certain medium is the limiting factor for how strong the diffusion flux will be(Einstein, 1905). The diffusion coefficient is defined as

$$D = \frac{k_\mathrm{B} T}{6\pi\eta R_0}, \tag{5.16}$$

where R_0 is the hydrodynamic radius of the diffusing particle, k_B the Boltzmann constant, T the temperature and η the medium's viscosity. The time τ required for a particle do diffuse a mean square distance $< x^2 >$ is then found to be

$$< x^2 > = 2D\tau. \tag{5.17}$$

$$\tau = \frac{< x^2 >}{2D} \tag{5.18}$$

Hence, the time required for a particle to diffuse a distance x will increase quadratically. For low distances however, diffusion is very fast, depending on the diffusion constant. Combining the effects of active fluid replacement via pumping and passive replacement via diffusion solves the problem of replacing the fluid at the edges of a flow channel or tube. For longer pumping times, the fluid profile as outlined in Figure 5.3 causes the layer of remaining old fluid between the replacement and the channel walls to become sufficiently thin for diffusion to be fast and reliable for replacing this remaining fluid.
An estimation of the timescale required for this replacement can be done by calculating the distance $x(z)$ which a particle in a given position z along the cross section of the flow channel will have traveled over time. Reconsidering Equation (5.9) and Figure 5.2, the parabolic flow velocity profile can be assumed to be reasonably correct when not being in the close to the left and right channel walls. The distance traveled by a particle along the length of the flow channel

with respect to it's relative vertical position within the channel can be calculated by simply using the equation of motion without acceleration:

$$x(y,z,t) = v_x(y,z) \cdot t \tag{5.19}$$

Using only the velocity profile at half channel width $y = W/2$, this returns the parabolic flow velocity profile shown in Figure 5.2 (c) and removes the dependency on y. An estimation of the time required to sufficiently replace a fluid inside of the perfusion system used in this work is shown in Section 6.3.4 starting on page 46.

5.3.2 Estimation of Treatment Fluid Volume

For optimal planning of experiments with a perfusion system it is crucial to estimate the amount of liquid required. This is especially important due to potential high costs of treatment drugs. Another important factor is the need to avoid empty fluid reservoirs which would cause air being pumped through the tubing and flow channel, instantly killing cells within. Warrick et al. (ibid.) propose the following equation for this:

$$\Phi = 100\,\% \cdot \left[\frac{C_{c,f} - C_{c,i}}{C_t - C_{c,i}}\right] = 100\,\% \cdot \left[1 - \chi \cdot \left(\frac{V_\mathrm{c}}{V_\mathrm{t}}\right)\right] \tag{5.20}$$

Here, Φ is the relation between treatment fluid C_t, the concentration of the fluid initially present inside of the channel $C_{c,i}$ and the final treatment concentration $C_{c,f}$. V_t and V_c are the treatment fluid volume and the flow channel volume. For $\Phi = 100\,\%$ the concentration inside of the channel is equal to the desired treatment concentration. χ is a scaling factor depending on the flow channel aspect ratio. For this scaling factor Warrick et al. provide numerically calculated values for various aspect ratios, these values are replicated in Table 5.1.

Table 5.1: Numerical values for χ for different channel aspect ratios H/W (Warrick et al., 2007, supplementary material).

H/W	χ
0.0	0.17
0.1	0.21
0.2	0.24
0.3	0.26
0.4	0.27
0.5	0.28
0.6	0.29
0.7	0.30
0.8	0.30
0.9	0.31
1.0	0.31

In order to calculate the volume required to replace the fluid in the channel up to a certain fraction with treatment fluid (5.20) can be rearranged to

$$V_\mathrm{t} = \frac{\chi \cdot V_\mathrm{c}}{1 - \varphi} \tag{5.21}$$

where $\varphi = \Phi/100\,\%$. Hence, calculation of the required volume requires very minimal information on the flow system.

Knowledge of the required treatment volume also enables calculation of the time required to replace the fluid inside of the perfusion system. Combining knowledge of the volumetric flow

rate Q and the treatment volume V_t yields the time t_t needed to reach the desired treatment concentration:

$$t_\mathrm{t} = \frac{V_\mathrm{t}}{Q} = \frac{\chi \cdot V_\mathrm{c}}{1-\varphi} \cdot \frac{1}{Q} \tag{5.22}$$

Evidently, t_t will diverge for $\varphi \to 1$, meaning for highly precise treatment concentrations, increasingly large volumes of treatment fluid are required. It is worth noting that due to added effects of diffusion — Equations (5.20) to (5.22) only take active fluid replacement into account — the calculated value for V_t will be larger than the actually required volume.
This information can be used in a programmable perfusion system like the one used in this thesis to set the active pumping times and ensuring proper treatment of the cells, while keeping the required fluid volumes in the reservoirs at a minimum. By estimating a tradeoff between precision of treatment concentration and treatment volume used, proper treatment of cells can be expected, as well as keeping excess volumes at a minimum, reducing costs per experiment.

Chapter 6

Materials and Methods

This chapter comprises the used materials and employed methodology for acquiring and evaluating of the data acquired during this study. This includes cell culture (Section 6.1), preparation of FN microcontacts for the cells to adhere to (Section 6.2) and the perfusion system used to precisely deliver stimulants to the cells during the experiment (Section 6.3), as well as the used microscopy techniques (Section 6.4.1).
In addition, key concepts involved in imaging and image evaluation are introduced and discussed in Section 6.4. This includes approaches to semi-automated data extraction from microscopy images using the predetermined available locations for cells enforced by microcontact printing. Special focus here lies on an assessment of the perfusion system and time required to sufficiently replace the cell surrounding medium in order to deliver a stimulus of predetermined concentration. Based on the concepts introduced in Chapter 5, the setup is confirmed to be sufficient for precise stimulus delivery to cells.
Technical details of the computational methodology applied to the data are described and, where applicable, their technical implementation more extensively discussed in the appendix Chapter A.
Concluding this chapter is a brief introduction of the statistical methods used in evaluating the obtained CDR data.

Cell Culture 6.1

The cells used in all experiments were murine embryonic fibroblasts of the cell line NIH3T3. Cells were grown under standard conditions of 37 °C and 5 % CO_2 athmosphere to ensure physiological conditions in Dulbecco's Modified Eagles Medium (DMEM) containing 3.7 g/L $NaHCO_3$, 4.5 g/L D-Glucose (*Biochrom, Germany*), 100 µg/mL Penicillin/Streptomycin (*PAA Cell Culture Company, Great Britain*) and 10 % Fetal Bovine Serum (FBS) (*Biochrom, Germany*). Cells were plated at numbers of $3 \cdot 10^4$ and culture was split at 80 % confluency. Cell splitting and

preparation protocols are summarized in the appendix Section B.1 and Section B.2. Cells were mycoplasma free.

6.2 Microcontact Printing

Cells were forced into circular shapes in order to obtain periodic boundary conditions for CDR movement on the cell surface (Bernitt, 2015). This circularity was achieved by employing so-called microcontact printing, following the protocol of Théry and Piel (2009). This microcontact printing is performed by stamping FN shapes onto glass substrate and coating the remaining space with Poly-L-Lysine graft Poly Ethylene Glycol (PLL-g-PEG).
This combination forces cells to spread onto the circular substrate, due to the PLL-g-PEG preventing formation of focal adhesions and the FN being a natural part of fibroblast Extracellular Matrix (ECM), thus promoting formation of adhesion points (ibid.).
This circular shape is fundamentally different from in-vivo fibroblast morphology, however the investigated CDR have been observed in cells randomly spreading to surfaces, as well as in tissues (Hua et al., 2023).
The used microprinting protocol is laid out in the appendix, Section B.3.

6.3 Cell Stimulation using PDGF

A major goal of this thesis was to employ a method viable for precise stimulation of living cells and also providing the ability to easily reproduce the performed experiments. This section outlines the chosen methods and the respective reasoning of choosing each method.
An initial overview of the perfusion system will be given in the following sub sections, followed by a measurement of generated flow rates depending on the applied pressure settings. This initial description is then followed by an assessment of timescale required to deliver the stimulus, followed by considerations concerning the chosen hPDGF concentrations used for experiments.

6.3.1 Microfluidic Perfusion System

Stimulation using varying concentrations of hPDGF, as described in Section 6.3, was performed using a microfluidic perfusion system. This approach was chosen due to the ability of stimulating cells for precise amounts of time and the possibility of removing the added stimulant from the cells. In contrast to classical approaches with cells being imaged in petri dishes, cells were plated onto prepared microcontacts in fluidic chambers by ibidi®in combination with the *Biophysical Tools GmbH p2cs®* air pressure system. The reasoning behind using air pressure generation in contrast to other possible methods is discussed in Section 6.3.5.

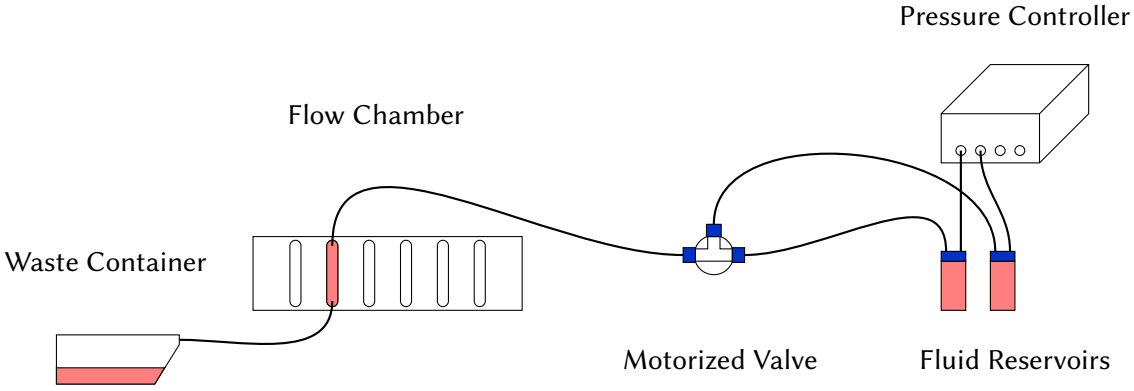

Figure 6.1: Schematic drawing of the used perfusion system. By alternating pressures on the fluid reservoirs and opening the motorized valve depending on desired medium to be delivered to the cells, precise exchange of medium can be achieved. The entire setup is developed so that everything aside from the pressure controller can be placed inside of the microscope's incubator.

Fluid Reservoirs 6.3.2

Fluid reservoirs used in the perfusion system setup were specially crafted for this purpose. On the basis of regular 25 mL Schott Duran®laboratory flasks with screw-lid, through modification of the lid, the reservoirs as shown in Figure 6.2 were built. Modification of the lids was performed by drilling two threaded holes for a 10-32 special tapered thread into the lid. As shown in Figure 6.2 one hole was occupied by a male Luer-Lock[1] to 10-32 special tapered threading adapter for fluid transition. The remaining hole was occupied using a threaded barbed connector which was used for attaching the pressure generation system to the reservoir. Both adapters were then sealed to the modified lid using two-component epoxy glue in order to further suppress air pressure leaks. The female Luer-Lock to barbed adapters as shown in Figure 6.2 (b) were used to thread a Polytetrafluoroethylene (PTFE) tube through the adapter, sealing it off with silicone tubing around the PTFE tube and the barbed end of the adapter.

Thin PTFE tubing was chosen for fluid delivery due to low internal diameter and thus the ability to keep the fluid dead volume required for the tubing as low as possible. Minimizing the fluid dead volume additionally reduces the time required to effectively flush the flow chamber with new medium.

The length of the PTFE tube reaching inside of the fluid reservoir was chosen to reach to the reservoir bottom. By applying a positive pressure to the pressure connector, fluid flow through the PTFE tube towards the flow chambers was created.

[1]The Luer connection system is standardized by ISO 80369 and widely used in scientific, as well as medical applications.

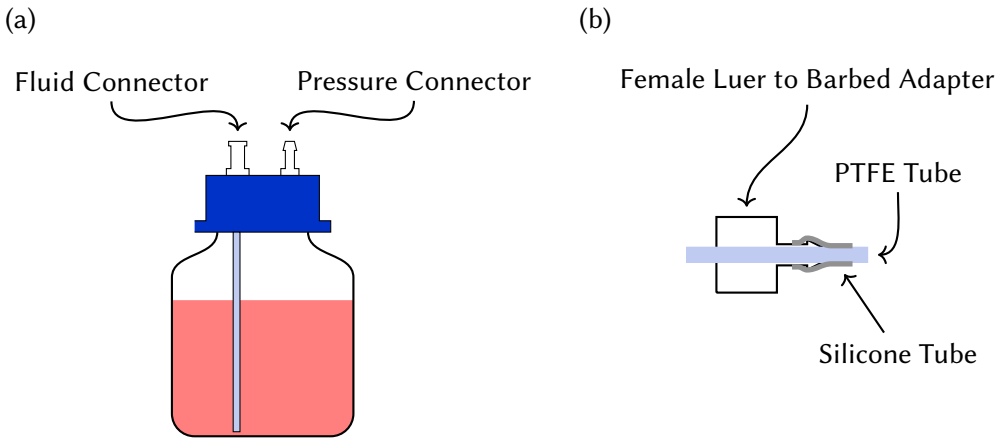

Figure 6.2: Schematic drawing of the used fluid reservoirs (a) and tubing connectors (b). For the connections, standard Luer connectors were used. Additional pressure sealing for the fluid reservoir was achieved by usage of rubber O-rings between the flask and lid (not shown here). A connection from the pressure system to the reservoir pressure connector was done using soft silicone tubing. PTFE tubing was sealed using soft silicone tubes due to PTFE tubing being too rigid.

6.3.3 Flow Chambers

The geometrical properties of flow chambers used during this work are displayed in table 6.1. The flow channels used here with width in the range of several milli meters are comparatively

Table 6.1: Geometrical dimensions of the used ibidi® flow chambers as stated in the user manual.

Length mm	Width mm	Height mm	Volume µL
17	3.8	0.4	25.84

large (Beebe, Mensing, and Walker, 2002)[2], however since one of the primary goals of using microcontact printing and the perfusion system is generation of large amounts of data per experiment, the large surface area enables a large number of cells per channel. Combined with a low magnification objective, see Section 6.4, the number of potentially recorded cells per imaging position is maximized.

An assessment of the perfusion system's Reynolds number reinsures properties like laminar flow are given within the flow channel despite the large dimensions. Recalling Section 5.2, the channel dimensions, fluid density and viscosity, as well as the volumetric flow rate are required. Of these required values, only the volumetric flow rate Q is dependent on pressure added to the system, since the other values are fixed by geometry or physiological conditions. For a given added pressure, Q can easily be measured by weighing the fluid mass Δm transported to the

[2]Typical dimensions of microfluidic flow systems are in the range of 10 µm to 100 µm

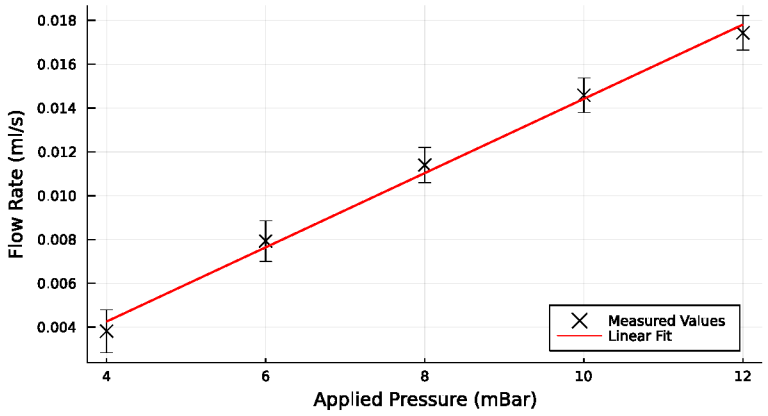

Figure 6.3: Volumetric flow rate Q in mL/s vs applied pressure in mbar for the used perfusion system. The red line indicates a linear fit to the data, showing a linear increase of the flow rate for higher pressures. Each datapoint is averaged over five individual measurements. Applied pressure is assumed to be exact as they were reported from the pressure controller with pressure values fluctuating only at the third decimal.

waste container in a time Δt, see Figure 6.3. The figure shows the measured volumetric flow rate Q of the perfusion system for different applied pressure values. Each measured value is averaged over five individual measurements where fluid mass was pumped through the system for 30 s and then converted to volume using a density for DMEM of $\rho_{\text{DMEM}} = 990\,\text{kg/m}^3$ (Bacabac et al., 2005). The fitted linear function is used to interpolate between the measured pressure values:

$$Q(p) = (1.69 \pm 0.07) \cdot 10^{-3}\,\frac{\text{mL}}{\text{mbar s}} \cdot p - (2.5 \pm 0.6) \cdot 10^{-3}\,\frac{\text{mL}}{\text{s}} \tag{6.1}$$

Using the channel dimensions presented in Table 6.1, the mean flow velocity $\bar{v}$ can also be determined, as this may give a more intuitive understanding of the flow inside of the perfusion system when recalling the parabolic shape of the velocity profile. For a pressure value of 8 mbar as was typically used in the scripted experiments, using Equation (6.1), a volumetric flow rate of $Q(8\,\text{mbar}) = (0.0110 \pm 0.0006)\,\text{mL/s}$ can be determined. Dividing this by the channel cross section yields a mean flow velocity $\bar{v} = Q/A \approx 7.24\,\text{mm/s}$.
With volumetric flow rate Q and a viscosity for DMEM of $\eta_{\text{DMEM}} = 7.8 \cdot 10^{-4}\,\text{Pa s}$ at 37 °C (ibid.), a Reynolds number of $\text{Re} \approx 6$ can be determined. Albeit being larger than 1, this Reynolds number is well within the regime of laminar flows for fluid flows inside flow channels (Avila et al., 2011). With this assessment of the Reynolds number, the assumptions on flow presented in Section 5.1 are justified to be considered true in this experimental setup.

6.3.4 Timescale of Fluid Replacement

With the calculated flow rates, the time for fluid replacement through active flow and diffusion, as presented in Section 5.3 can be estimated. Calculation of the flow velocity profile in Figure 5.2 at page 34 were performed for flow rate Q and channel dimensions W, H of the used flow chambers and can therefore be used to assess fluid replacement during the experiment. Firstly, considering the time required to replace a fluid particle inside of a flow channel only by pressure driven flow excluding the effects of the diffusion is done by multiplying the flow velocity v_x with time t. Considering the shape of the flow velocity profile, calculating this for the center region along the channel width is sensible, since effects at the outer channel walls only influence the velocity at close proximity to them. Therefore, an assessment can be performed by utilizing the velocity profile along half channel width using Equation (5.19):

$$x(t,z) = v_x\left(y = \frac{W}{2}, z\right) \cdot t \tag{6.2}$$

With this and the length of the channel of 17 mm, see Table 6.1, the time for a particle to reach a certain distance into the channel is calculated and presented in Figure 6.4. Here the relative distance into the channel is color coded and it becomes clearly visible, that at the upper and lower edges of the channel the required time becomes asymptotically larger. Directly at the channel edges no movement happens due to the no-slip condition. The dashed line indicates a relative distance into the channel of 1, i.e. a particle traveling through the entire channel.

With the above information it is possible to include diffusion into the process in order to

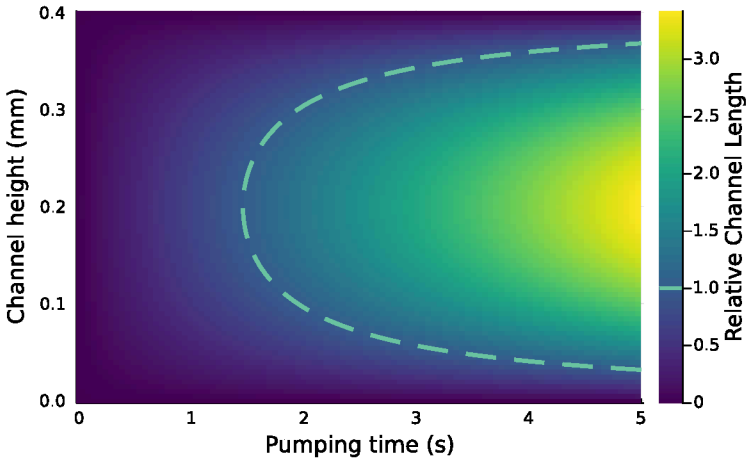

Figure 6.4: Relative distance into the flow channel traveled by particles being moved by pressure driven flow. The dashed line indicates a relative distance of 1, i.e. particles that traveled through the entire flow channel. It is clearly visible, that in the upper and lower regions of the channel, particles move significantly slower. Values for calculations using (6.2) are taken from the perfusion system in use.

determine the time required for replacement fluid particles to reach the channel walls, since

cells are located at those locations. This is also of interest due to potential time differences of stimulant reaching structures protruding upwards from the cell substrate like the nucleus or CDRs in contrast to the lamellipodium, which is however not investigated in this study. Due to the remaining distance to be traveled being very small after seconds of pressure driven flow, e.g. in the order of magnitude of 10 µm, diffusion becomes very fast.
In order to estimate the time particles need to diffuse inside of the microchannel, their diffusion constant needs to be known. In this work the molecule of interest is hPDGF, which is a protein of mass $m_{\mathrm{PDGF}} = 38\,\mathrm{kDa}$ (Antoniades, 1981). An equation to estimate the diffusion constant of molecules from their mass is given by Young, Carroad, and Bell (1980):

$$D \approx 8.34 \cdot 10^{-8} \frac{T}{\mu \cdot M^{1/3}} \tag{6.3}$$

where T is the absolute temperature, μ the dynamic viscosity and M the molecular mass in Da without the unit. At physiological temperature of 37 °C and inside of DMEM, the diffusion coefficient for hPDGF is estimated as

$$D_{\mathrm{PDGF}} = 1.014 \cdot 10^{-10} \frac{\mathrm{m}^2}{\mathrm{s}}.$$

This value seems plausible when comparing to values for smaller or larger molecular masses given by the authors of (6.3). The time required for a particle of diffusion constant D is, solving

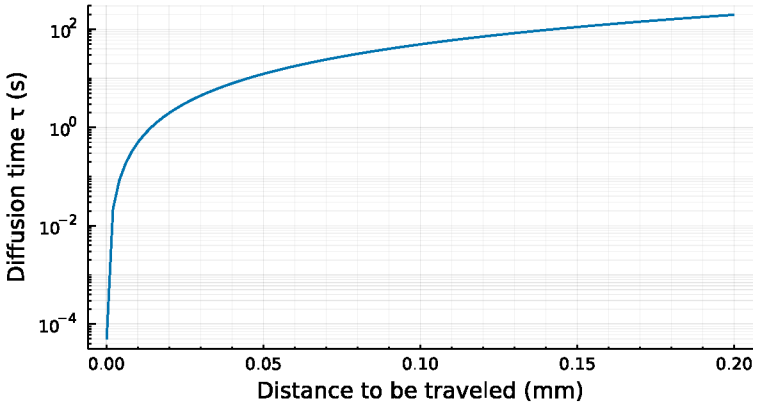

Figure 6.5: Time τ required by hPDGF to diffuse a given distance at 37 °C in DMEM. Time axis shown in logarithmic scaling for better visualizing of orders of magnitude needed to diffuse a certain distance. Maximum distance to be traveled is chosen as half channel height. In combination with Figure 6.4 it becomes clear that typical diffusion times from the therein indicated dashed line appear to be in the order of magnitude of pumping times.

Equation (5.17) — page 37 — for τ, defined as

$$\tau = \frac{< x^2 >}{2D}. \tag{6.4}$$

The time τ required for hPDGF to diffuse varying distances at 37 °C is displayed in Figure 6.5. Here, it becomes visible that the diffusion time at low distances is very efficient at transporting particles into low concentration areas. A distance in the order of 50 µm is traversed in $\tau = 12$ s by diffusion. This information, together with the findings of Figure 6.4 makes it clear that after tens of seconds, the fluid inside of the flow channel will be sufficiently replaced with stimulation fluid.

6.3.5 Flow Generation

Generation of pressure driven flow can be achieved via various methods, such as syringe pumps, peristaltic pumps or air pressure control. In the following, syringe pumps and air pressure control will be further investigated, as both allow for very compact setups.
In order to decide whether which method is beneficial to the experimental setup, it is important to define certain wanted characteristics of the flow system itself and the generated fluid flow. For the experiments conducted here, spanning over multiple hours with repeated exchange of treatment fluid inside of the perfusion system, a setup with sufficiently large fluid reservoirs was required. In order to keep shear effects on the cells at a minimum, it is also crucial to perform any fluid replacement with very low flow velocities. On the basis of these assumptions, the two aforementioned flow generation methods were investigated.

Syringe Pumps Syringe pumps are widely used in microfluidic setups, however the requirements for the experiments render these insufficient. The combination of large fluid reservoirs and low flow rates is the main weakness of these pumps. Flow is generated by pushing a syringe's plunger mechanically, which causes the flow rate to be highly dependent on syringe volume. According to the manufacturer *Harvard Apparatus Inc.* flow rates in the order of nL/h to mL/min are achievable with syringe pumps. However for the lowest flow rates, syringe volumes of 0.5 µL and for larger flow rates volumes of 60 mL to 140 mL are required. This considerably reduces the amount of fluid available for low flow rate experiments, shortening the experiments. Hence, syringe pumps were deemed inappropriate for the experiments planned for the thesis. However, for experiments on single cells in very small flow channels, syringe pumps would be ideal with another positive feature of such pumps being easy determination of volumetric flow rates, since the amount of fluid dispensed by the system is directly correlated to the moved distance of the syringe plunger.

Air Pressue Control The above mentioned limitations of syringe pumps do not apply to air pressure control, however this method is affected by other limitations. Since flow systems using air pressure to control the flow of fluids from a reservoir are not completely isolated from

outside influences, hydrostatic pressure does have an effect on the generated flow, as will be further discussed in Section 6.3.6.
A complete stop of fluid flow is, in comparison to syringe pumps, more difficult to achieve. For syringe pumps simply stopping the pressure on the plunger will stop the flow, however for air pressure systems, removing the added pressure will not stop the flow when a height difference between the fluid level inside of the fluid reservoir and the waste container is present. One method to overcome this would be monitoring of the volumetric flow rate by measuring it and applying negative pressure onto the fluid reservoir — provided the pressure controller is capable of this. A more simply solution is shutting of the fluid flow using a valve as will be described in Section 6.3.6.
Generation of continuous flow using an air pressure controller is easily possible by applying constant positive pressure on the reservoirs. In addition to this, the ability to incorporate arbitrarily large fluid reservoirs in the perfusion system enables very long experiments. However, very large fluid reservoirs also imply very large dead volumes of excess air which will delay the perfusion system's response on controlled pressure changes.
Despite the drawback of the added effects of hydrostatic pressure, an air pressure control system of type *p2cs®* by *Biophysical Tools GmbH* was chosen for the conducted experiments.

Valve Control 6.3.6

As mentioned in the previous section, a drawback of the air pressure driven perfusion system is the influence of hydrostatic pressure on the quasi-open system. Due to these non-negligible effects of hydrostatic pressure in the perfusion system, a valve is required to effectively mitigate any unwanted fluid flow.
The used pressure generator operates in the range of 0 mbar to 20 mbar pressure added onto the fluid reservoirs. In case the fluid levels inside of the reservoirs differ, the passive hydrostatic pressure will have an effect in the magnitude of the added pressure, as shown below assuming 1 cm fluid level difference and the density $\rho_{\mathrm{DMEM}} = (0.99 \pm 0.05)\,\mathrm{kg/m^3}$ of DMEM at $T = (37.0 \pm 0.5)\,^{\circ}\mathrm{C}$.[3]

$$\begin{aligned} p_{\mathrm{hydrostatic}} = \rho g \Delta h &= (0.99 \pm 0.05)\,\frac{\mathrm{kg}}{\mathrm{m^3}} \cdot 9.81\,\frac{\mathrm{m}}{\mathrm{s^2}} \cdot 1\,\mathrm{cm} \\ p &= (0.98 \pm 0.03)\,\mathrm{mbar} \end{aligned} \tag{6.5}$$

Without means to physically suppress flow, this pressure causes unwanted fluid flow within the perfusion system, hence the system includes a motor driven valve to prevent unwanted flows, while being able to enable flow when needed.
Among different approaches, using a manual three way valve of type *Dicofix®3-way Stopcock* —

[3] Temperature chosen due to the incubation system being set to physiological conditions and the fluid reservoirs being preheated to this temperature. Margin of error given in order to account for temperature fluctuations inside of the incubation system. Density value has been determined by weighing a volume of 10 mL of DMEM.

Braun Melsungen AG, steered a servo motor *RS-D10Y — Modelcraft GmbH* was used. In contrast to clamping the tubing, this method does not induce any unwanted short flow spikes in advance to stopping the flow, but results in clear transitions between flow and no-flow settings due to the channel opening being rotated to opened or closed position. Another advantage of using these three-way valves is the wide supply of sterile units[4], without the need to sterilize each unit in the lab with processes which may impair the valve due to high temperatures in the autoclave.

6.3.7 Determination of Used hPDGF Concentrations

The used hPDGF concentrations in the experiments performed during this study were chosen based on findings by Bernitt, 2015, as well as data provided by the manufacturer *Cell Signaling Technology*. The chosen values were 10 ng/mL, 21 ng/mL and 30 ng/mL, where 21 ng/mL instead of 20 ng/mL was chosen due to easier preparation of the used concentration. Expressed in molarities, these values are 0.4 nM, 0.8 nM and 1.2 nM.
The manufacturer provides a figure of stimulant efficiency measured by NIH3T3 cell proliferation, displaying a sigmoidal shape depending on concentration. The aforementioned values were chosen due to these values being located close to the maximum slope of the provided data.
Higher and lower concentrations were investigated, but did not yield sufficient visible results. Lower concentrations appeared to have no visible effect on CDR expression, while higher concentrations appeared to stimulate cells too strongly, i.e. cells forming CDR like structures spanning their entire lamellipodium or heavily changing their morphology upon stimulant delivery.
The results presented in this study may, however warrant further experiments on a wider range of concentrations.

6.4 Imaging and Image Processing

In the following, the process of acquiring microscopic images of live-cells is described along with the steps taken for feature extraction from digital images. As computer vision is a complex field and a complete introduction to it is beyond the scope of this work, most methods used in this section are not extensively explained here. Methods applied to specific data evaluation problems encountered during this thesis are explained in more detail than general image processing methods.

6.4.1 Microscopy

Imaging was performed using a *Zeiss Microimaging Axio Observer Z1* with an attached incubator for control of constant physiological conditions of 37 °C and 5 % added CO_2.

[4]The experimental setup incorporates three-way valves which are also used in medical applications like infusions. Due to this, sterile units of high quality are readily available.

In order to maximize the number of cells per Field of View (FOV), an objective with low magnification of 10x — *Zeiss Achroplan 10x/0.25 Ph1* — was used. This magnification in combination with Phase Contrast (PC) imaging yielded an optimal trade off between captured fine details and the number of cells. Additionally, with CDRs protruding several micrometers upwards from the lamellipodium, higher magnifications impede CDR identification due to too shallow depth of field and CDR outlines only being visible as faint lines in the image.
Contrast enhancement via PC was chosen due to the low difference in optical density between cells and their surrounding medium rendering bright-field microscopy unusable. Another contrast enhancement method for cell microscopy is Differential Interference Contrast (DIC), however this method heavily relies on unaltered polarization angles of light beams (Allen, David, and Nomarski, 1969). Since the flow chambers used in the experimental setup are made from plastics[5] this requirement is not met and image contrast generated using DIC in this setup is sub optimal.
Image timeseries were taken using the attached *Zeiss AxioCam* cameras and *Zeiss AxioVision* software. *AxioVision* was used to navigate a list of locations in the specimen for each recorded timepoint per FOV in order to maximize the amount of collected data per experiment.

Cell Array Registration 6.4.2

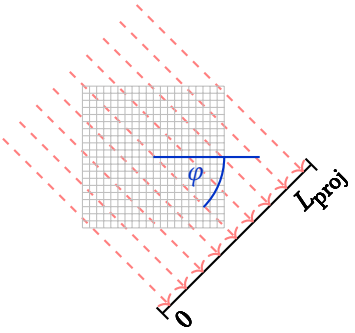

Figure 6.6: Sketch of the Radon transform principle in image processing. The projection onto the black line at angle φ is achieved by summing up all image pixels (gray grid) along the indicated red-dashed lines. This process is repeated for every projection angle $\varphi \in [0, \pi]$.

Due to using microcontact printing, see Section 6.2, the cells were not randomly distributed within the flow channel, but adhered to an underlying pattern determined by the used stamp. This underlying pattern is known from the mould used in the casting process of the stamp and can therefore be utilized to identify locations within the full image where cells can adhere. Finding such locations was performed by fitting an ideal microcontact-grid onto the image. The steps involved in the fitting process are hereinafter presented.

Since aligning the Polydimethylsiloxane (PDMS) stamp perfectly with the flow channel is virtually impossible due to the process being manual, the printed FN substrates will be tilted by an angle α_{tilt}. Determination of α_{tilt} is therefore the initial step to fit the ideal cell locations to the ones present in the recorded dataset. Finding this angle is performed using the Radon transform (Radon, 1986) which is widely used in medical applications such as, e.g. computed tomography (Ter-Pogossian, 1977).

[5]The exact type of plastics is unknown due to the manufacturer not disclosing the material.

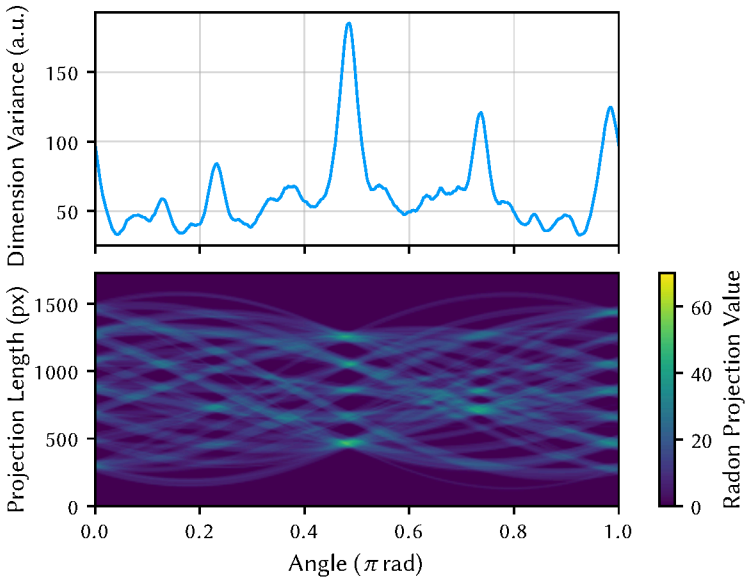

Figure 6.7: Illustration of tilt angle α_{tilt} determination using the Radon transform. The lower figure shows the so-called sinogram obtained by applying the Radon transform to a version of the source image which was modified using edge detection algorithms. The visible pattern has peaks at projection angles where the cell patches align perfectly. Calculating the variance of the sinogram's brightness values along the projection length, as indicated in the upper plot, is used to identify the ideal turning angle α_{tilt}, which is located at the maximum variance.

The working principle of the Radon transform in the scope of image processing is sketched in Figure 6.6. For every full pixel step along the projection length from $L = 0$ to $L = L_{\text{proj}}$, the image pixels along perpendicular lines (indicated by red-dashed lines in Figure 6.6) are summed up. This process yields a so-called sinogram, an example is displayed in Figure 6.7. This is repeated for angles $\varphi \in [0, \pi]$. In the medical example of computer tomography the process principle is similar. By rotating the x-Ray source around the patient along with the opposing detector array, an x-Ray projection for each angle is recorded and then computed into the tomography image by applying the inverse Radon transform on the data.
The actual determination of the angle α_{tilt} is displayed in Figure 6.7, the lower part of the figure displays the so-called sinogram obtained by applying the Radon transform on the image for angles $\varphi \in [0, \pi]$. Only a half rotation is required due to symmetry. Performing the Radon transform with a full rotation only yields duplicate data along the second half of the rotation. The stripes in the obtained pattern converge onto each other at projection angles where the cells are perfectly aligned. Finding α_{tilt} is then performed by calculating the variance of the sinogram along the projection length, see upper part of Figure 6.7, and identifying the angle with maximum variance. Multiple local maxima split by $\Delta\varphi = \pi/4$ can be identified due to the locations on the cell grid overlapping for $\Delta\varphi_i = i \cdot \pi/4,\ i \in \{0, 1, 2, ...\}$. The absolute maximum is located where

the number of aligned cell locations is maximal.[6] With the tilt angle α_{tilt} determined, the ideal

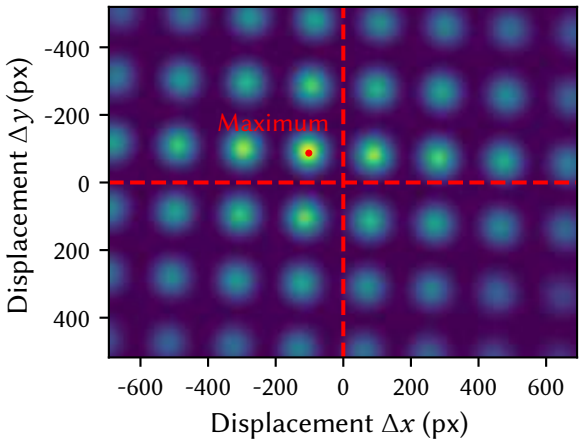

Figure 6.8: Example for fitting the ideal grid to the recorded cell grid using the two dimensional convolution method. The color coded image $c(\Delta x, \Delta y)$ displays periodic maxima where the two input images overlap maximally. The maximum value denoted by the annotated red dot displays the minimum shift $(\Delta x, \Delta y)$ required for the fit. No color bar is shown because pixel values apart from the absolute maximum are insignificant.

grid is calculated and then rotated by α_{tilt}. With known geometrical properties and pixel scaling factors, a binary image with value 1 denoting the positions of potential adhesion spots and 0 denoting the background is generated. Using two dimensional convolution maps of the ideal grid and the imaging data, the offset $(\Delta x, \Delta y)$ required to align the ideal grid with the recorded cell layout is measured, see Figure 6.8. Convolution is a method widely employed in image processing for object detection and pattern matching (Bovik, Alan C., 2009). Calculation of the two dimensional image convolution in it's continuous form is performed using the following equation

$$c(\Delta x, \Delta y) = \int_0^X \int_0^Y I(x + \Delta x, y + \Delta y) \cdot G(x, y)\, \mathrm{d}y\mathrm{d}x, \tag{6.6}$$

where $I(x, y)$ is the input image and $G(x, y)$ is the pre generated ideal grid. Due to image data being discrete with a fixed number of pixels M in x-direction and N in y-direction, Equation (6.6) can be rewritten into it's discrete variant:

$$c(\Delta x, \Delta y) = \sum_{m=1}^{M} \sum_{n=1}^{N} I(m + \Delta x, n + \Delta y) \cdot G(m, n) \tag{6.7}$$

[6] Due to the imaging data being rectangular with a higher number of cells along one axis, a preferential orientation exists. On square images with a square grid of cells, multiple rotation angles would be viable.

This process corresponds to a two-dimensional convolution $I(x, y) * G(x, y)$. A property of the convolution operation is it being a multiplication in Fourier space (Bronstein et al., 2008, p. 794). Calculating the convolution in Fourier space is performed by applying the Fourier transform $\mathcal{F}\{\cdot\}$ on Equation (6.6) and performing the inverse Fourier transform on the result:

$$\mathcal{F}\{c(\Delta x, \Delta y)\} = \mathcal{F}\{I\} \cdot \mathcal{F}\{G\}^* \tag{6.8}$$

$$c(\Delta x, \Delta y) = \mathcal{F}^{-1}\left\{\mathcal{F}\{I\} \cdot \mathcal{F}\{G\}^*\right\} \tag{6.9}$$

where $\mathcal{F}\{G\}^*$ is the complex conjugate of $\mathcal{F}\{G\}$ and $\mathcal{F}^{-1}\{\cdot\}$ the inverse Fourier transform. Performing the cross correlation in Fourier space greatly reduces computation time by using efficient Fast Fourier Transform (FFT) (Ukidave et al., 2013). Identification of the shifting offset required to align both images onto one another is then performed by locating the maximum of $|c(\Delta x, \Delta y)|$, as indicated in Figure 6.8. The ideal grid is then overlaid onto the imaging data and used to automatically crop cell Regions of Interest (ROIs) — for further details on the implementation of the process see Sections A.1.1 and A.1.2 in the appendix.

6.4.3 Circular Kymographs

In digital imaging analysis, a kymograph is typically a two dimensional image consisting of image brightness values gathered along a selected line for every frame in an image sequence or video, meaning the resulting image has a time axis correlating to video frames and a length axis which denotes distance along the selected line. This method is widely used in life sciences from medical applications to cell biology and analysis of subcellular structures.
In this case with cells spread onto circular FN substrates and the resulting disk like morphology, a non-linear approach, the circular kymograph, was introduced into the work group by Bernitt (2015). This circular kymograph uses the forced circular morphology of the cell and generates a kymograph along a selected circle between cell edge and nucleus, indicated by the dashed red line in Figure 6.9. The dark spot overlaid by this line below the nucleus is a CDR, meaning that any CDRs will be recorded into kymographs as dark traces. Since this space on the lamellipodium is the only viable location for CDRs to emerge, any occurring CDR and it's movement will be tracked in the generated kymograph.

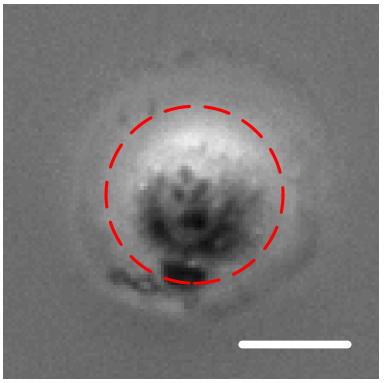

Figure 6.9: Example of a circle used to obtain a circular kymograph. The dashed red line indicates the locations being recorded into the resulting kymograph. The dark structure below the nucleus is a currently expressed CDR, hence CDRs will be recorded as black traces in the kymograph. Scale bar: 20 µm

This method therefore enables measurement of CDR frequency, lifetimes and distance traveled, since the cellular layout enforces a quasi one-dimensional path for CDRs to propagate.
Further information on technical details of how the circular kymographs are obtained from digital images is presented in the appendix, Section A.1.3.

Cell Segmentation 6.4.4

Segmentation of microscopic images for feature extraction such as total area of the cell, area of the nucleus, roundness of the cell and width of the lamellipodium was performed using means of Convolutional Neural Networks (CNNs) (Aggarwal, 2018, Chapter 8). Such CNNs are inspired by the interaction of neurons in the brain and can be statistically "trained" to identify certain characteristics, depending on the layout of the used model. A more detailed description of how these models work mathematically is beyond the scope of this thesis.
Here, the U-Net model as proposed by Ronneberger, Fischer, and Brox (2015) was used for this purpose due to very good results with small training datasets and good performance on microscopy images of cells. Such deep learning methods require labeled training data to "learn" identification of image properties (Aggarwal, 2018).[7] In this case, the goal was to discriminate between background, cell and nucleus. Hence, each training image needed three labels.
Training data required to achieve good performance of the CNN was obtained by methods of active contours (Xu and Prince, 1998a). Active contours, also called "snakes" as introduced by Xu and Prince (1998b), use image characteristics to generate a potential energy field. An initial contour is then iteratively optimized using Gradient Vector Flow (GVF) (Xu and Prince, 1998a,b).

[7] In fact, all machine learning and deep learning methods require data to be trained on, so they can adjust parameters for optimal fitting of the data. In the concept of neural networks this process is often called training and the model iteratively "learns" how to achieve high accuracy by adjusting fitting parameters of the model.

This optimization minimizes an energy function, ideally placing each point of the contour closest to the targeted characteristic. The authors propose the GVF-field $\vec{v} = [u(x,y), v(x,y)]$ which minimizes the energy functional

$$E = \int \left(\mu \left(u_x^2 + u_y^2 + v_x^2 + v_y^2 \right) + \nabla f^2 \left(\vec{v} - \nabla f \right)^2 \right) \tag{6.10}$$

where $f(x,y) = -\nabla I(x,y)^2$ is an edge detection of the original image I and μ is a parameter. For iterative minimization of the energy functional, u and v are treated as functions of time and solving the following functions:

$$u_t(x,y,t) = \mu \nabla^2 u(x,y,t) - [u(x,y,t) - f_x(x,y)] \cdot \left[f_x(x,y)^2 + f_y(x,y)^2 \right] \tag{6.11a}$$

$$v_t(x,y,t) = \mu \nabla^2 v(x,y,t) - \left[v(x,y,t) - f_y(x,y) \right] \cdot \left[f_x(x,y)^2 + f_y(x,y)^2 \right] \tag{6.11b}$$

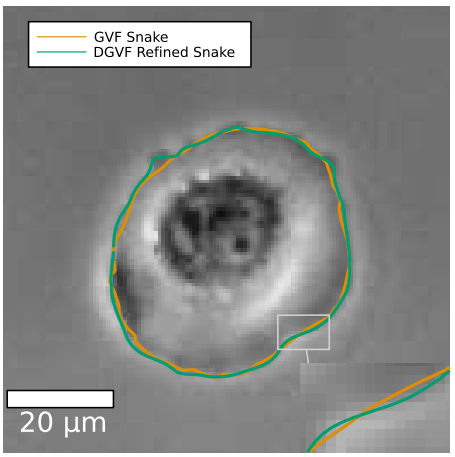

Figure 6.10: Example of Directional Gradient Vector Flow (DGVF) active contour refinement on a PC image. The orange line indicates the contour obtained using regular GVF after manually placing an ellipse around the cell outlines. The green line indicates the contour after refinement using DGVF. The refined contour follows the visible cell outlines more accurately.

In this work due to the use of PC, a method adapted to the unique artifacts and image properties of the generated images was used, the so-called DGVF introduced by Seroussi et al. (2012). This method utilizes the typical PC artifacts like halation to find cell edges. This method uses a two-step approach consisting of an initial approximation of the cell contour by using the original GVF approach as described above, which returns a contour which is already close to the cell outlines. With this preliminary result, a directional edge map is calculated and then used to drive the contour closer to the cell outline (ibid.). This directional edge map is obtained by defining a signed distance map $\phi(x,y)$, which measures the distance of each point from

the contour. $\phi(x, y)$ is positive outside of the contour and negative inside of the contour. The directional edge map is then obtained from

$$f_2(x, y) = \begin{cases} -(\nabla\phi \cdot \nabla I)^2 & \text{for } \nabla\phi \cdot \nabla I > 0 \\ 0 & \text{for } \nabla\phi \cdot \nabla I \leq 0 \end{cases} \tag{6.12}$$

An example of the refinement achieved by this method is shown in Figure 6.10. A clear improvement in the reproduction of the cell edge is visible, the classical GVF did not properly converge to the actual cell boundaries, whereas the refined DGVF contour is more accurate.
The same method can be used to segment the nucleus. By placing the ellipse for the initial contour inside of the lamellipodium, close to the nucleus, the snake will converge to the outlines of the nucleus. By inspecting each generated contour, a good training dataset is ensured. The U-Net model was trained using a dataset of 100 microscopy images of varying focus accuracy and cell morphology[8] with each image being labeled for background, cell outline and nucleus outline. In addition to the variation in the data itself, the data for training was augmented by rotation of the image itself in order to minimize the effects of overfitting the model.

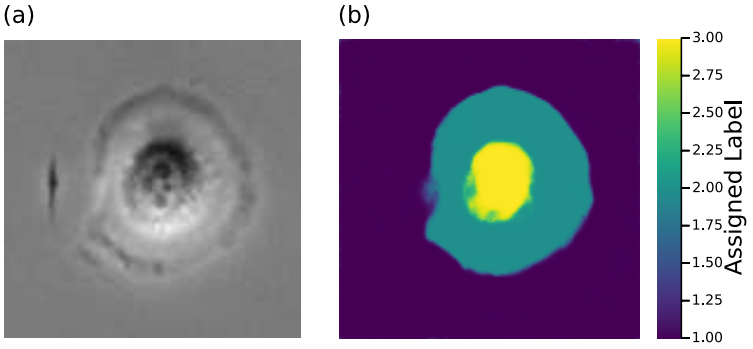

Figure 6.11: Example of cell image segmentation using U-Net. (a) Image of a cell not perfectly adhering to a circular microcontact. The area on the lefthand-side would be especially challenging for typical segmentation approaches, due to very low contrast at the cell boundary. (b) Color coded labels assigned to image regions by the U-Net implementation. Pixels labeled as 1 are identified as background, 2 is the cell lamellipodium and 3 the cell nucleus. The segmentation is overal very precise with very clear boundaries between background, cell and nucleus, respectively. In addition, the debris next to the cell was properly identified as not being a part of the cell by the neural network.

After training, the U-Net yielded very good results as shown in Figure 6.11. Comparing the input image (a) to the label output (b) shows very good accuracy of the assigned labels. Despite

[8] Despite each cell being placed on a circular substrate, see Sections 6.2 and B.3, individual cells often do not perfectly assume a circular shape due to variations in cell size or imperfect adhesion. Additionally, in some experiments due to thermal drifting in the microscope, the focus accuracy deteriorated over the time span of the experiment.

areas of low contrast, e.g. the area of detached lamellipodium on the left-hand side of the cell, the U-Net accurately identified the cell boundaries. Additionally, the debris present in the image was properly labeled as background. Such debris imposes difficulties for various classical image segmentation methods which often require additional processing of the segmented image after initial processing. Such processing might involve removing smaller objects, opening and closing contours and a large variation of other issues, which heavily depend on the quality of the input images. The overall downside of this method is the requirement of considerable computational power of the training of the network, as well as the inference process[9].
Given sufficiently powerful computer hardware, this method makes it applicable to automatically segment the full stack of all images which are used to generate data. Hence, it is possible to obtain time series of cell area, nucleus area and other geometrical metrics. Rising availability of specialized hardware for neural network applications will increase the feasibility of such approaches in the future.

6.5 Layout of Stimulation Experiments

The experimental setup used consists of a microfluidic perfusion system, further described in Section 6.3.1. This perfusion system is used to facilitate precise stimulation of cells with hPDGF added to the cell culture medium DMEM. With the experimental setup being programmable, each experiment was repeatable with stimulations happening at precise points of time.
The experiments performed in this work generally consisted of five different timespans, which are hereafter denoted as experiment blocks. The five experiment blocks are defined as follows

1. Only DMEM present in the flowchannel. This is the initial state of the cells after experiment preparation and setup.
   Duration: 15 min

2. The first stimulation phase. Replacement of medium with DMEM containing added hPDGF. The hPDGF concentration is varied across individual experiments.
   Duration: 15 min

3. Removal of stimulation medium and renewal of DMEM. This is referred to as the recovery phase of the experiment. The duration of this phase is varied for different experiments, thus providing cells with different recovery[10] timespans after the initial stimulus.
   Duration: 10 min to 45 min in 5 min steps

4. The second stimulation phase. After the recovery period, the cells are exposed to a second stimulus. This stimulus again is performed by replacing the present medium with DMEM

[9] Processing all recorded frames for every cell during this thesis took several weeks of processing on the Central Processing Unit (CPU). This time would have been greatly reduced by employing a high performance Graphics Processing Unit (GPU), however this was not available.
[10] Also referred to as “delay” or “delay time”.

with added hPDGF.
Duration: 15 min

5. For the final phase of the experiment, the stimulus medium is again replaced with standard DMEM.
Duration: 15 min

Of these five blocks, only the third one varies in length. Replacement of medium using the perfusion system is performed using identical settings for added pressure and flow times, meaning the used valve is open for equal amounts of time. This exact repeatable setup allows for better comparability between individual experiments which are then collected into a complete dataset for evaluation.

Statistical Analysis 6.6

Due to the amount of generated data and the multitude of measured cell properties, statistical methods were used to reduce the dimensionality of the dataset through Principal Component Analysis (PCA) – Section 6.6.2 – and to identify underlying structure by k-means clustering – Section 6.6.3. These methods are extensively used in data science and are ideal for processing of vast, heterogeneous and complex datasets (Jolliffe and Cadima, 2016).

Data Preparation 6.6.1

Before the mentioned methods could be applied, it is necessary to prepare the data by removing extreme outliers, which are typically measurement errors, from the dataset. However, removing only the extreme outliers is in certain cases not sufficient to obtain optimal results. In such cases, applying the machine learning methods only to a certain percentile of the dataset yields improved results.
After successful cleaning of the dataset, it is necessary to standardize each measurement characteristic while retaining the overall characteristic of the dataset. This standardization is performed using the so-called z-score transform as a standard scaler (Bronstein et al., 2008, pp. 799-803). The z-score for a datapoint x of a statistical population is calculated as follows:

$$z(x) = \frac{x - \mu}{\sigma} \tag{6.13}$$

Where μ is the mean of the population and σ is the standard deviation. Applying this z-score to all datapoints x of the population yields a distribution with a mean of 0 and unit variance. These properties greatly enhance the performance of machine learning and other statistical methods, some of which will be introduced in the next sections (Jolliffe and Cadima, 2016).

6.6.2 Principal Component Analysis

Due to the high dimensionality of the measured data, the so-called Principal Component Analysis (PCA) is used (Jolliffe and Cadima, 2016). This method is commonly employed when working on large datasets with multiple measurements per datapoint. The PCA linearly transforms the data into a new coordinate system where most of the datasets variation can be described with fewer dimensions. This greatly improves the ability to interpret and visualize such datasets by enabling a display of the data in, ideally, two dimensions.
An assessment of whether higher principal components can be safely discarded from further analysis is typically performed by inspecting the amount of variation per principal component.

6.6.3 K-Means Clustering

In order to split a large dataset into multiple sub-sets, called clusters, the method of k-means clustering is applied in this work. The subsets identified by this method can then be further examined, allowing the identification of similar properties of the data inside the cluster as compared to other identified clusters.
K-means produces a pre-chosen, fixed number of clusters. This is done by initially placing centroids μ_i for the number of chosen clusters S_i into random locations within the data (MacQueen, 1967). These centroids are then iteratively moved in order to find

$$L = \arg\min \sum_{i=1}^{k} \sum_{x \in S_i} \|x - \mu_i\|^2 \tag{6.14}$$

in order to minimize intra-cluster variance (ibid.). This results in a partition of the data into the desired number of clusters. This intra-cluster variance is also often referred to as a "cost" or "loss" for the clustering algorithm and can be used to determine how many clusters are reasonable to identify within the data.
Details on determination of the amount of clusters to be identified will be shown in Section 6.6.4.

6.6.4 Elbow and Silhouette Plots

Selecting the ideal number of clusters to be identified using k-means clustering is performed using so-called elbow and silhouette plots. These plots display different metrics for determination of the ideal number of clusters and will be described in the following.

Elbow Plot An elbow plot for the k-means clustering algorithm is generated using the overall loss metric, see Section 6.6.3, for a chosen number of clusters k. This overall loss is calculated for various k in order to generate a plot loss function vs. k. This plot typically displays a non-linear decline in the loss function with increasing k. Determining the ideal value for k is then performed by identifying the k_{elbow} which marks the "elbow" of the loss function, i.e. the

point which marks the inversion of the slope. Examples for this are found in the Appendix C.2, page 115.

Silhouette Plot Since the elbow plot on itself is not a precise measure — the point k_{elbow} can be difficult to identify — an additional metric is required. One such metric is called the silhouette score (Rousseeuw, 1987). By calculating this silhouette score for a given number of clusters k and generating a plot silhouette score vs k, see Figures in Appendix C.2.
For the calculation of the silhouette value $s(i)$ for a point i in cluster C_I, two measurements are needed. The first is the mean distance

$$a(i) = \frac{1}{|C_I| - 1} \sum d(i, j) \tag{6.15}$$

between a point $i \in C_I$ and all other points in C_I, where $d(i, j)$ is the distance between points i and j (ibid.). The next required measure is the minimum mean distance $b(i)$ of i to points in other clusters C_J:

$$b(i) = \min_{J \neq I} \frac{1}{|C_J|} \sum_{j \in C_J} d(i, j) \tag{6.16}$$

The silhouette value is then calculated using

$$s(i) = \frac{b(i) - a(i)}{\max\{a(i), b(i)\}} \tag{6.17}$$

The silhouette score is then referring to the maximum mean value of $s(i)$ over the entire dataset (ibid.).
The location of the maximum of this function in conjunction with the elbow plot is then used to identify the ideal number of clusters k_{elbow} for the given data.

Part II

Results

Chapter 7

Cellular Responses to Stimuli

This chapter of the results part focuses on the cellular activity in response to a stimulus with hPDGF. The activity is here measured as the proportion of cells expressing one or more CDRs at a time measured from the moment of adding the stimulant. This method yields a quick assessment of how cells are affected by the added growth factors.

In Section 7.1, a complete overview of the first and second stimulus as were introduced in Section 6.5, discriminated by added hPDGF concentration is given. As the results show, cells respond to the stimulus by increasing CDR expression, as was expected from literature. Interestingly, the rate of increase in cell activity is inverse to the added concentration, with the highest increase being observed at 10 ng/mL and the lowest at 30 ng/mL. The decrease in activity, however, does not depend on the concentration. For the control dataset without added hPDGF this, however does not hold true. For these cells, a reduction in activity after the stimulus is observed.

Inspecting an aggregation of all datapoints for the secondary stimulus shows no clear effect. This may be linked to the receptor internalization which occurs as part of the CDR process which was introduced in Section 3.2.2.

Discriminating between the individual datasets for the different delay times in Section 7.2 shows no dependency on concentration or delay time. This is surprising, but a hint towards the chosen delay times being too low. As will be discussed in this section, using longer waiting times imposes major reconsiderations onto the experiments, which will be further discussed in the outlook.

Further inspection of the previously observed suppression of CDR in the control dataset is done in Section 7.3. Here, the cell responses are split up by CDRs lasting longer or shorter than the median measured duration. A clear difference in cellular responses is visible.

In the following chapters of the results part, the focus will lie on a deeper inspection of how CDR expression is impacted by hPDGF, as well as a more detailed inspection of how individual cells are affected by the stimulus.

7.1 Cells Respond to hPDGF Stimuli by Expressing More CDRs

Upon stimulation, cells increase expression of CDRs after a delay of about 2 minutes as is visible in Figure 7.1 for four different concentrations of added hPDGF. The curves for 10 ng/mL, 21 ng/mL and 30 ng/mL display a clear increase in CDR activity, while the control set shows an initial decline. Interestingly, the maximum value of ruffle expression appears to decrease for higher concentrations with the peak for 10 ng/mL being highest. The onset of increased activity appears equal, with the rates of increase differing between the concentrations. Here again, the increase for 10 ng/mL is highest. Additionally, the location of the peak appears to shift to the right for higher concentrations.
The rate of decline in CDR activity appears to be equal among the three concentrations with all of them dropping below the basal activity of the control cells. Activity falling below the

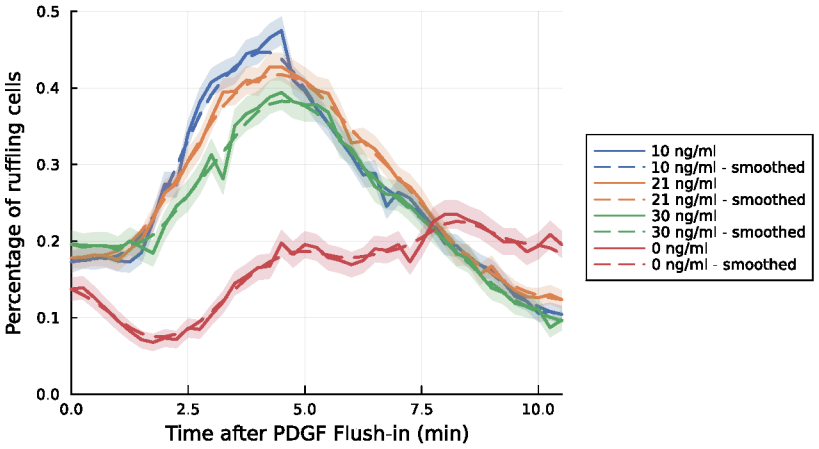

Figure 7.1: Cellular response to the initial stimulation with hPDGF measured as proportion of cells actively expressing CDRs. Cells begin to more actively express CDRs after receiving the stimulus which is applied at $T = 0$ min. Here, a hPDGF concentration of 10 ng/mL displays the highest effect with higher concentrations reaching lower activation levels. For the control set not receiving any stimulant, the cell activity drops to a minimum after 2 minutes. Ribbons indicate standard error.

control set can be explained by receptor internalization described in Section 3.2.2 rendering the cells less susceptible to stimuli. Interestingly, this appears to be equal for the three different concentrations, while the rate of increase was different between them. All three concentrations appear to be sufficient for internalization of the majority of RTKs.
Doing the same analysis for a secondary stimulus after a delay is shown in Figure 7.2, notably all different delay times are used in this figure. Individual delay times will be shown in the upcoming section. Here, all curves appear to be approximately equal, except for the 30 ng/mL signal remaining below the others. All four datasets display a decrease in CDR activity at around

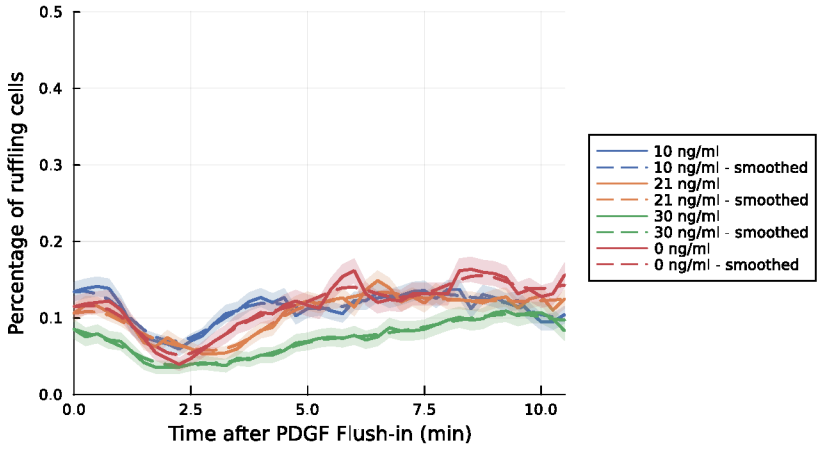

Figure 7.2: Cellular response to a delayed secondary stimulation with hPDGF measured as the proportion of cells actively expressing CDR. In comparison to the data shown in Figure 7.1 this dataset shows no clear response to the hPDGF stimulus. However, here the minimum in activity previously observed for the control dataset is present for data with delivered stimulant. This effect may point to an influence of the fluid flow on the activity of cells within the flow channel and may show a cellular adaption to the stimulant rendering them unable to respond again within the specified time frames. Y-axis is deliberately chosen in this scale to emphasize the difference when compared to Figure 7.1.

2 minutes, as was previously only observed for the control dataset.
The minimum of activity observed in both plots is most likely to be attributed to the cells experiencing drag forces due to fluid flow. However, the flow rate determined in Section 6.3.3 is significantly lower than what has been found to be of physiological relevance in literature, i.e. a flow rate of 1500 µL/s as compared to the here measured 11 µL/s (see Section 6.3.3) (Park, Joo, and Chen, 2018). Apparently, despite the very low flow rate, cells appear to still be affected by the fluid flow around them. Possible further experiments on this behavior will be discussed in the outlook chapter.

7.2 Delayed Secondary Stimulus after up to 40 Minutes has No Clear Effect

Splitting up the data for the secondary stimulus by delay time after the first hPDGF stimulus yields no clear results. An effect into reduction of activity, as was observed for the combined data in the previous section is slightly visible, which is still present when splitting the data up by delay time. However, no clear trend depending on delay time is visible, for an example see the data for 10 ng/mL in Figure 7.3. The figure here differs from the previously displayed ones in that the displayed values are relative to the value at $t = 0$ min in order to emphasize the effects. The remaining figures for other concentrations are found in the appendix, Section C.1 —

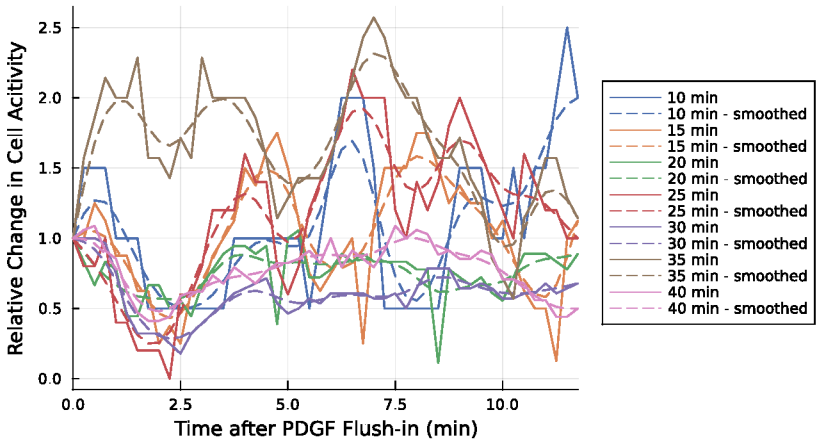

Figure 7.3: Change in cell activity relative to the value at $t = 0$ min for the second stimulus with 10 ng/mL added hPDGF, discriminated by delay time. The distinct minimum previously observed mainly for the control set is visible in all datasets. The brown line for 35 min initially increases at a higher rate than the remaining lines, but also displays a decrease in activity around 2 minutes.

page 113.

The reduction in activity up to around 2 minutes is clearly visible, with the brown line indicating a delay of 35 min differing by showing an initial increase in relative activity, but still showing a decrease in conjunction with the remaining data. The remaining figures in the appendix show similar behavior. After the initial decrease, activities appear to either remain stagnant or increase slightly, again with no evident dependency on delay time.

This could indicate usage of too low delay times, since reduction in sensitivity to repeated stimuli (Section 3.2.1) appears to hold on for longer than what has been tested (Lyashenko et al., 2020). This, however, would require a modification of the experimental sequence, since the cells would require a replacement of culture medium in order to provide optimal conditions for a longer period of time, reducing comparability to previously obtained data. A more detailed discussion of these modifications and requirements will be done in the outlook in Chapter 11.

7.3 Suppression of CDRs after Fluid Replacement Primarily Affects Short CDRs

Further inspection of the observed suppression of CDRs in the control cells to a minimum at around 2 minutes after the initial stimulus has been done by separating the dataset into CDRs lasting longer or shorter than the median duration of 1.51 min. A clear difference between responses to hPDGF stimuli can be observed for these two different types of CDR. Observing Figure 7.4 shows the difference in response to the initial stimulus for each concentration discriminated by CDRs with a duration longer (solid lines) or shorter (dashed lines) than the median

value.

It is clearly visible, that hPDGF stimulates cells to create longer lasting CDRs, while it appears

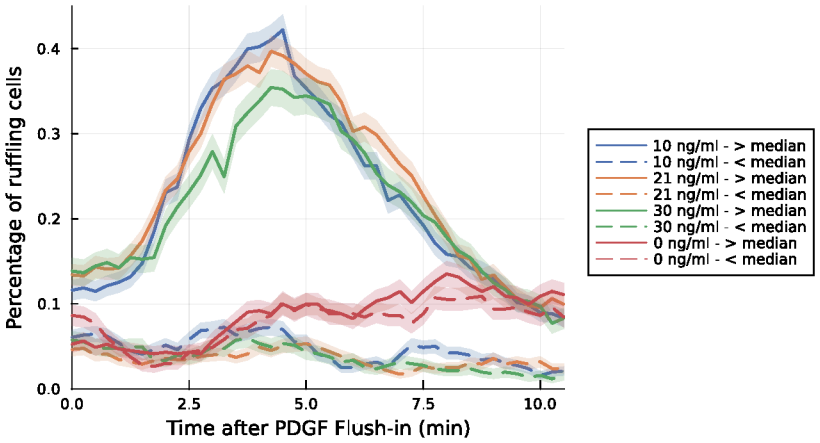

Figure 7.4: Cellular response to the initial stimulation with hPDGF measured as the proportion of cells actively expressing CDRs - split up by CDRs longer or shorter (dashed lines) than the median duration of 1.51 min. A very clear difference in cell activity depending on duration of the length of expressed CDRs is visible. While longer CDRs are clearly increased by adding hPDGF, shorter ones track the behavior of the control set up to around 4 minutes, with a decrease thereafter. This decrease coincides with the decrease in long ruffle activity. Ribbons indicate standard error.

to have almost no effect on creation of shorter lasting ruffles. All dashed lines appear to decrease to the observed minimum at about 2 minutes after replacing the surrounding cell medium, however for the control set (red lines) the activity increases again thereafter. Data for short CDRs with added hPDGF show a decline in activity in concordance with the decline in longer lasting CDR activity. The onset of decline in short CDR activity coincides with the onset of decline in long CDRs. An explanation for this can be receptor internalization as was described in Section 3.2.2.

Figure 7.5 shows the same analysis for the second stimulation. Here, there appears to be no significant difference between short and long lasting CDRs since all cellular responses follow a similar pattern. However, notably the activity for short CDRs appear to be lower for the higher hPDGF concentrations, with the 30 ng/mL being lowest.

This difference in response to growth factor stimulation will be further inspected in Chapter 8 on a per CDR basis and in further detail concerning individual behavior of cells in Chapter 9. Due to the low to non existing cellular response to the secondary stimulus, the following chapters will focus on the initial stimulus.

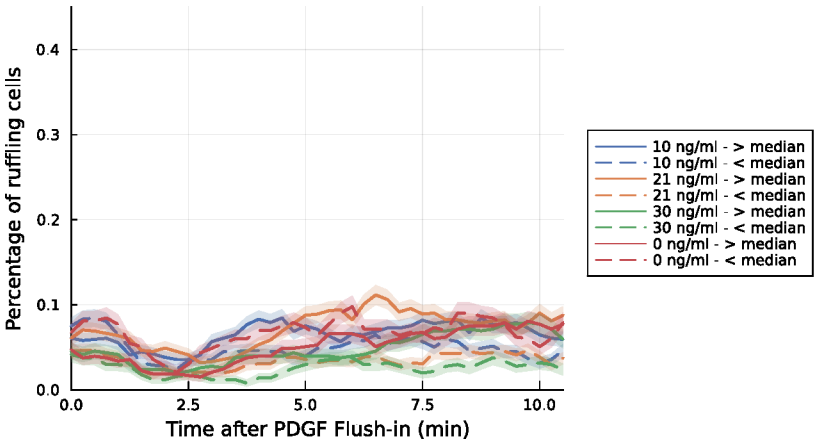

Figure 7.5: Cellular response to the secondary stimulus with hPDGF measured as the proportion of cells actively expressing CDRs - split up by CDRs longer or shorter than the median duration of 1.51 min. Data for all delay datasets combined. No clear difference between the concentrations is visible. Y-axis scaled for better comparability with Figure 7.4.

Chapter 8

Circular Dorsal Ruffle Dynamics

This chapter focuses on analyzing how hPDGF stimulation affects CDR motility. In Section 8.1, a deeper insight into CDR expression patterns depending on different hPDGF concentrations is obtained by firstly investigating how CDR duration and distance traveled are influenced by the growth factor, followed by a more narrow investigation of the findings through cluster analysis. The primary finding here is, that with increasing stimulant concentration, cells express more longer lasting, but mostly stationary CDRs. Section 8.1.1 shows a general increase in median CDR durations with added stimulant. With more refined inspection of the dataset, not only a trend towards longer durations and less motility is discovered, but also a less frequent induction of highly motile CDRs with very long durations and very large traveled distances.
Section 8.2 presents findings on the influence of lamellipodium width on CDR motility. Interestingly, there appears to be an optimal width for CDR propagation.

8.1 The Influence of Platelet Derived Growth Factor on CDR Motility

As described in Section 3.2.1, cells are stimulated to form CDRs by adding hPDGF to the medium. In order to achieve repeatable and precise stimulation, the microfluidic perfusion system was used to deliver the stimulant to the cells. The following subsections investigate the impact of different concentrations of hPDGF as a stimulant on the motility of CDRs.
Initially, in 8.1.1, a general trend in CDR durations and traveled distances will be investigated. As becomes clear from the data, adding growth factors to the medium increases mean CDR lifetime and duration with effects becoming more pronounced for higher concentrations. A more finely adjusted approach is then presented in Section 8.1.2. Here, the previously presented CDR data will be further analyzed by employing clustering methods described in Section 6.6.3, which are used to discriminate between different motility types of CDRs.
This two dimensional approach to investigating the effect differs from the method of focusing on CDR velocities used by other members of the work group (Bernitt, 2015; Lange, 2019). Investigating both dimensions allows for more fine grained insights into the influence on CDR

motility. Combining duration and distance into a velocity measurement would only show a shift to slower velocities, but would mask the trend towards longer durations for less motile CDRs.

8.1.1 Higher hPDGF Concentrations Increase CDR Duration and Reduce Distance Traveled

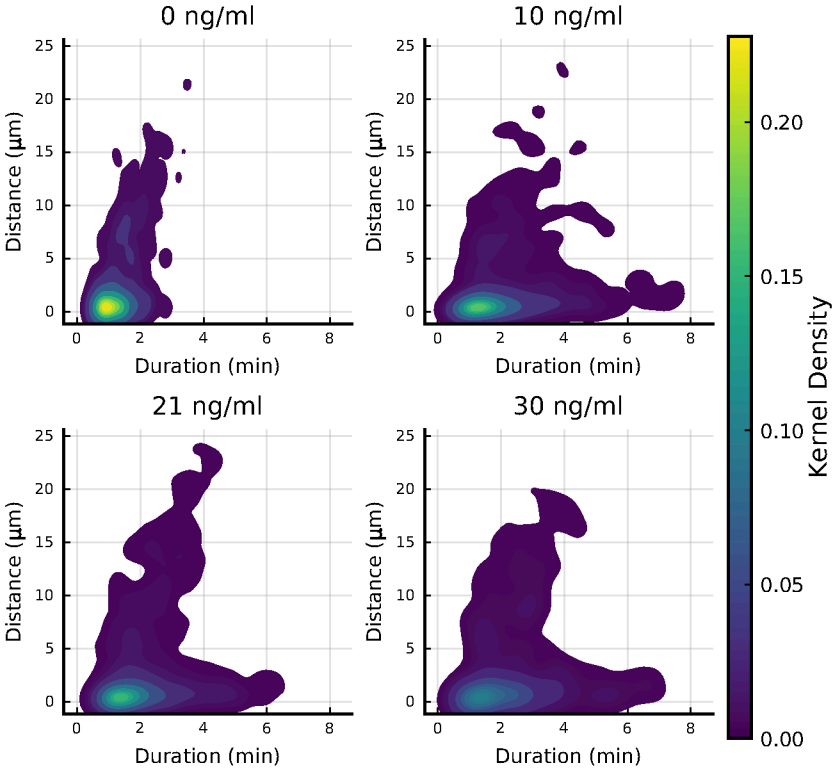

Figure 8.1: Kernel Density Estimation of CDR Duration versus Distance traveled for different concentrations of added stimulant during the first stimulus. For all added hPDGF concentrations a distinct difference from the control data at 0 ng/mL is visible in the shape of more quasi-stationary CDRs with higher durations. **Note:** The lowest contour level in this plot is not shown in order to enhance the visibility of the data shape.

Stimulating cells with different concentrations of hPDGF using the perfusion system results in a significant difference in CDR motility depending on concentration. Figure 8.1 displays the kernel density estimation of distance traveled and CDR lifetime for the initial stimulation of the experiment. The most striking difference is that the results with added hPDGF clearly deviate from the control set by an increased number of CDRs having longer lifetimes while traveling only very small distances. This shift is indicated by the extended "foot" of the displayed kernel density estimations. In addition to this extension at the bottom, the control dataset shows a more intense maximum for very short CDRs. The intensity at this location is reduced for increasing hPDGF concentrations. Figure 8.2 shows a comparison between typical CDR morphologies (a)

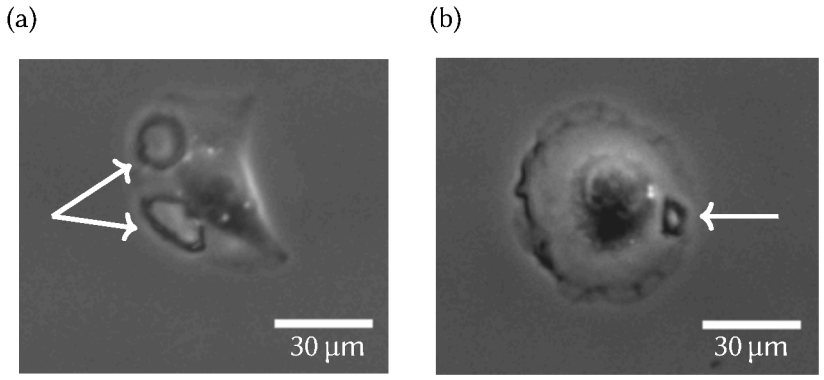

Figure 8.2: Example picture of the difference in CDRs expressed (a) with added hPDGF or (b) without. A clear difference in the size of the rings is visible, with the stimulated CDRs being significantly larger in diameter.

with and (b) without added hPDGF. The actin rings with added hPDGF are significantly larger in diameter than the passively occurring CDR. This larger size appears to correlate with decreased motility as is visible in the presented data. Isolating only the CDR lifetimes and inspecting the

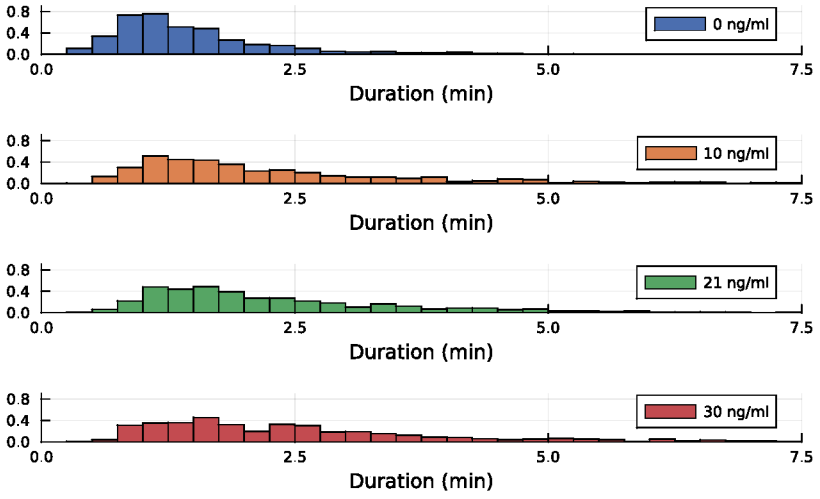

Figure 8.3: CDR lifetimes for different concentrations of hPDGF during the first stimulus. A clear trend towards longer durations is visible with distributions becoming wider for higher concentrations. This visible trend is backed up by increased median durations as shown in Table 8.1.

distribution for the different hPDGF concentrations, displayed in Figure 8.3, displays a distinct shift towards longer lifetimes with higher stimulant concentrations and the corresponding histograms get visibly wider. Table 8.1 reinforces the visible shift by displaying a significant increase in the median CDR lifetime with higher stimulant concentrations.
This trend will be further analyzed in the next section.

Table 8.1: Median CDR lifetime for varying added hPDGF concentrations during the initial stimulus. A clear shift towards longer lifetimes with higher stimulant concentration is visible. The hPDGF concentration of 0 ng/mL indicates control experiments.

hPDGF Concentration ng/mL	Median CDR Lifetime min	CDR Lifetime Variance min
0	1.1	2.1
10	2.22	3.12
21	3.1	1.1
30	4.4	0.1

8.1.2 Cluster Analysis of CDR Motility Reinforces Findings about increasing CDR Durations

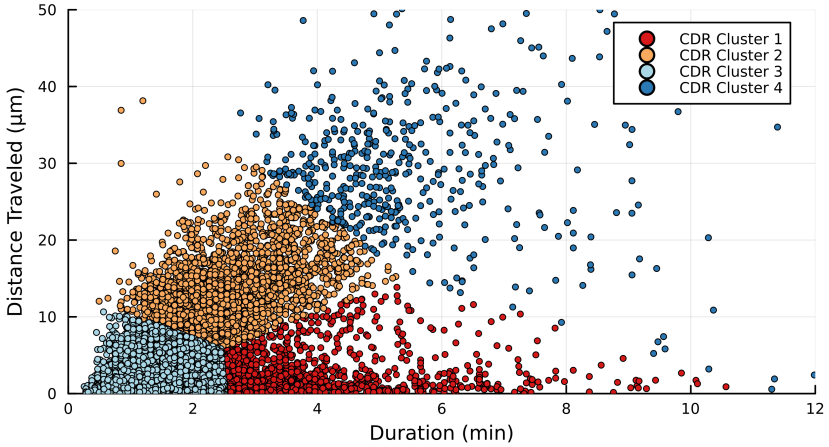

Figure 8.4: Overview of CDR clusters determined via k-means clustering. Clusters 2,3 and 4 clearly show an increase of distance traveled with higher CDR lifetimes. Cluster 1 is best suited to identify quasi-stationary CDRs traveling low distances despite long lifetimes. However, the outliers with the longest durations are assigned to cluster 4. Identification of clusters was performed on the full set of all CDRs.

The distribution densities of CDRs displayed in the previous section indicate a clear trend towards CDRs with longer lifetimes and low distance traveled with added hPDGF stimulus. In order to discriminate between different CDR behavior patterns the statistical method of k-means clustering, introduced in Section 6.6.3, is applied to the distribution. This methodology allows for identification of different patterns within a dataset. Despite the distribution of CDRs not displaying a visibly clear cut between different clusters, it is possible to identify multiple different clusters of similar properties within the dataset.
Figure 8.4 indicates the clusters determined from the full dataset of all measured CDRs. Determination of the number of clusters to identify was performed using a combination of an elbow and silhouette plot, displayed in the appendix C, Figure C.4 — see Section 6.6.4 for details.

This analysis yielded a number of four clusters to be discriminated within the dataset. By identifying these four clusters within the dataset, it is possible to determine differences in CDR behavior within these clusters by comparing the distributions of the underlying characteristics, i.e. duration and distance traveled. Comparing Figures 8.1 and 8.4, it becomes clear that cluster 1 is indicative of the largest effect of added hPDGF, since it comprises the long duration but low distance CDRs.

Comparing the relative CDR population of each cluster for the varying concentrations of hPDGF, as shown in Figure 8.5, makes the difference between no added stimulant and added stimulant apparent. By adding hPDGF as a stimulant, a larger proportion of the CDR population is shifted towards cluster 1. Interestingly, the relative population of cluster 4 is also increased for all nonzero concentrations of hPDGF, however to a significantly lesser extent than the effect on cluster 1. This shows that not only long lasting stationary CDRs are amplified by adding a growth factor stimulus, but also long lasting very motile CDRs. Only the data for 10 ng/mL shows a significant impact on cluster 2, comprising CDRs of medium motility. For all nonzero growth factor concentrations, the population of cluster 3, being short lasting quasi-stationary CDRs, is reduced when compared to the control data.

Further inspection of the distributions of CDR duration and distance traveled for each CDR cluster, see Figure 8.6, does indeed support the aforementioned classifications. Clusters 2 and 4 both contain motile CDRs, inspecting their respective velocity distributions shows an increase in median velocity and a wider distribution of velocities for CDRs contained in cluster 4 as compared to cluster 2. This result is surprising, since the initial result was that added hPDGF

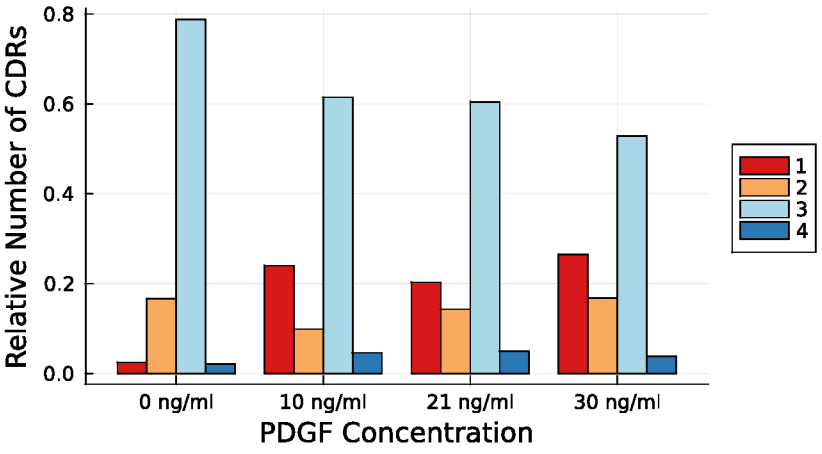

Figure 8.5: Relative population of CDR clusters after initial stimulation with hPDGF. With the majority of CDRs occupying cluster 3, the difference between the control set and the sets with hPDGF being present is most visible in the higher occupation of cluster 1. This clearly shows the trend towards CDRs with longer durations and less distance traveled when cells are being stimulated with hPDGF.

reduces CDR motility while increasing duration. The aforementioned increase of cluster 4 pop-

ulation does hint towards another possible, albeit less likely, effect of growth factor stimulation is induction of highly motile CDRs with, on average, marginally higher propagation velocities.

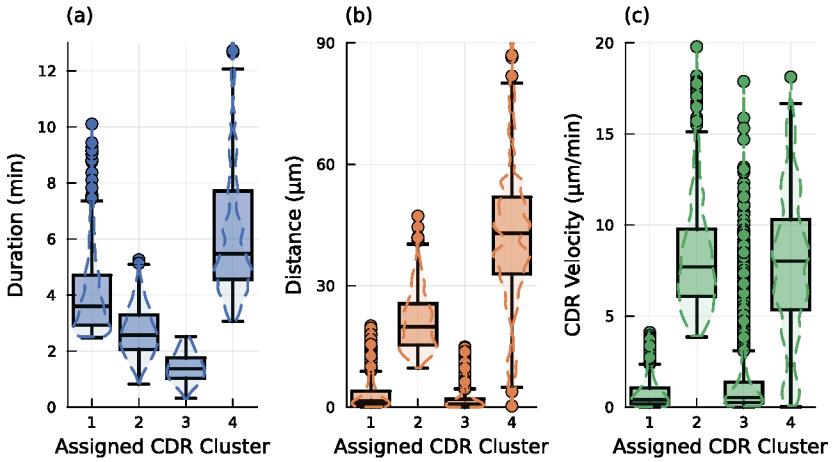

Figure 8.6: Boxplots with overlaid violin plots of (a) CDR duration, (b) distance traveled and (c) velocity for the four CDR clusters during the initial stimulation. A clear difference for each cluster is visible, with cluster 1 comprising the long lasting stationary CDRs, cluster 2 the CDRs of medium motility, cluster 3 showing only very short and stationary ruffles and finally cluster 4 containing very motile, very long lasting circular actin waves.

8.2 Optimal Width of Lamellipodium for CDR Motility

Since the lamellipodium of adherent cells is the area where CDR formation takes place, the influence of the lamellipodial width on CDR motility has been investigated. Despite the cells being forced into controlled circular shapes by means of microcontact printing, individual cells vary in size. Some cells extend past the microcontact, whereas other cells are imperfectly attached to it. For many cells, the nucleus is not perfectly centered, causing an imbalance in lamellipodium width along their circumference.

By not only evaluating cells with ideal geometric properties, i.e. perfect circular shape and the nucleus being localized in the center, the collected dataset includes cells displaying variable lamellipodium widths along the arc length of their circumference. Due to the CDR data being collected as circular kymographs around the cell nucleus, CDRs traveling around the nucleus are subject to a variation in lamellipodial width along their path.

Measurement of lamellipodial width was performed by segmenting microscopy images into background and cell with the cell nucleus being identified, too. The most robust process for this was found to be an approach based on neural networks using the U-net model as described in Section 6.4.4.

The mean lamellipodial width along the arc length appears to have an optimal width for CDR motility at the mean lamellipodium width of $(13.82 \pm 0.03)\,\mu m$, as shown in Figure 8.7. The data

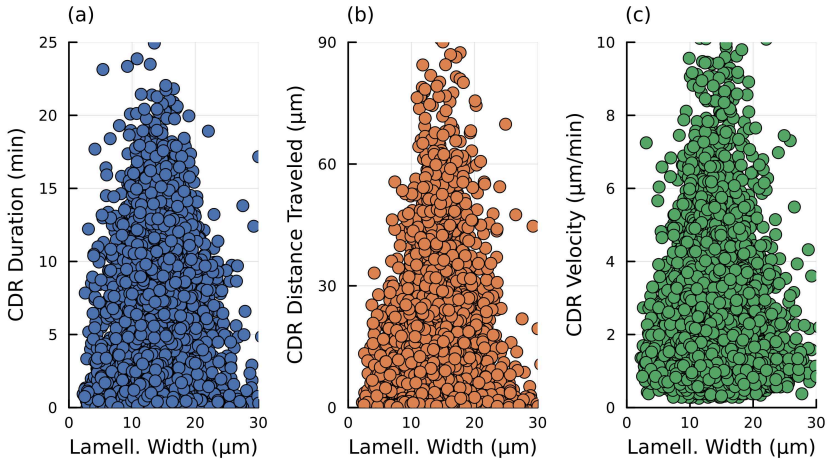

Figure 8.7: Effect of lamellipodium width on (a) CDR duration, (b) distance traveled and (c) velocity. The primary visible effect is that both the most frequent and maximum values for each measurement are bunched around the mean lamellipodium width of $(13.82 \pm 0.03)\,\mu m$.

in Figure 8.7 shows that variance in path width does not impact the CDR characteristics distance traveled and lifetime and in combination of the previous two the propagation velocity, aside from providing apparently optimal width at the aforementioned mean value. Wider or narrower lamellipodia appear to greatly reduce motility of CDRs.

The area for the used microcontacts of $3000\,\mu m$ was chosen due to cell area distribution measurements performed by Erik Bernitt (Bernitt, 2015). Since this was the most frequent value for the area of randomly spread cells, it was chosen for the circular microcontacts. The novel data here shows, that for CDR motility this area provides an optimal width except for some outliers. Seemingly, a more narrow lamellipodium does not provide sufficient area for a CDR to migrate, while a more wide lamellipodium hinders propagation by allowing for a more stationary ruffle.

Chapter 9

Morphological Cell States

The NIH3T3 murine embryonic fibroblasts used for the experiments in this work display a high variability of possible dynamic states classified by their morphology and CDR expression. Since the internal state in the cell cycle of each cell cannot be determined during live microscopy, due to it being governed by protein concentrations within the cell (Alberts et al., 2015, Chapter 17). Such morphological states were chosen as a hint towards internal processes of the cell, despite being arbitrary. Gathering such states from a sufficiently large dataset, however, does allow for deeper insight into cellular reaction patterns when compared to findings in Chapter 7.

Attempts to synchronize the cell cycle phase through the wide spread method of serum deprivation, also called starvation, of cells (Pirkmajer and Chibalin, 2011) was unsuccessful due to the cells being isolated from other cells on the FN microcontacts. Starvation in this context is replacing culture medium with medium containing little to no nutrients such as FBS. Prolonged isolation in combination with starvation causes individual cells to go into apoptosis, rendering this method unsuitable for the used experimental setup (Kulkarni and McCulloch, 1994; Paddenberg et al., 2001). This effect of the method greatly reduced the number of viable cells per experiment and was therefore discarded as an approach to synchronize individual cell cycles across the plated cells.

Synchronizing all cells into the same cell cycle phase would be beneficial due to the protein configuration within individual cells within the same experiment being equal, however with current protein concentrations within cells unknown upon initiation of experiments, another classification approach was needed. Data acquisition and evaluation was mainly done using an optical microscope, therefore morphological properties and CDR expression patterns were used to identify different cell behavior classes as will be layed out it Section 9.1. The given measurements are then analyzed using methods of PCA for dimensionality reduction and k-means clustering as introduced in Section 6.6.

Evaluation of these identified behaviors which are classified as clusters or cell states, yields information on how likely cells are to react to an external stimulus by hPDGF added to their culture medium. This cell state investigation is described in Section 9.2, where an analysis of the

probability for cells changing their cluster upon a stimulus is done. As will become evident from the data, cells which are actively expressing CDRs are more likely to stop expressing ruffles or reduce ruffling activity, while cells which are not actively ruffling are stimulated to do so. This behavior could hint towards the underlying molecular machinery being pushed towards other fixed points in the scope of viewing them as a dynamic reaction-diffusion system, as was described in Chapter 4.

9.1 Identification of Cell States

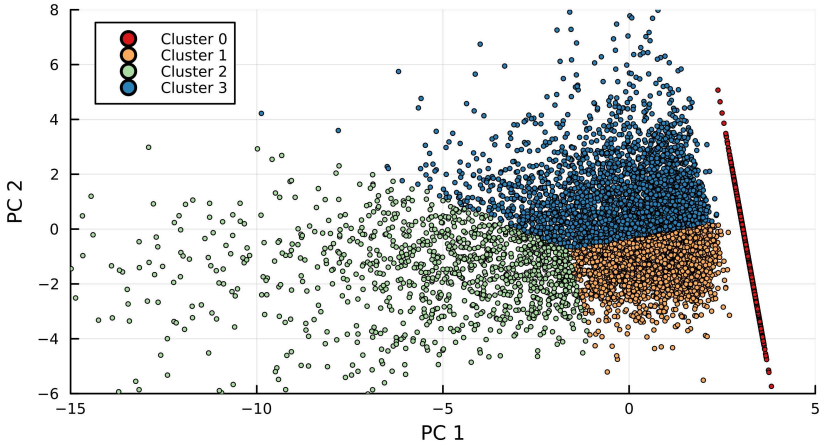

Figure 9.1: Principal component analysis of cells based on mean lamellipodial width, mean CDR duration and mean CDR distance. Using k-means clustering, 4 clusters were identified in order to discriminate between different ruffling activity patterns of the cells. Axis labels indicate their respective principal component abbreviated as "PC". By investigating the PCA loadings, see Figure 9.2, it is obvious that PC 1 is most influenced by mean CDR width and duration, whereas PC2 scales with mean lamellipodial width.

In order to split up the timeline of each cell into multiple time frames, the data of each cell was separated by experiment block, as introduced in Section 6.5. Using this approach enables detection of changes in cell behavior upon modification of the chemical surroundings of the cell, since during each experimental block the chemical conditions in the flow channel remain equal. The metrics used for identification of cell states were extracted from microscopy data for each cell. The selected metrics for this were the mean lamellipodial width, mean CDR duration, mean CDR distance traveled, as well as the frequency of CDR expression for each cell.
These measurements were chosen due to them being a good indication of changes in cellular responses to external stimuli. Observations in Chapter 8, especially in Section 8.1.1, of cells expressing larger, more immobile and longer lasting CDRs with increased hPDGF concentrations made duration and distance traveled prime candidates for this analysis in order to hint at systematic changes in the cell. For both values the mean value for all CDRs expressed by the cell

during the given time span was calculated. The frequency of newly formed CDRs additionally indicates cell activity in this context. The mean lamellipodium width of the cell was chosen due to some cells expressing a contraction or expansion of the lamellipodium in response to hPDGF stimuli, hence measuring changes in width indicates cellular reaction (Pierce et al., 1991).
The method of PCA, as introduced in Section 6.6.2, was used for reducing the dimensionality of the used four dimensional dataset. By reducing the high dimensional dataset to a two dimensional plane, discrimination between certain cellular states is simplified. Figure 9.1 displays this plane and the clusters identified using k-means clustering, to be noted here is that inactive cells were automatically assigned to cluster 0. The number of clusters to be identified via the k-means algorithm was determined with elbow and silhouette plots which were introduced in Section 6.6.4. These plots are displayed in appendix C — Section C.2.2. Furthermore, in order to view which input scales the returned principal component values the most, the calculated PCA eigenvalues can be displayed like in Figure 9.2.[1]. Prinicpal component 1 is primarily influenced by mean CDR duration and distance, whereas principal component 2 is mostly determined by mean lamellipodium width and CDR frequency. By investigating the distributions of the input

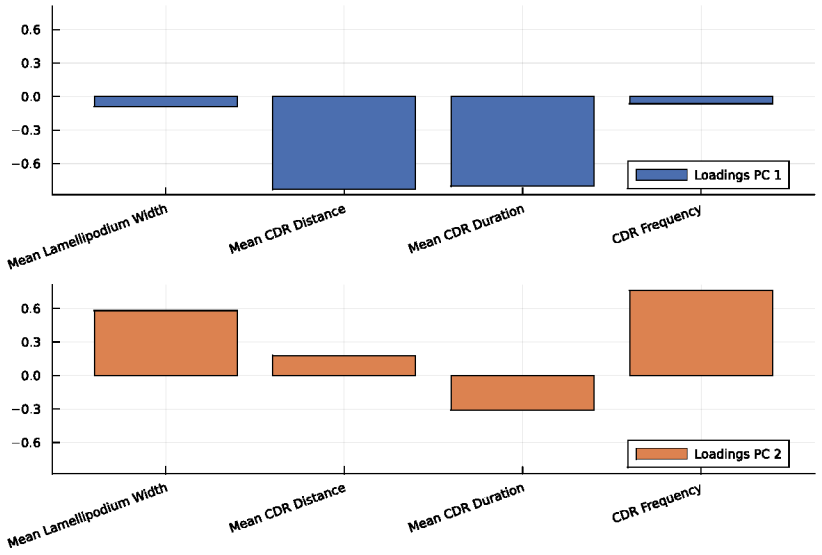

Figure 9.2: PCA loadings for the analysis shown in Figure 9.1. These loadings can be used to asses which input measurements have the greatest influence on each principal component. PC 1 is clearly mostly influenced by mean CDR duration and distance of each cell, while lamellipodium width and CDR frequency have a larger impact on PC 2.

characteristics within each cluster it is possible to assign each cluster a meaning.
These distributions are displayed in Figure 9.3 as boxplots with overlaid "violin" plots in order to show properties such as median value, 25th and 75th percentile and to visualize the shape of each distribution. Cluster 0 is, as expected, most easily identified as inactive cells, meaning cells

[1]In the context of PCA analysis the values shown in such plots are often referred to as "loadings"

currently not expressing any CDRs. Higher number clusters range from cells showing what is hereafter referred to as "typical" or "normal" CDR activity which are identified via clusters 1 and 3, with the main difference between 1 and 3 being the lamellipodial width. Cells in cluster 2 are denoted as highly active due to the main differentiation to all other clusters being determined to be longer CDR durations and distances, however at a lower frequency than cluster 3. The

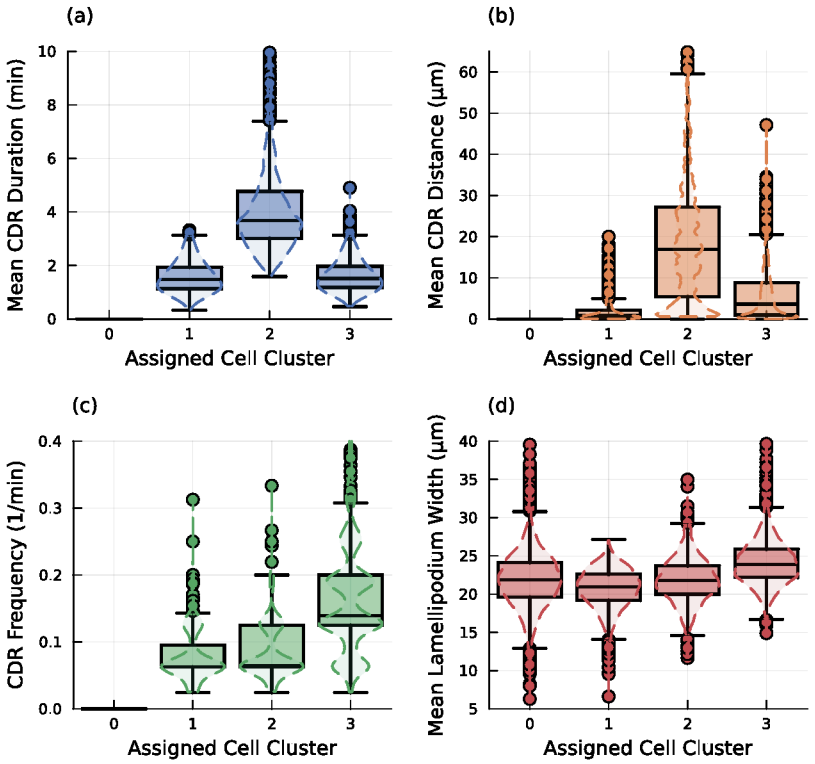

Figure 9.3: Distribution of the four input metrics for each assigned cell cluster. (a) Mean CDR duration. Clusters 1 and 3 appear to have equal distributions with cluster 2 expressing significantly longer lasting CDRs. (b) Mean CDR traveled distance. This metric appears to divide the set of all cells into cells expressing more stationary CDRs in cluster 1, very motile CDRs in cluster 2 and low motility in cluster 3. (c) Frequency of CDRs. A trend towards higher frequencies from clusters 1 to 3 is visible, however the difference between cluster 1 and 2 is mostly a wider distribution with median values being very similar. (d) Mean lamellipodium width of cells again shows an increase from cluster 1 to 3, with median values increasing. Boxplots are overlaid with violin plots to indicate the shape of each distribution.

following sections will focus on the changes of which cluster individual cells occupy before and after stimulation with hPDGF and the effects of different concentrations thereof.

Cell State Transition Probabilities 9.2

Quantification of cell state dynamics was performed by analyzing the probabilities of cells transitioning from one activity cluster to another after an external stimulus. Evaluation was performed for each cell individually. The dataset used for clustering was split into the different experiment blocks, as described in Section 6.5. Therefore a set of 4 transitions is available to be investigated:

1. DMEM ⟶ DMEM + hPDGF
2. DMEM + hPDGF ⟶ DMEM
3. DMEM ⟶ DMEM + hPDGF
4. DMEM + hPDGF ⟶ DMEM

Stimulation of cells happens at transitions 1 and 3, also referred to as experiment blocks 2 and 4, since this is where cells are exposed to culture medium with added growth factors. The experiments are set with a delay, i.e. varying duration of the experiment block with only DMEM after the first stimulus. However, due to findings in Section 7.2, the focus here lies entirely on the first stimulus, since the effects after delayed stimulation were unclear and require modifications to the experimental setup for further research, which will be discussed in Section 11.2.

Cells Actively Expressing CDRs Prior to Stimulation are Inhibited by Stronger hPDGF Stimuli 9.2.1

Due to the initial stimulus being the first section of the experiments where cells are exposed to the hPDGF stimulus, the most substantial cellular reaction is expected to happen at this experiment transition. In order to visualize the effect on cells, the state of each cell before and after the transition was determined. With this, 16 possible state transitions could be identified. A heatmap of probabilities for each transition in dependence of hPDGF concentration is shown in Figure 9.4.

The most distinct difference between the control data (0 ng/mL) and the stimulation data is a higher probability of cells to remain in their initial activity cluster. With increasing stimulant concentrations, the probability to remain in the cluster before the stimulus decreases, indicated by the diagonal of each heatmap. Another striking difference between the control data and the nonzero hPDGF concentrations is the strong reduction of cells remaining in cluster 3. Recalling Figure 9.3, this cluster contains cells expressing normal motility CDRs at a higher frequency.

An alternative presentation of these cluster transitions is shown in Figure 9.5. Here, the percentages of cells switching into higher or lower activity clusters and not switching cluster is classified by assigning a qualitative activity to each cluster and shown for all concentrations at the initial experiment block transition. Activities were ranked by observed CDR expression frequency. The majority of cells in all concentrations remain in their corresponding qualitative activity before the stimulation event. This value changes with added hPDGF, depending on the

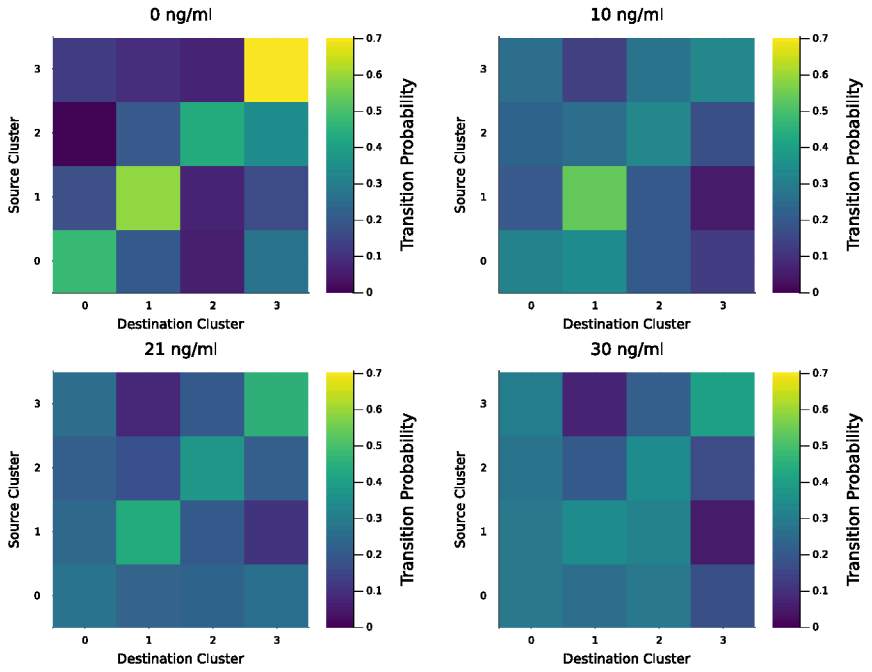

Figure 9.4: Transition probabilities from source cluster to destination cluster for cells on the first hPDGF stimulus. Stimulant concentration is indicated above each subplot. The source cluster indicates the assigned cell cluster before the stimulus, whereas the destination cluster is the assigned cell cluster after the stimulus. For the control set and the lowest concentration of 10 ng/mL a tendency for cells in cluster 1 to remain in that cluster is visible. Another striking difference between control data and all stimulated cells, is that for the control set, cells were significantly more likely to remain in cluster 3 than to transition to other clusters. This probability is reduced for higher concentrations, where more cells tend to get inactive upon stimulation. The color coding for all four sub-figures is equal in order to enhance inter comparability.

concentration. All displayed classifications show concentration dependent trends. A switch to lower activities is more likely with higher hPDGF concentration. Consistently, it is less likely for cells to not change their activity with increasing stimulant concentrations. A transition to higher activities appears to not be significantly impacted by added stimulant. There appears to be a trend, but no definitive conclusion can be drawn since variations between concentrations remain within the standard error.

Recalling the interpretation of the CDR machinery as a dynamic reaction diffusion system as described in Chapter 4 — Section 4.1, this behavior of cells becoming inactive or less active can be interpreted as the active cell being pushed away from a fixed point by the external stimulus. Likewise, cells increasing their activity may be pushed towards a fixed point allowing for increased activity.

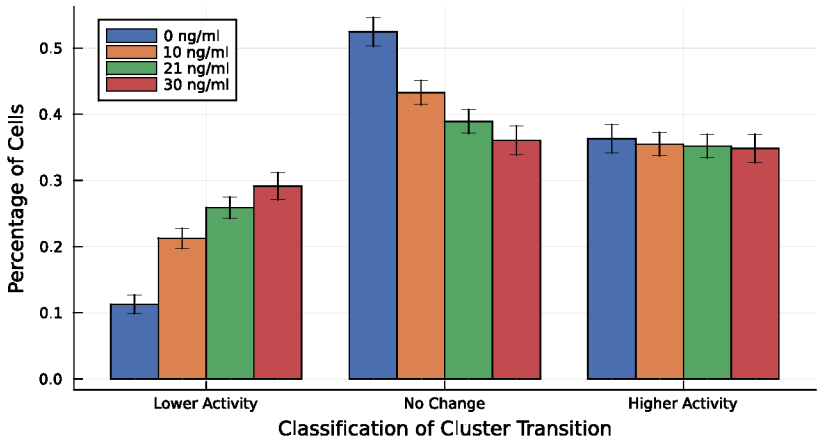

Figure 9.5: Classification of cell migration between clusters in terms of CDR activity on experiment transition 1. Shown is the percentage of cells migrating into a cluster with higher activity, lower activity, or remaining in their initial cluster (no change). Color coded is each concentration of hPDGF. With added stimulant, a lower percentage of cells remains in their initial cluster. Compared to the control data, a higher percentage of cells switches into a higher activity cluster, where the percentage is similar for all added hPDGF concentrations. Higher percentages of migration to lower activity clusters is observed with added stimulant. Errorbars show standard error.

9.2.2 Cells Remaining in Initial Cluster

In contrast to cell transitioning between the determined clusters, a subset of cells remained in their initial cluster after stimulation. These cells are apparently unaffected by the stimulus and in a relatively stable state. Figure 9.6 displays the relative amount of cells remaining in their initial cluster for four different concentrations of hPDGF. With the highest amount of cells not changing the cluster being observed for 0 ng/mL, a distinct decline is shown with non-zero hPDGF concentration. Yet, there appears to be no clear dependency on concentration for this behavior, since within standard error, differences for each hPDGF concentration are negligible. Further inspection of this behavior warrants for more hPDGF concentrations to be included, especially lower than 10 ng/mL. This additional data may uncover a saturation curve like decline in unaffected cells. Further discussion on possible extended experiments will be done in the outlook.

In the scope of understanding the CDR machinery as a reaction diffusion system, this behavior may imply actively ruffling cells to stay close to the fixed point where CDRs are possible. With higher concentrations, the chemical conditions are more likely to push the system away from that point, therefore reducing the number of cells staying in their initial cluster. As mentioned above, some cells are however able to return to their active fixed point.

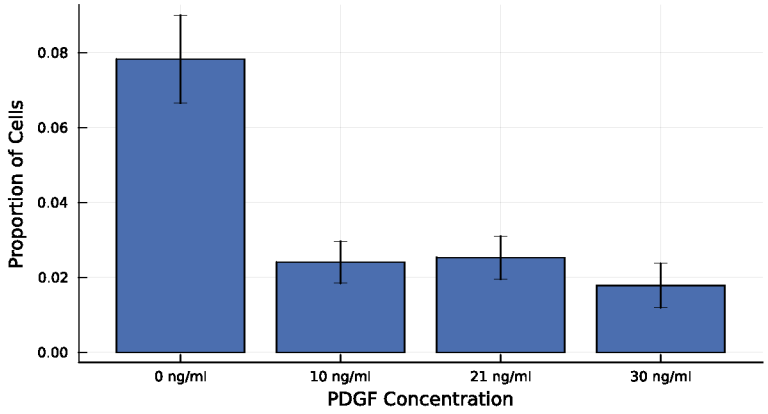

Figure 9.6: Relative number of actively ruffling cells remaining in their initial activity cluster. With added hPDGF, significantly fewer cells remain in their initial cluster. Around 2 % to 3 % of cells seem to be very stable in their initial state and appear to not be affected by the external stimulus. Error bars show standard error.

Chapter 10

Conclusion

The data obtained from single cells on printed FN microcontacts inside a perfusion system allowed for collection of a large amount of data. Forcing cells into pre-determined shapes and locations allowed for considerable automation in the extraction of data from microscopy images. The forced circular shape of cells, first introduced into the workgroup by Erik Bernitt based on the protocol by Théry and Piel, 2009, greatly improves evaluation of individual CDRs by creating a circular lamellipodium of, ideally, equal width along the circumference of the cell. This provided CDRs with a one dimensional propagation path, reducing the complexity of extracting CDR duration or distance traveled.

In addition, the ability to use a programmable perfusion system enabled repeating experiments with exact repetition of stimulation times without interrupting image acquisition. Image metadata in combination with perfusion system log files allowed for very precise alignment of stimulation events with the recorded images. This greatly improved accuracy of evaluation steps following certain events during the experiment.

The total number of single cells imaged and evaluated in this study amounts to 2548, while the total amount of individual recorded CDRs is 16 663. This very large dataset enables more precise insight into behavior of individual cells, as well as CDR expression patterns in general. For each cell, the individual morphology has been extracted from images using a convolutional neural network, introduced in Section 6.4.4, which greatly reduced the effort required in image segmentation. Especially with phase contrast microscopy rendering artifacts imposing challenges for conventional computer vision methods, such as simple threshold based attempts. In addition, the system also handled slight defocus due to thermal drifting of the microscope gracefully and more robust than approaches using active contours. Without the efficiency of this method and especially the employed U-net by Ronneberger, Fischer, and Brox, 2015, which yielded very good results with minimal required training data, evaluating each imaging frame for each cell would have required substantial amounts of time.

The results obtained using these approaches will be recapitulated in the following sections.

10.1 Cellular Response to Growth Factor Stimulation

Investigation of how cells generally react to hPDGF stimulation was performed by assessing which proportion of cells was actively expressing CDRs after adding the stimulus using the perfusion system.
For the first stimulation, the overall data showed a clear increase in activity for all non-zero stimulant concentrations, see Section 7.1. Interestingly, the time and magnitude of peak activity differed between concentrations with 10 ng/mL causing the earliest and highest peak, with 21 ng/mL and 30 ng/mL following. All three datasets showed similar rates of decline in activity after the peak was reached. In contrast to this, the control dataset for 0 ng/mL showed an initial decline in activity to a minimum at 2 min with a subsequent increase in activity to slightly higher levels.
Applying the same analysis to the secondary stimulation, initially including all different delay times into the same data, showed no increase in activity for all used concentrations. This lack of a reaction may be a hint towards cells having adapted to the external stimulus by RTK internalization (Lyashenko et al., 2020) or the selected recovery times being too low. For this secondary stimulus, all datasets showed a decline in activity after the fluid replacement in concordance with the previously observed minimal activity after 2 min. This reduction in activity is therefore suspected to be caused by the fluid flow involved in replacing the culture medium with stimulant carrying medium, which will be further discussed in the outlook.
Discriminating the second stimulation event by delay times from 10 min to 40 min in steps of 5 min in Section 7.2 showed no clear dependency on concentration, strengthening the aforementioned assumption of too low recovery times and effective adaption to the stimulant.
Further inspection of the initial drop in activity observed in the control data and the secondary stimulus in Section 7.3 was done by splitting the data up by CDRs lasting longer or shorter than the median duration of the dataset. This analysis showed that mostly the expression of short lasting CDRs is reduced after the stimulus, while the activity for longer lasting CDRs increases.

10.2 CDR Dynamics Depending on hPDGF Concentration

The observation that added hPDGF causes cells to express more longer lasting CDRs lead to further inspection of CDR dynamics. In Section 8.1, the influence of different growth factor concentrations on the dynamics of expressed CDRs was analyzed. By measuring individual durations and traveled distances, it became clear that a primary effect of growth factor stimulation is the expression of longer lasting, less motile CDRs. This effect increases with hPDGF concentration, which is confirmed by increasing median CDR durations.
Deeper inspection of CDR dynamics was performed using cluster analysis in Section 8.1.2. Here, the total dataset of CDRs was split up into four clusters using the k-means algorithm. This arbitrary partition of the duration-distance dataspace was then used to investigate the population of different clusters of CDR motility depending on hPDGF concentration.

This analysis confirms the tendency towards longer lasting, less motile CDRs with added growth factor. Another result of the cluster analysis is that added hPDGF also marginally increases the amount of very motile CDRs, which express the longest durations and largest traveled distances. Further inspection of the underlying distributions of CDR duration, traveled distance and in combination propagation velocity showed these CDRs to also propagate at marginally higher velocities. This result, however very rare, strongly contrasts the general trend towards less motile ruffles with increased growth factor stimulation.

Influence of Lamellipodium Width on CDR Motility 10.3

With cell morphology measured for every cell, it was also possible to assess the influence of lamellipodium width on CDR motility in Section 8.2. This was done by evaluating the previously used measurements of CDR duration, distance and velocity in dependency of the mean lamellipodium width along the propagation path of each individual CDR.
Interestingly, there appears to be no clear functional relation between lamellipodium width and CDR motility. The main finding here, is that the mean lamellipodium width of $(13.82 \pm 0.03)\,\mu m$ provides ideal conditions for CDRs to propagate. The most motile ruffles in the dataset accumulate around this value, with only few outliers at wider lamellipodia. Apparently, a more narrow lamellipodium impairs movement, while a wider one facilitates local expansion of the actin ring.

Cell States implied by Morphology and CDR Dynamics 10.4

Further insight into cellular behavior depending on growth factor concentrations has been obtained by performing statistical analysis of individual cells over the course of their respective experiments. This was done by using key measurements for cellular ruffling activity, i.e. mean CDR duration, mean distance traveled, frequency of CDR expression, as well as their mean lamellipodium widths. In order to reduce the dimensionality of this dataset, a principal component analysis, see Section 6.6.2, was performed reducing the four dimensions into two.
Subsequent k-means cluster analysis yielded different clusters of cellular activity. Classification of the found clusters by their respective CDR activity properties was done by investigating the underlying distributions of input measurements for each cluster. This, of course, yielded no activity for the cluster containing inactive cells. The other clusters were then identified to consist of cells with what was deemed regular activity, or high activity, depending on the mean values for duration, distance and CDR frequency.
Changes in cellular behavior upon addition of an external growth factor stimulus was then performed by investigating the cluster a cell was occupying before and after the stimulus was added. By calculating the probabilities of cells transitioning from one cluster to another, depending on added hPDGF concentration, yielded the insight that a primary effect of growth factor stimulation is pushing actively ruffling cells into lower activity clusters.

This result is counter intuitive, since the expectation for adding a stimulant would be increased activity of cells. In agreement with previous findings of cells expressing more long lasting, stationary ruffles with added growth factor, however, it becomes clear that one impact of the stimulus is a reduction in CDR frequency. The frequency is a key measurement for the qualitative cluster classification, hence lower frequencies in this case coincide with lower activity. On the other hand, observations in the raw data do show many cells actively expressing CDRs before a stimulus ceasing to do so after the stimulus is added.
Again, interpreting the cellular CDR signaling machinery as a reaction-diffusion system in a fixed point promoting CDR formation means that the stimulus may perturb the cellular system sufficiently for it to not be able to return to said fixed point.
Another investigated point is cells not changing their activity cluster upon stimulation, which shows a stark difference between the control data and the non-zero added concentrations. As was expected from the previous findings, cells are more likely to change their cluster upon stimulation. Future experiments on this behavior will be further discussed in the outlook.

10.5 Relevance of Dataset Size

A key factor during this study was maximizing the amount of collected data. As was laid out in Chapter 6, most of the considerations that went into designing the experimental setup and analysis tools were aiming to increase the amount of data per experiment and increase efficiency of data extraction from experimental results.
This attention to large datasets resulted in overall 2548 cells and among them 16663 CDRs being recorded and evaluated. This very large amount of data yielded results which would have gone unnoticed with smaller datasets due to them disappearing in the large variance inherent to biological systems. Additionally, documenting the origin of each cell and CDR datapoint allowed for a more fine grained analysis of cellular behavior. During this study, each cell, as well as every CDR extracted from that cell, was given a unique identifier which enabled the aforementioned tracing of every data point.
Further improvements to this system will, of course, keep on improving experimental throughput and data output of the experimental setup, as will be discussed in Section 11.3. In addition, further improvements in availability of well documented, open datasets may facilitate incorporation of datasets obtained by other work groups into work. A possibility of how this may come to pass will be discussed in Chapter 12.

Part III

Outlook

Chapter 11

Outlook and Future Experiments

Some findings in this study hinted at cellular mechanisms for which the here used experimental setup was insufficient. In the following, a discussion of improved and altered experiments will be presented. Further improvements to the setup will play a key role in future findings.
As was shown in Chapter 7, cells appear to be influenced by the fluid flow itself. Since the control data showed a clear decline in ruffling activity after exchanging the fluid, there appears to be an effect on the cell. How this may be assessed will be discussed in Section 11.1.
Section 11.2 focuses on how experiments may need to be modified in order to extend their duration without impacting cells by aging culture medium. Since findings in Section 7.2 showed the used delay times to be too short, longer experiments are required.
Possible improvements to the extraction and analysis of experimental data are presented in Section 11.3.

11.1 Impact of Medium Replacement on Cellular CDR Activity

Results in Section 7.1 indicated that cells are, in fact, influenced by the fluid flow upon replacement of the surrounding medium. During planning and testing of the setup, no influence on the cells was observed, which may hint at this effect being primarily visible due to the large amount of collected data. Without this many analyzed cells this behavior would have probably been left unnoticed.
In order to further investigate this, an approach would be collection of data for many cells without added growth factor for varying pressure settings of the perfusion system. A possible link between reduction in cell activity and flow rate could improve information on how the perfusion system affects cell behavior.

11.2 Further Extension of Delayed Repeated Stimulus Experiments

Since the investigated delay times for a second stimulation of 10 min to 40 min were proven to be insufficient in Section 7.2, further experiments with longer delay times are required.
One challenge for longer experiments is, since cells are enclosed in the flow chamber, that over longer periods of time the chemical conditions in the low volume of DMEM may deteriorate. Since DMEM uses a carbonate buffer to sustain a constant pH value, a lack of CO_2 within the channel, despite atmosphere in the incubator attached to the microscope being set to 5 % CO_2, may cause the pH value to shift.
A solution to this would be usage of different buffer solutions, such as HEPES. Experiments using HEPES buffer were performed, however cells appeared to be impaired by it. A negative effect of HEPES on cell culture is confirmed in literature by Bowman et al., 1985.
Another approach would be a more frequent replacement of the medium within the channel during the delay time. This however, as was already discussed in the previous section, does impact cells, too. A solution to this issue may be finding a low flow rate at which cells are not impacted and apply this frequently during the waiting period in order to replace the culture medium.
A change to the experimental setup and the timing of experimental steps would, however, require a re-run of the already obtained delay times in order to be able to properly analyze and compare the data.

11.3 Improved Automation of Data Extraction

The data extraction pipeline developed here automates many steps in the process, though some key steps still require manual intervention. Increasing the throughput of this pipeline may be a key to obtain more data, especially considering possible adaptations of the experimental protocol as discussed in Section 11.2.
Image segmentation using CNNs showed promising results and can be adapted to more steps in the pipeline. One example would be identification of occupied spots on the microcontact array, see Section 6.4.2. This step is currently performed manually, meaning an automation of this step reduces the total time needed to extract the data. Another example for beneficial use of modern machine learning approaches would be extraction of CDR data from circular kymographs, which is another key point requiring manual work for each cell.
Improvements to the already present segmentation of cells may be adding the ability to also label currently active CDRs on the cell, allowing for extraction of a timeline of geometrical dimensions for each CDR. This may, however be limited due to the used magnification of the microscope. A switch from a 10x magnification objective to 20x may be sufficient to properly analyze the morphology of CDR over time. This switch, however, would reduce the number of cells imaged per experiment due to the FOV being smaller.

Improving extraction of CDR data from kymographs may also be useful in more finegrained analysis of ruffle behavior during the process. Results obtained by Julia Lange, 2019, showed a dependency of CDR propagation velocity on membrane tension by analyzing data of simultaneously express CDRs on the same cell. These results showed a reduction in velocity upon formation of a second ruffle while another was already motile on the cell.
All these approaches involving neural networks would require improved computational hardware not currently available in the laboratory. Without, e.g. a sufficiently powerful GPU or other specialized hardware, the time required to train and test a neural network would heavily outweigh the gained benefits.

Chapter 12

The Relevance of Documented and Open Data Structures

A big challenge in science is availability of open datasets and well documented methodologies. The amount of data generated in order to produce publications greatly outweighs the data available with said publications. Open access to such data with ideally well documented accompanying metadata would greatly improve a very important aspect of science, namely the ability to reproduce published findings. Access to the original source data, not only the data extracted from it, would greatly improve this.
Another important aspect is the generally lacking availability of algorithm implementations for the analysis performed on data. In recent years, a push towards open source software improved the situation here, however heavily specialized or customized programs are typically not published in a way which enables verification of a proper implementation.
Ideally, data should be identifiable by a unique identification string and be immutable. A very promising proposed open standard for this are FAIR Digital Objects (FDOs). Where FAIR stands for **F**indability, **A**ccessibility, **I**nteroperability, and **R**euse of digital assets. The concept of digital objects is not new, virtually anyone involved in science has at some point used a Digital Object Identifier (DOI) link to reach the location of a searched publication. In fact, the bibliography of this thesis provides DOIs for the majority of cited sources. FDOs extend this approach by providing a framework for datasets with well documented metadata, see Section 12.1, datatype, schema and profile, as well as a permanent identifier similar to a DOI. Storage of such FDOs in openly accessible repositories greatly increases findability and reusability of existing data.
The approach of a well documented structure for all generated datasets as presented in Section A.2.1 of the appendix, aims at simplifying future use of the data generated during this study. Generally, usage of non-proprietary formats should be encouraged since such formats offer full access to all specifications, making reverse engineering unnecessary while also not depending on the mercy of a select few corporations or nation-states to keep supporting the format and ensure backwards compatibility in the case of intransparent updates to the format.

In addition to this, access to scientific data and publications generated thereof should not depend on the origin and financial means of any scientist or other individual.
The quote by Louis Pasteur from 1876 in the front matter of this thesis, repeated here, should always hold true — especially in times of again rising nationalism.

> *Science knows no country, because knowledge belongs to humanity, and is the torch which illuminates the world.*

12.1 Metadata

Data should always be accompanied by corresponding metadata. This metadata gives insight into how the data was collected, how the data format is laid out and a multitude of other possible information required to properly assess it's contents and relevance. Especially the layout of the data format used, which could be Comma Separated Values (CSV) for tabular data or binary formats for imaging data like in this work adds the ability for other researchers to investigate already present data without reverse engineering the data format and wasting precious resources like time and money in the process.

12.2 Evaluation Script Source Codes

With the ever increasing popularity of open source programs and programming languages in the sciences, publishing of the scripts used in evaluating the data comes at greatly reduced complexity.
With code versioning programs such as GIT and projects like GitLab or GitTea, it is possible to easily set up a server for publishing of source codes and providing the ability to quickly reproduce the code on local computers or other servers mirroring the code repositories.
Publication aspect aside, the ability to keep a proper version history of the code is immensely helpful in identification of introduced programming errors which may be uncovered. Trying different approaches at solving a given problem can be done without impacting the main working code by performing modifications easily in isolated branches. It is not without reason, that GIT became the most used versioning system in the programming world.

Part IV

Appendix

Appendix A

Used Software and Technology

This chapter of the appendix contains information about the general workflow using the software tools developed during this work. Since all of these programs are specialized tools, developed for certain tasks in the evaluation workflow, a short explanation of the underlying principles of each tool is given. Additionally, in A.2.1, page 105, an overview and short documentation of the internal structure used for data storage is given to facilitate possible future use of the generated data.

Image Processing Utilities A.1

A number of specialized Command Line Interface (CLI) and Graphical User Interface (GUI) software tools was developed during this project. All of these programs are specialized for certain tasks, based on the data generated with the used experimental setup. The sections hereafter give a short overview of the respective functions.

Imaging File Conversion and Microcontact Grid Fitting A.1.1

In order to facilitate faster processing of the data, files from the microscope's control software AxioVision in Zeiss Vision Image (ZVI) format needed to be converted to a more widely readable file format. Since the recorded images are a monochromatic time series of two dimensional pixel images, the simplest way of storage was three dimensional arrays (x, y, t). The variables x and y correspond to image dimensions in pixels and the time dimension t iterates over all frames recorded in the time series.
One possible file storage method would be saving the images as TIFF image stacks, however here the Hierarchical Data Format 5 (HDF5) image format was chosen. Due to the possibility of storing metadata information along with the data, as well as being able to store each processing step's results in the same file this file format was deemed appropriate for the intended use case. A significant advantage of the approach followed here is the ability to store all data belonging to a single experiment in the same file.

Conversion from ZVI files to a format compatible with software tools used for processing the images and data was performed with a specialized CLI tool written in the `Julia` programming language. After conversion of the images to HDF5 format, the process of fitting the microcontact grid as described in 6.4.2 is performed and results are thereafter saved into the same file.
In order to maximize the signal obtained by the Radon transform and the two dimensional convolution, several preparatory steps were required. Reduction of overall variance in pixel brightness values was achieved by background subtraction and execution of the Canny edge detection algorithm on the image (Canny, 1986; Xuan and Hong, 2017). The output binary image was then further process by filtering small objects using morphological operations. This reduced the influence of debris and unoccupied FN substrates in the image, hence augmenting the following processing steps.
For improved results of the image registration algorithm, the filtered image was augmented by an additional step of calculating the convolution as described in Equation (6.9) of the filtered image with a generated image of a disk with the size of a FN substrate. This step resulted in a more stable output function and more accurate identification of the shifting offset.

A.1.2 Cell Cropping

Cell cropping was performed using a GUI tool written in Python programming language. This tool loads images from HDF5 files and overlays the registered microcontact grid annotated with cell indexes. A selection box can then be used to select the adhesion spots occupied with circular cells for automatic cropping and storing of cells. Since each experiment comprises multiple FOVs, it is possible to process each FOV individually with few mouse clicks.
After selecting the desired cells and clicking the `Crop` button, the center point of each marked cell is taken and a square containing it, the ROI, is cropped out and saved as a new image stack with a consecutive index, annotated with metadata to enable tracing of it's origin.
In the case of a misaligned automatic microcontact grid fit[1], an additional manual cropping function was included. Using this method, a square selection around the position of the mouse cursor when clicked is cropped.

A.1.3 Circular Kymograph Generation

Generation of circular kymographs is performed using a GUI tool which cycles through available cropped cells in the dataset. Upon opening a file, the tool shows the first cell within the dataset and assumes the cell center to be at the image center. Since cells are not always centered in the ROI, it is possible to manually shift the center point C by clicking onto the cell center.
With the desired kymograph center point C selected it is then possible to set the kymograph's radius and a width for averaging, both in radius r and angle φ, modifying them to $r \pm \Delta r$ and

[1] Misalignment of the fit is often the case when only few microcontacts are populated by cells or when cells detach from the microcontact and subsequently drift across the flow channel before being flushed out in a queued medium exchange. A manual crop is in these cases more efficient than reprocessing the full image stack with modified settings.

$\varphi \pm \Delta\varphi$. The width setting allows multiple pixels perpendicular to the kymograph circle over a larger angle to be averaged, see Figure A.1. By reading the mean gray intensity value of pixels within the area, the overall influence of sensor read noise within the picture is reduced. The algorithm used here is inspired by the work of Erik Bernitt, who introduced the method and concept of circular kymographs into the work group.

The general process of extracting the circular kymograph is hereafter described. All operations are done in polar coordinates, with the center of the circle set as selected in the GUI. For a point A at angle $\varphi \in [0, 2\pi)$ and radius r, set via the GUI, all pixels touched or overlaid by the area spanned by $(r \pm \Delta r, \varphi \pm \Delta\varphi)$ indicated in Figure A.1 are being averaged. This process is repeated

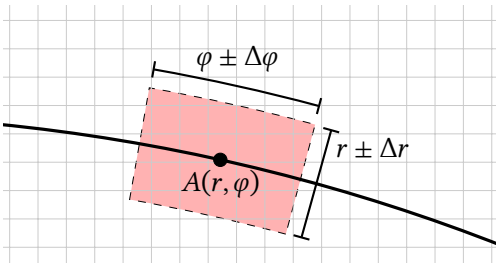

Figure A.1: Indication of point $A = (r, \varphi)$ as part of the circular kymograph with the area $(r \pm \Delta r, \varphi \pm \Delta\varphi)$ shaded in red indicating the area which is being averaged in order to reduce the influence of camera sensor noise. The thick black line indicates the circle used for generating the kymograph. Light gray squares indicate image pixels. Pixels overlaid or touched by the light-red area are used in the averaging process.

for all frames of the digital image stack, thus yielding a brightness value b_φ for all timesteps t_i resulting in a vector with n_{Frames} entries. Since this process is repeated for all values of φ, the results can be represented as a two dimensional image, the so-called kymograph with time t on the abscissa and angle φ on the ordinate. An example for a full kymograph as displayed in Figure A.2, section A.1.4. CDRs are then clearly visible as dark structures, such as lines or dots. The visible structure depends on propagation velocity and lifetime, of course.

A.1.4 CDR Data Extraction from Kymographs

Identification of CDRs within the kymographs was performed by marking CDR traces in the kymograph manually. The GUI used for this task shows the image of cell along with it's kymograph for better assessment of whether the visible trace is a CDR or an imaging artifact. Attempts to automate this process were made, however no method able to robustly identify the CDRs was found. With more computational power and well trained deep learning models an automated extraction of data may be viable, however due restrictions of available hardware[2] this path was not followed.

[2]Deep learning CNNs are very demanding in terms of computational hardware. Especially a general purpose graphical processing unit in the computer can, if available, greatly enhance performance. Since such hardware was not available for this work, manual data extraction was deemed more efficient than CNN calculations potentially lasting full weeks per training process.

The manual marking process then involves identifying start- and endpoints of CDR traces, like

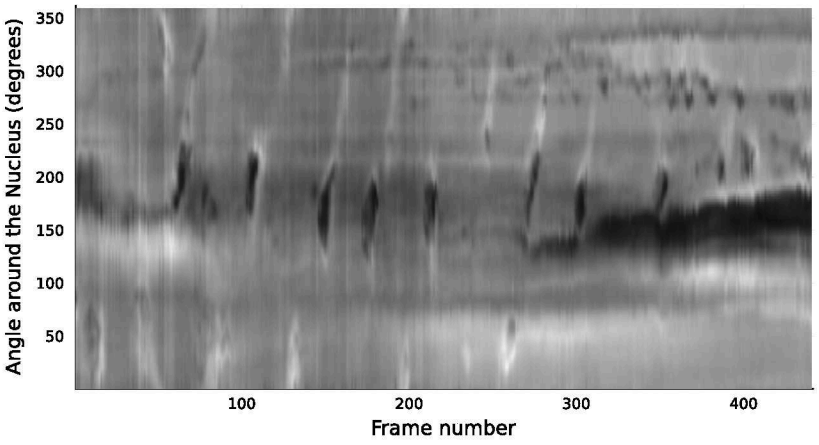

Figure A.2: Example plot of a circular kymograph obtained with the process layed out in Section A.1.3. CDRs are visible as dark traces with varying lengths and slopes in the kymograph. Part of the kymograph darkening after frame 270 indicates changes in cell morphology, in this case a shift of nucleus location on the printed microcontact. This example of an imperfect kymograph was deliberately chosen here to also emphasize on issues with automating analysis thereof.

those visible in Figure A.2 and clicking on them, leaving a visual dashed line in the GUI and an entry with the collected data in a table view. Upon finishing marking CDRs in all previously cropped cells, data can be saved and be read out of the storage file for further processing and analysis.
This data enables measurement of CDR lifetime, propagation velocity and distance traveled. Additionally from the collected dataset per cell, the cell's activity can be measured, as well as potential locations of high CDR activity on the lamellipodium.

A.1.5 Further Processing

Processing of extracted CDR data is then performed via a collection of data analytics scripts written in Julia or Python programming language.
The paradigm of being able to identify which cell and experiment each CDR originated from was upheld during all statistical processing. In order to achieve this identification, each CDR and cell were given a unique identification number and a database was upheld for looking up which CDR belongs to which cell, as well as their respective source experiment files.

A.2 Data Storage File Documentation

Experimental data obtained from microscopy is converted from proprietary ZVI files to HDF5 format. This file format provides an internal structure similar to a file directory and enables easy

loss less compression of the embedded data[3]. Additionally, the HDF5 format has bindings for all programming languages used in this work, making it possible to seamlessly switch between programming languages depending on the context and the language's respective strengths. The HDF5 format is widely used in science, most prominently in numerical simulations, but also in various other scientific fields accumulating large amounts of data (Folk et al., 2011).
This conversion enables storage of the entire experiment with image stacks from multiple positions, along with image processing results in the same file. Additionally, it allows for seamless processing of the data using tools written in different programming languages. Another valuable property of the HDF5 format is the possibility to add so-called attributes to stored datasets, which is here used to add metadata to every stored dataset.

Data Storage Layout A.2.1

Storing data in HDF5 files enables, among many other options, a file-directory like internal structure, which simplifies retrieval of only desired datasets from a large file. Datasets are stored in files using filenames of the pattern

```
YYYY_MM_DD_N_drug_concentration_contactsize_flow.h5
```

where `N` is the index of the experiment for the given day and `flow` (or `noflow`) being an indication if the perfusion system was in use. The internal file layout is hereafter summarized in a tree view in Figure A.3, page 106.

Each cropped cell can be backtraced to the corresponding origin coordinates in the full image stack via information stored as metadata attributes. Attributes also contain information about pixel and time scaling factors. Processing of CDR data is then done by collecting necessary information from the HDF5 files.
For every CDR in the final processing dataset it is thus possible to look up the originating cell and uncropped image whenever necessary. This approach to storing the data has been chosen in order to enable reuse of the data for future projects. Having all necessary informations stored alongside the actual data in the same files enables easier interpretation of the dataset.

Additional Software Used A.3

Various different software applications aside from the aforementioned self-developed solutions were used. The most important ones are listed in this section for transparency reasons.
Spreadsheets were managed using the open-source *LibreOffice Calc* application.
Writing of this thesis was performed using the *neovim* text editor and LaTeXtypesetting engine using the open source Libertinus fonts family.

[3] Due to the imaging data generated consisting of large amounts of background, i.e. non-cell parts of the image, the compression algorithms significantly reduce file sizes. This results in faster file transfers and overall faster processing, when computer hard drives are throttling the computation.

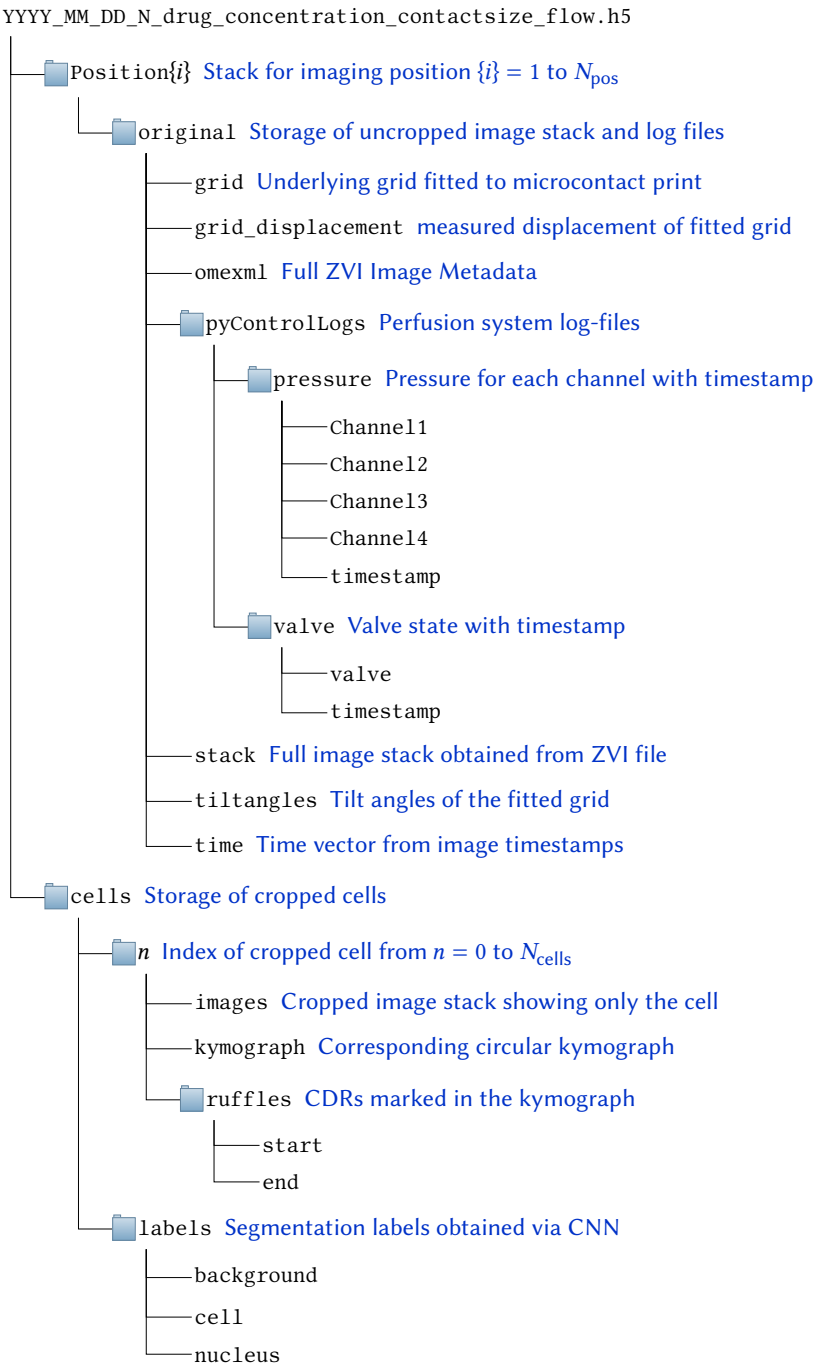

Figure A.3: Tree view of used internal HDF5 file structure. Directory icons denote HDF5 groups, entries without icon are datasets which can be read into processing software as array structure.

Version controlling of self developed software and thesis text-files was performed using the program `git`.
Bibliography management was done using `Zotero`.
Sketches and figures have been generated using the *Inkscape* vector-graphics editor, the TikZ package for LaTeX. In the case of data plots, figures were generated using plotting libraries `Plots.jl` for `Julia` programming language and `matplotlib` for `Python` programming language. Programming languages used for the different plots were chosen based on the individual requirements and ease of use, as well as maturity of the underlying libraries for the desired figures. Since all data is stored in formats which can easily be used by both languages this was easily achieved and streamlined processing of data.
The majority of programs used was free and open source software, in order to rely as little as possible on closed source software and to ensure the possibility of inspecting the implementations of algorithms for data evaluation.

A.3.1 Data Processing and Evaluation

Evaluation of data and generation of plots was performed using `Python` and `Julia` programming languages.

Notable Julia Packages

A set of notable `Julia` packages used here is displayed in the following with credit to their authors where possible. Versions have been consistently kept up to date.

- DataFrames
- Plots
- StatsPlots
- DrWatson
- Statistics
- MultivariateStats
- hdf5

Notable Python Modules

A set of notable `Python` packages used here is displayed in the following with credit to their authors where possible. All package versions have been consistently kept up to date.

- Numpy (Harris et al., 2020)

- Matplotlib (Hunter, 2007)
- pyqt
- sklean
- tensorflow
- keras
- pandas

A.3.2 Microscopy Image Acquisition, Image Review and Experiment Control

Microscopy was performed using Zeiss `Axiovision` Software by Carl Zeiss Microscopy.
Quick review and quality assessment of the obtained data before further processing was done in `AxioVision` and `ImageJ` software. After this initial review, data may be deemed to be of low quality due to, e.g. cells drifting out of the focal plane or too many cells detaching from microcontacts.
Control of the perfusion system consisting of the *p2cs* by biophysical tools and a motorized valve was performed using a custom written Python program called `pyControl`. A database of performed experiments with annotations and details was kept using LibreOffice `Calc` software.

Appendix B

Laboratory Protocols

Cell Splitting B.1

The general process of sustaining cell culture by splitting the cells at 70 % confluency can be summarized as follows:

1. Warm up all required media to 37 °C in a heatbath
2. removal of culture medium and washing with Phosphate Buffered Saline (PBS)
3. Remove PBS, add trypsin and place in incubator for 2 minutes, check if cells are detached under the microscope. If cells remain adherent, increase incubation time
4. add 2 mL of DMEM to inactivate the trypsin
5. Transfer fluid containing the cells into a 10 mL falcon tube
6. Centrifuge at 3600 rpm for 3 minutes
7. Aspirate off the fluid, while avoiding the cell pellet at the bottom of the tube
8. Add 2 mL of DMEM and gently resuspend the cells by slowly pumping the fluid up and down in a 1 mL pipette
9. Transfer a drop of the cell suspension onto a hemocytometer in order to determine cell concentration
10. Prepare new culture flask by adding 5 mL of DMEM
11. Add the required amount of suspended cells to obtain desired confluency

B.2 Cell Preparation for Experiments

In advance to planned experiments, cells from the surplus after spltting were plated into [5 cm PETRI DISHES!?] at varying confluencies, depending on the designated day of use.

- Cells to be used 1 day after splitting the cells: $9 \cdot 10^4$
- Cells to be used 2 days after splitting the cells: $6 \cdot 10^4$

General handling of the cells for experiments is highly similar to the process of cell splitting shown in Section B.1. The main deviation from this process is that after resuspending the cell pellet at step 10, cells are not plated into a culture flask, but into the flow channels of the flow chamber prepared with microcontact printing, see Section B.3.
Cells within the flow channel are then returned to the incubator for 30 min in order to let the cells spread onto the FN microcontacts. After the incubation period, proper cell spreading is assessed under the microscope and if deemed viable, unattached cells are removed by flushing the flow channel with DMEM twice. This flushing is performed by steadily adding 1 mL of DMEM to one channel connector while simultaneously aspirating the old medium off the opposite channel connector. The flow generated by this method is sufficient to remove unattached cells from the channel without detaching the cells occupying microcontacts.
The cells are then ready for use and the flow chamber is connected to the perfusion system within the microscopes incubator. During the process of connecting the tubing it is paramount to not incorporate any air bubbles into the flow system.[1]

B.3 Microcontact Printing

Microcontact printing was performed following the protocol by Théry and Piel (2009) with minor modifications. These modifications were partially required to enable the use of microcontacts within flow channels. Additionally, some adsorption times were reduced after ensuring equal quality of the produced microcontacts.

Required Materials

- FN
- PLL-g-PEG
- Tweezers
- PBS
- PDMS stamp

[1] Such air bubbles greatly impair the performance of the perfusion system due to greatly increased flow resistance. Additionally, flushing air over the cells will in most cases damage them.

- reservoir with MilliQ water
- glass slide
- Argon-Plasma Pen
- ibidi Sticky Slide
- Ultrasonic cleaning bath heated to 60 °C

Microcontact Printing Process

1. Resuspend the FN solution by pipetting it up and down 5 times, let it rest for 2 minutes
2. Spread 20 µL of the FN solution on the PDMS stamp, gently spreading the drop across the surface using the pipette tip without touching the stamp's surface, let it adsorb for 15 minutes
3. During the 15 minutes waiting time, prepare the glass slide by marking the location of ibidi sticky slide's flow channels using a pen
4. 5 Minutes before the end of the 15 minute time span: activate the glass sides unmarked surface using the Argon-Plasma pen, by slowly moving the plasma-jet across the glass surface
5. Aspirate the unadsorbed FN solution off the stamp and leave the stamp in the clean cabinet for 2 minutes to dry off any remaining liquid.
6. Grasp the PDMS stamp with tweezers, invert it so that the FN coated surface faces downwards and carefully place the stamp onto the activated glass surface at the center of a marked flow channel, lateral movement on the glass surface must be avoided. Leave for 2 minutes.
7. Carefully grasp the stamp again with tweezers and remove it from the glass surface in a straight upwards movement[2] — a light adhesion to the glass surface is typically a sign of well printed microcontacts. In order to clean the stamp, transfer it into a reservoir filled with MilliQ water.
8. Combine the glass slide and the sticky slide, so that the printed microcontacts are placed inside of the individual flow channels.
9. Add 40 µL PLL-g-PEG to the flow channel, leave for adsorption for 15 minutes.

[2]Moving the stamp laterally on the glass substrate during this process results in imperfect FN patches. In case this happens, it is typically advisable to restart the process. Some FN patches may have the desired shape and dimensions, but the vast majority will be smeared out into different shapes.

10. Remove the PLL-g-PEG solution by aspiration it off and replace it with 100 µL PBS for removal of unadsorbed PLL-g-PEG. Leave for 10 minutes
11. Repeat the washing process again leaving the PBS for 2 minutes.
12. Repeat the washing process and leave the PBS inside of the flow channel.
13. The microcontacts are ready to be used and can be stored sealed with parafilm at 4 °C for up to 2 days.

Cleaning of Used Stamps for Next Usage

1. Place the container holding the stamps in MilliQ water into the ultrasonic cleaning bath and wash the stamps for 15 minutes at 60 °C.
2. Remove the MilliQ water, add an equal amount of 98 % Ethanol and repeat the ultrasonic cleaning for 15 minutes at 60 °C.
3. Remove the stamps from the Ethanol, and carefully place them into their storage containers with the stamp-surface showing upwards, let the stamps dry in a heating cabinet at 50 °C for at least 5 hours.
4. Remove the dried stamps from the heating cabinet and store them at room temperature. The stamps are now ready to be reused.

B.4 Preparation of hPDGF Stock Solution

hPDGF-BB stock solutions were prepared from lyophilized form following the protocol provided by manufacturer *Cell Signaling Technology*.

Appendix C

Supplementary Figures

Supplementary figures for some sections in the results part are displayed in the following sections. This includes measured cell activity after stimulation for varying delay times in Section C.1.
Elbow and Silhouette plots used for determination of the number of clusters in Chapters 8 and 9 are presented in Section C.2.

C.1 Cell Activity after the Secondary Stimulus

This section contains the remaining figures of Section 7.2 in the results part in order to reduce visual clutter in the results part.
Figure C.1 shows the data for the control set without added hPDGF. The Figure for 10 ng/mL was already visible in Section 7.2. Data for 21 ng/mL is presented in Figure C.2, followed by Figure C.3 for the 30 ng/mL dataset.
As mentioned in the results part, there appears to be no clear dependency of activity on delay time pointing towards delay times being chosen too short.

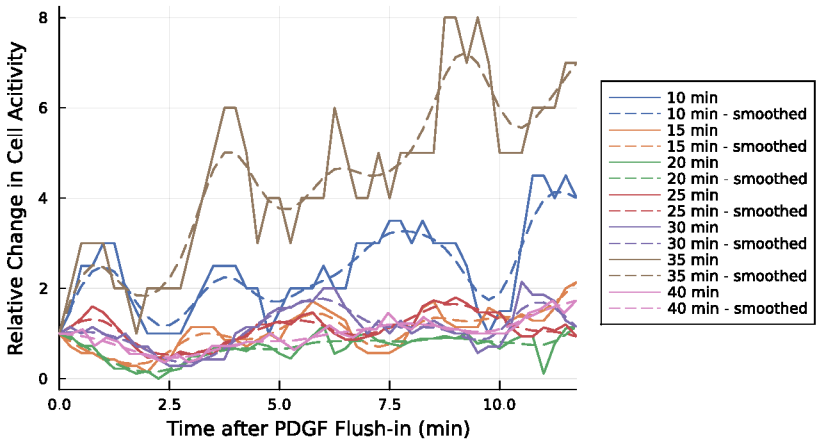

Figure C.1: Change in cell activity relative to the value at $t = 0$ min for the second stimulus with no added hPDGF, discriminated by delay time. The decrease in activity at 2 min is clearly visible. Interestingly, the brown line for 35 min initially increases at a higher rate than the remaining lines and shows an earlier decline in activity.

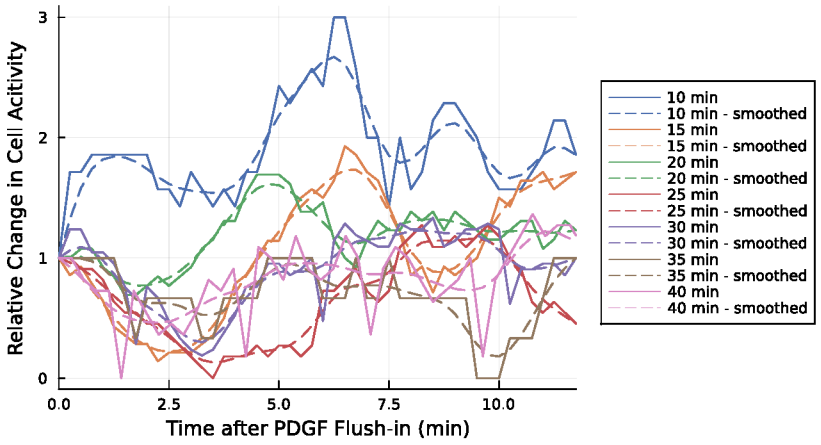

Figure C.2: Change in cell activity relative to the value at $t = 0$ min for the second stimulus with 21 ng/mL added hPDGF, discriminated by delay time. The decline here is again visible, however shifted to a later time. This shift, however, does not appear to have any dependency on the delay time before the stimulus. The blue line indicating a delay of 10 min here appears to be an outlier.

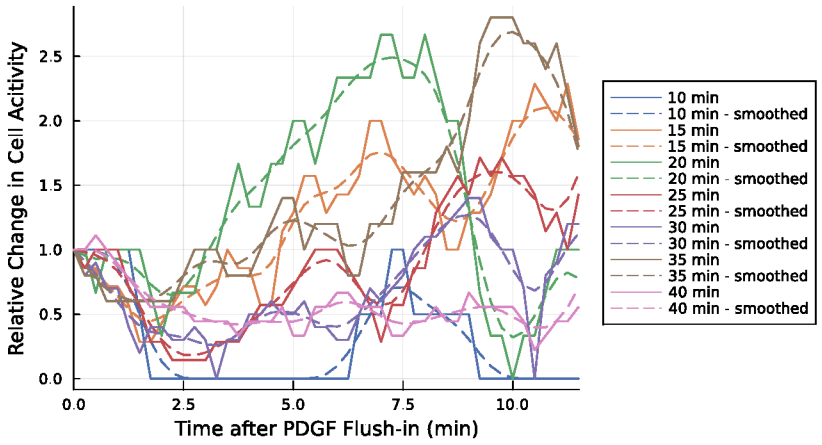

Figure C.3: Change in cell activity relative to the value at $t = 0$ min for the second stimulus with 30 ng/mL added hPDGF, discriminated by delay time. Here, again the minimum appears to be shifted to later times without a clear dependency on delay times. In comparison to Figure C.2, the 10 min delay drops to a minimum, while the green line representing 20 min increases.

Elbow and Silhouette Plots C.2

Here, the elbow and silhouette plots, see Section 6.6.4, used for determination of the number of clusters to be discriminated by the k-means algorithm are presented. As was described when these scores were introduced, these measurements remove arbitrariness from selection of the number of clusters.

Determination of CDR Clusters C.2.1

For data presented in Section 8.1.2, the numer of clusters to be identified using k-means clustering was determined to be 4. Figure C.4 shows the plotted elbow plot for k-means cost and silhouette score. The local maximum of silhouette score at $k = 4$ indicates the chosen amount of clusters.

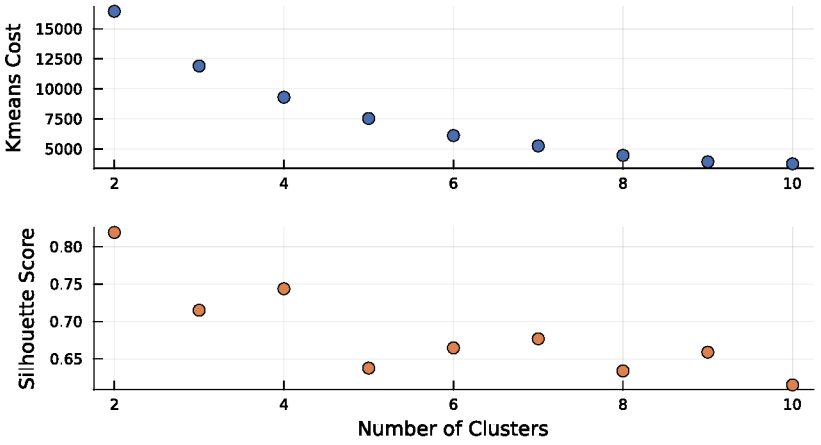

Figure C.4: Elbow plot of k-means cost function and silhouette scores used for determining the number of clusters to be identified within the CDR dataset. The local maximum in silhouette score at $k = 4$ indicates the number used in the analysis.

C.2.2 Determination of Cell Clusters

The number of clusters used in the analysis of cell states in Chapter 9 was determined using Figure C.5. Here, the maximum of the silhouette score at $k = 3$ indicates the number of clusters to be identified. Note that a fourth cluster, cluster 0, was automatically added in order to contain inactive cells.

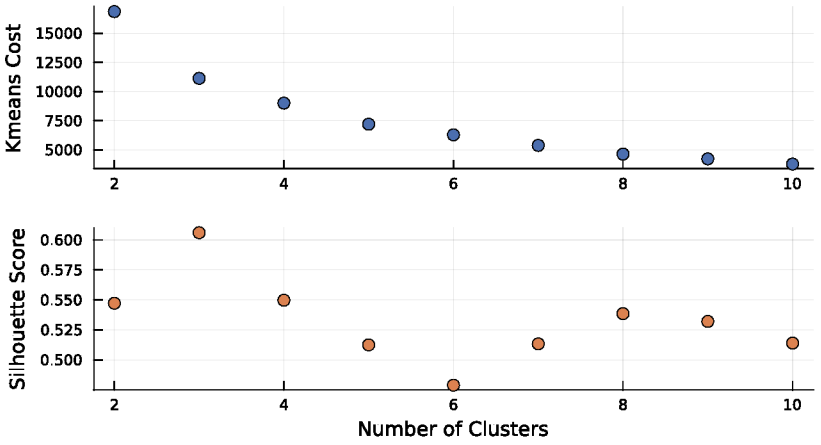

Figure C.5: Plot of k-means cost and silhouette score for determination of the number of cell clusters to be identified within the dataset presented in Chapter 9. The local maximum at $k = 3$ for the silhouette score and the corresponding "elbow" in the k-means cost indicates the used number of clusters for the k-means algorithm.

Bibliography

Aggarwal, Charu C. (2018). *Neural Networks and Deep Learning: A Textbook*. en. Cham: Springer International Publishing. ISBN: 978-3-319-94462-3 978-3-319-94463-0. DOI: 10.1007/978-3-319-94463-0.

Alberts, Bruce et al. (2015). *Molecular Biology of the Cell*. 6th ed. Garland Science. ISBN: 978-0-8153-4432-2.

Allard, Jun and Alex Mogilner (2013). "Traveling waves in actin dynamics and cell motility". In: 25. DOI: 10.1016/j.ceb.2012.08.012.

Allen, RD, GB David, and G Nomarski (1969). "The Zeiss-Nomarski differential interference equipment for transmitted-light microscopy". In: *Zeitschrift fur Wissenschaftliche Mikroskopie und Mikroskopische Technik* 69.4, pp. 193–221.

Antoniades, H N (Dec. 1981). "Human platelet-derived growth factor (PDGF): purification of PDGF-I and PDGF-II and separation of their reduced subunits." In: *Proc. Natl. Acad. Sci. U. S. A.* 78.12, pp. 7314–7. ISSN: 0027-8424.

Avila, Kerstin et al. (July 2011). "The Onset of Turbulence in Pipe Flow". In: *Science* 333.6039. Publisher: American Association for the Advancement of Science, pp. 192–196. DOI: 10.1126/science.1203223.

Bacabac, Rommel G et al. (Jan. 2005). "Dynamic shear stress in parallel-plate flow chambers." English. In: *J. Biomech.* 38.1, pp. 159–67. ISSN: 0021-9290. DOI: 10.1016/j.jbiomech.2004.03.020.

Balla, Tamas (July 2013). "Phosphoinositides: Tiny Lipids With Giant Impact on Cell Regulation". In: *Physiological Reviews* 93.3. Publisher: American Physiological Society, pp. 1019–1137. ISSN: 0031-9333. DOI: 10.1152/physrev.00028.2012.

Beebe, David J, Glennys A Mensing, and Glenn M Walker (Jan. 2002). "Physics and applications of microfluidics in biology." In: *Annu. Rev. Biomed. Eng.* 4, pp. 261–286. ISSN: 1523-9829.

Bernitt, Erik (2015). "The Dynamics of Dorsal Actin Waves". PhD Thesis. Universität Bremen.

Bernitt, Erik and Hans Günther Döbereiner (2017). "Spatiotemporal Patterns of Noise-Driven Confined Actin Waves in Living Cells". In: *Phys. Rev. Lett.* 118.4. ISSN: 10797114. DOI: 10.1103/PhysRevLett.118.048102.

Bernitt, Erik, Hans Günther Döbereiner, et al. (2017). "Fronts and waves of actin polymerization in a bistability-based mechanism of circular dorsal ruffles". In: *Nat. Commun.* 8. ISSN: 20411723. DOI: 10.1038/ncomms15863.

Bernitt, Erik, Cheng Gee Koh, et al. (Jan. 2015). "Dynamics of actin waves on patterned substrates: A quantitative analysis of circular dorsal ruffles". In: *PLoS One* 10.1, e0115857. ISSN: 19326203. DOI: 10.1371/journal.pone.0115857.

Blanchoin, Laurent et al. (Jan. 2014). "Actin Dynamics, Architecture, and Mechanics in Cell Motility". In: *Physiological Reviews* 94.1. Publisher: American Physiological Society, pp. 235–263. ISSN: 0031-9333. DOI: 10.1152/physrev.00018.2013.

Bloomfield, Gareth and Robert R. Kay (2016). "Uses and abuses of macropinocytosis." In: *J. Cell Sci.* 129.14, pp. 2697–705. ISSN: 1477-9137. DOI: 10.1242/jcs.176149.

Boguski, Mark S. and Frank McCormick (Dec. 1993). "Proteins regulating Ras and its relatives". en. In: *Nature* 366.6456. Number: 6456 Publisher: Nature Publishing Group, pp. 643–654. ISSN: 1476-4687. DOI: 10.1038/366643a0.

Borisy, Gary G. and Tatyana M. Svitkina (2000). "Actin machinery: Pushing the envelope". In: *Curr. Opin. Cell Biol.* 12.1, pp. 104–112. ISSN: 09550674. DOI: 10.1016/S0955-0674(99)00063-0.

Bovik, Alan C. (2009). *The Essential Guide to Image Processing*. en. Elsevier. ISBN: 978-0-12-374457-9. DOI: 10.1016/B978-0-12-374457-9.X0001-7.

Bowman, C. Michael et al. (1985). "Hepes may stimulate cultured endothelial cells to make growth-retarding oxygen metabolites". In: *Vitr. Cell. Dev. Biol.* 21.3, pp. 140–142. ISSN: 10545476. DOI: 10.1007/BF02621350.

Bronstein, Ilja et al. (2008). *Taschenbuch der Mathematik*. 7th ed. Harri Deutsch. ISBN: 3-8171-2005-2.

Bruus, Henrik (2008). *Theoretical microfluidics*. 1st ed. Vol. 18. 33235. Oxford University Press. ISBN: 0-19-923509-0. DOI: 10.1111/j.1574-6968.2009.01808.x.

Buccione, Roberto, James D Orth, and Mark a McNiven (Aug. 2004). "Foot and mouth: podosomes, invadopodia and circular dorsal ruffles." In: *Nat. Rev. Mol. Cell Biol.* 5.8, pp. 647–657. ISSN: 1471-0072. DOI: 10.1038/nrm1436.

Canny, J. (Nov. 1986). "A Computational Approach to Edge Detection". In: *IEEE Transactions on Pattern Analysis and Machine Intelligence* PAMI-8.6. Conference Name: IEEE Transactions on Pattern Analysis and Machine Intelligence, pp. 679–698. ISSN: 1939-3539. DOI: 10.1109/TPAMI.1986.4767851.

Carlier, Marie-France and Dominique Pantaloni (June 1997). "Control of actin dynamics in cell motility11Edited by N.-H. Chua". en. In: *Journal of Molecular Biology* 269.4, pp. 459–467. ISSN: 0022-2836. DOI: 10.1006/jmbi.1997.1062.

Chesarone, Melissa A and Bruce L Goode (Feb. 2009). "Actin nucleation and elongation factors: mechanisms and interplay". en. In: *Current Opinion in Cell Biology*. Cell structure and dynamics 21.1, pp. 28–37. ISSN: 0955-0674. DOI: 10.1016/j.ceb.2008.12.001.

Dam, Teunis J.P. van, Johannes Bos, and Berend Snel (Jan. 2011). “Evolution of the Ras-like small GTPases and their regulators”. In: *Small GTPases* 2.1. Publisher: Taylor & Francis _eprint: https://doi.org/10.4161/sgtp.2.1.15113, pp. 4–16. ISSN: 2154-1248. DOI: 10.4161/sgtp.2.1.15113.

Demtröder, Wolfgang (2008). *Experimentalphysik 1*. Springer-Lehrbuch. Berlin, Heidelberg: Springer Berlin Heidelberg. ISBN: 978-3-642-25465-9. DOI: 10.1007/978-3-642-25466-6.

Di Paolo, Gilbert and Pietro De Camilli (Oct. 2006). “Phosphoinositides in cell regulation and membrane dynamics”. en. In: *Nature* 443.7112. Number: 7112 Publisher: Nature Publishing Group, pp. 651–657. ISSN: 1476-4687. DOI: 10.1038/nature05185.

Egami, Youhei et al. (2014). *Small GTPases and phosphoinositides in the regulatory mechanisms of macropinosome formation and maturation: Gtpases and phosphoinositides in macropinocytosis*. Vol. 5. SEP. ISBN: 1664-042X (Electronic)$\backslash$r1664-042X (Linking). DOI: 10.3389/fphys.2014.00374.

Einstein, A. (1905). “Über die von der molekularkinetischen Theorie der Wärme geforderte Bewegung von in ruhenden Flüssigkeiten suspendierten Teilchen”. In: *Ann. Phys.* 322.8, pp. 549–560. ISSN: 1521-3889. DOI: 10.1002/andp.19053220806.

FitzHugh, Richard (July 1961). “Impulses and Physiological States in Theoretical Models of Nerve Membrane”. en. In: *Biophysical Journal* 1.6, pp. 445–466. ISSN: 0006-3495. DOI: 10.1016/S0006-3495(61)86902-6.

Folk, Mike et al. (Mar. 2011). “An overview of the HDF5 technology suite and its applications”. In: *Proceedings of the EDBT/ICDT 2011 Workshop on Array Databases*. AD ’11. New York, NY, USA: Association for Computing Machinery, pp. 36–47. ISBN: 978-1-4503-0614-0. DOI: 10.1145/1966895.1966900.

Gerhardt, Matthias et al. (Oct. 2014). “Actin and PIP3 waves in giant cells reveal the inherent length scale of an excited state”. en. In: *J Cell Sci* 127.20, pp. 4507–4517. ISSN: 0021-9533, 1477-9137. DOI: 10/f6qbm4.

Gerisch, Günther et al. (2009). “Self-organizing actin waves as planar phagocytic cup structures”. In: *Cell Adhesion & Migration* 3.4, pp. 373–382. ISSN: 1933-6918.

Hannink, Mark and Daniel J. Donoghue (July 1989). “Structure and function of platelet-derived growth factor (PDGF) and related proteins”. In: *Biochim. Biophys. Acta - Rev. Cancer* 989.1, pp. 1–10. ISSN: 0304419X. DOI: 10.1016/0304-419X(89)90031-0.

Harris, Charles R. et al. (Sept. 2020). “Array programming with NumPy”. en. In: *Nature* 585.7825. Number: 7825 Publisher: Nature Publishing Group, pp. 357–362. ISSN: 1476-4687. DOI: 10.1038/s41586-020-2649-2.

Higgs, Henry N. and Thomas D. Pollard (Nov. 1999). “Regulation of Actin Polymerization by Arp2/3 Complex and WASp/Scar Proteins *”. English. In: *Journal of Biological Chemistry* 274.46. Publisher: Elsevier, pp. 32531–32534. ISSN: 0021-9258, 1083-351X. DOI: 10.1074/jbc.274.46.32531.

Hoon, J.-L., W.-K. Wong, and C.-G. Koh (Aug. 2012). "Functions and Regulation of Circular Dorsal Ruffles". In: *Mol. Cell. Biol.* 32.21, pp. 4246–4257. ISSN: 0270-7306. DOI: 10.1128/MCB.00551-12.

Hua, Rui et al. (2023). "Identification of circular dorsal ruffles as signal platforms for the AKT pathway in glomerular podocytes". en. In: *Journal of Cellular Physiology* n/a.n/a. ISSN: 1097-4652. DOI: 10.1002/jcp.30996.

Hunter, John D. (2007). "Matplotlib: A 2D graphics environment". In: *Comput. Sci. Eng.* 9.3, pp. 99–104. ISSN: 15219615. DOI: 10.1109/MCSE.2007.55.

Inagaki, Naoyuki and Hiroko Katsuno (2017). "Actin Waves: Origin of Cell Polarization and Migration?" In: *Trends Cell Biol.* 27.7, pp. 515–526. ISSN: 18793088. DOI: 10.1016/j.tcb.2017.02.003.

Jolliffe, Ian T. and Jorge Cadima (Apr. 2016). "Principal component analysis: a review and recent developments". In: *Philosophical Transactions of the Royal Society A: Mathematical, Physical and Engineering Sciences* 374.2065. Publisher: Royal Society, p. 20150202. DOI: 10.1098/rsta.2015.0202.

Kabsch, W. and J. Vandekerckhove (1992). "Structure and function of actin". eng. In: *Annual Review of Biophysics and Biomolecular Structure* 21, pp. 49–76. ISSN: 1056-8700. DOI: 10.1146/annurev.bb.21.060192.000405.

Kay, Robert R, Thomas D Williams, and Peggy Paschke (2018). "Amplification of PIP3 signalling by macropinocytic cups." In: *Biochem. J.* 475.3, pp. 643–648. ISSN: 1470-8728. DOI: 10.1042/BCJ20170785.

Kerr, Markus C. and Rohan D. Teasdale (2009). "Defining macropinocytosis". In: *Traffic* 10.4, pp. 364–371. ISSN: 13989219. DOI: 10.1111/j.1600-0854.2009.00878.x.

King, Jason S. and Robert R. Kay (Feb. 2019). "The origins and evolution of macropinocytosis". English. In: *Philosophical Transactions of the Royal Society B-Biological Sciences* 374.1765. Place: London Publisher: Royal Soc WOS:000459332600010, p. 20180158. ISSN: 0962-8436. DOI: 10.1098/rstb.2018.0158.

Koestler, Stefan A. et al. (Mar. 2009). "F- and G-Actin Concentrations in Lamellipodia of Moving Cells". en. In: *PLOS ONE* 4.3. Publisher: Public Library of Science, e4810. ISSN: 1932-6203. DOI: 10.1371/journal.pone.0004810.

Kulkarni, G V and C a McCulloch (1994). "Serum deprivation induces apoptotic cell death in a subset of Balb/c 3T3 fibroblasts." In: *J. Cell Sci.* 107 (Pt 5, pp. 1169–1179. ISSN: 0021-9533.

Lange, Julia (2019). "Mechanobiological control of circular dorsal ruffle dynamics". PhD Thesis. Bremen.

Legg, J. A. et al. (Nov. 2006). "N-WASP Involvement in Dorsal Ruffle Formation in Mouse Embryonic Fibroblasts". In: *Molecular Biology of the Cell* 18.2, pp. 678–687. ISSN: 1059-1524. DOI: 10.1091/mbc.E06-06-0569.

Lu, Hang et al. (2004). "Microfluidic shear devices for quantitative analysis of cell adhesion". In: *Anal. Chem.* 76.18, pp. 5257–5264. DOI: 10.1021/ac049837t.

Lyashenko, Eugenia et al. (2020). "Receptor-based mechanism of relative sensing and cell memory in mammalian signaling networks". In: *eLife* 9, e50342. ISSN: 2050-084X. DOI: 10.7554/eLife.50342.

MacQueen, J. (Jan. 1967). "Some methods for classification and analysis of multivariate observations". In: *Proceedings of the Fifth Berkeley Symposium on Mathematical Statistics and Probability, Volume 1: Statistics*. Publisher: University of California Press, pp. 281–297.

Maréchal, Valérie et al. (Nov. 2001). "Human Immunodeficiency Virus Type 1 Entry into Macrophages Mediated by Macropinocytosis". In: *Journal of Virology* 75.22. Publisher: American Society for Microbiology, pp. 11166–11177. DOI: 10.1128/jvi.75.22.11166-11177.2001.

Mellström, Karin, Carl-Henrik Heldin, and Bengt Westermark (Aug. 1988). "Induction of circular membrane ruffling on human fibroblasts by platelet-derived growth factor". In: *Exp. Cell Res.* 177.2, pp. 347–359. ISSN: 00144827. DOI: 10.1016/0014-4827(88)90468-5.

Mercer, Jason and Ari Helenius (May 2009). "Virus entry by macropinocytosis." In: *Nat. Cell Biol.* 11.5, pp. 510–20. ISSN: 1476-4679. DOI: 10.1038/ncb0509-510.

Meza, Isaura and Margaret Clarke (2004). "Dynamics of endocytic traffic of Entamoeba histolytica revealed by confocal microscopy and flow cytometry". en. In: *Cell Motility* 59.4. _eprint: https://onlinelibrary.wiley.com/doi/pdf/10.1002/cm.20038, pp. 215–226. ISSN: 1097-0169. DOI: 10.1002/cm.20038.

Mogilner, A. and G. Oster (Dec. 1996). "Cell motility driven by actin polymerization". eng. In: *Biophysical Journal* 71.6, pp. 3030–3045. ISSN: 0006-3495. DOI: 10.1016/S0006-3495(96)79496-1.

Mogilner, Alex and George Oster (Mar. 2003). "Force generation by actin polymerization II: the elastic ratchet and tethered filaments". eng. In: *Biophysical Journal* 84.3, pp. 1591–1605. ISSN: 0006-3495. DOI: 10.1016/S0006-3495(03)74969-8.

Mullins, R. Dyche, John A. Heuser, and Thomas D. Pollard (May 1998). "The interaction of Arp2/3 complex with actin: Nucleation, high affinity pointed end capping, and formation of branching networks of filaments". In: *Proceedings of the National Academy of Sciences* 95.11. Publisher: Proceedings of the National Academy of Sciences, pp. 6181–6186. DOI: 10.1073/pnas.95.11.6181.

Nagumo, J., S. Arimoto, and S. Yoshizawa (Oct. 1962). "An Active Pulse Transmission Line Simulating Nerve Axon". In: *Proceedings of the IRE* 50.10. Conference Name: Proceedings of the IRE, pp. 2061–2070. ISSN: 2162-6634. DOI: 10.1109/JRPROC.1962.288235.

Oliver, T., M. Dembo, and K. Jacobson (1995). "Traction forces in locomoting cells". eng. In: *Cell Motility and the Cytoskeleton* 31.3, pp. 225–240. ISSN: 0886-1544. DOI: 10.1002/cm.970310306.

Oliver, T., J. Lee, and K. Jacobson (June 1994). "Forces exerted by locomoting cells". eng. In: *Seminars in Cell Biology* 5.3, pp. 139–147. ISSN: 1043-4682. DOI: 10.1006/scel.1994.1018.

Orth, James D and Mark A McNiven (Dec. 2006). "Get off my back! Rapid receptor internalization through circular dorsal ruffles." In: *Cancer Res.* 66.23, pp. 11094–11096. ISSN: 0008-5472. DOI: 10.1158/0008-5472.CAN-06-3397.

Ostap, E. Michael et al. (2003). "Dynamic localization of myosin-I to endocytic structures in Acanthamoeba". en. In: *Cell Motility* 54.1. _eprint: https://onlinelibrary.wiley.com/doi/pdf/10.1002/cm.10081, pp. 29–40. ISSN: 1097-0169. DOI: 10.1002/cm.10081.

Paddenberg, R et al. (2001). "Serum withdrawal induces a redistribution of intracellular gelsolin towards F-actin in NIH 3T3 fibroblasts preceding apoptotic cell death." In: *Eur. J. Cell Biol.* 80.5, pp. 366–378. ISSN: 0171-9335.

Park, Seungman, Yoon Ki Joo, and Yun Chen (Sept. 2018). "Dynamic adhesion characterization of cancer cells under blood flow-mimetic conditions: effects of cell shape and orientation on drag force". en. In: *Microfluidics and Nanofluidics* 22.10, p. 108. ISSN: 1613-4990. DOI: 10.1007/s10404-018-2132-7.

Peleg, Barak et al. (Jan. 2011). "Propagating cell-membrane waves driven by curved activators of actin polymerization". In: *PLoS One* 6.4, e18635. ISSN: 19326203. DOI: 10.1371/journal.pone.0018635.

Peskin, C S, G M Odell, and G F Oster (July 1993). "Cellular motions and thermal fluctuations: the Brownian ratchet." In: *Biophysical Journal* 65.1, pp. 316–324. ISSN: 0006-3495.

Pierce, Glenn F. et al. (1991). "Role of platelet-derived growth factor in wound healing". en. In: *Journal of Cellular Biochemistry* 45.4, pp. 319–326. ISSN: 1097-4644. DOI: 10.1002/jcb.240450403.

Pirkmajer, Sergej and Alexander V Chibalin (Aug. 2011). "Serum starvation: caveat emptor." In: *Am. J. Physiol. Cell Physiol.* 301.2, pp. C272–9. ISSN: 1522-1563. DOI: 10.1152/ajpcell.00091.2011.

Radon, J. (Dec. 1986). "On the determination of functions from their integral values along certain manifolds". In: *IEEE Transactions on Medical Imaging* 5.4. Conference Name: IEEE Transactions on Medical Imaging, pp. 170–176. ISSN: 1558-254X. DOI: 10.1109/TMI.1986.4307775.

Ronneberger, Olaf, Philipp Fischer, and Thomas Brox (2015). "U-Net: Convolutional Networks for Biomedical Image Segmentation". en. In: *Medical Image Computing and Computer-Assisted Intervention – MICCAI 2015*. Ed. by Nassir Navab et al. Lecture Notes in Computer Science. Springer International Publishing, pp. 234–241. ISBN: 978-3-319-24574-4.

Rosales-Reyes, Roberto et al. (June 2012). "Salmonella infects B cells by macropinocytosis and formation of spacious phagosomes but does not induce pyroptosis in favor of its survival". en. In: *Microbial Pathogenesis* 52.6, pp. 367–374. ISSN: 0882-4010. DOI: 10.1016/j.micpath.2012.03.007.

Rottner, Klemens et al. (Oct. 2017). "Actin assembly mechanisms at a glance". In: *Journal of Cell Science* 130.20, pp. 3427–3435. ISSN: 0021-9533. DOI: 10.1242/jcs.206433.

Rousseeuw, Peter J. (Nov. 1987). "Silhouettes: A graphical aid to the interpretation and validation of cluster analysis". en. In: *Journal of Computational and Applied Mathematics* 20, pp. 53–65. ISSN: 0377-0427. DOI: 10.1016/0377-0427(87)90125-7.

Ruthel, Gordon and Gary Banker (1998). "Actin-dependent anterograde movement of growth-cone-like structures along growing hippocampal axons: A novel form of axonal transport?" en. In: *Cell Motility* 40.2. _eprint: https://onlinelibrary.wiley.com/doi/pdf/10.1002/%28SICI%291097-0169%281998%2940%3A2%3C160%3A%3AAID-CM5%3E3.0.CO%3B2-J, pp. 160–173. ISSN: 1097-0169. DOI: 10.1002/(SICI)1097-0169(1998)40:2<160::AID-CM5>3.0.CO;2-J.

Seroussi, I. et al. (Aug. 2012). "Segmentation and tracking of live cells in phase-contrast images using directional gradient vector flow for snakes". In: *J. Microsc.* 247.2, pp. 137–146. ISSN: 00222720. DOI: 10.1111/j.1365-2818.2012.03624.x.

Sharp, Kendra V. et al. (2002). "Liquid Flows in Microchannels". In: *MEMS Handb.*, pp. 6.1–6.38. DOI: 10.1016/j.ijheatmasstransfer.2004.12.019.

Streets, Aaron M and Yanyi Huang (Jan. 2013). "Chip in a lab: Microfluidics for next generation life science research." In: *Biomicrofluidics* 7.1, p. 11302. ISSN: 1932-1058. DOI: 10.1063/1.4789751.

Strogatz, Steven H. and Ronald F. Fox (June 1995). *Nonlinear Dynamics and Chaos: With Applications to Physics, Biology, Chemistry and Engineering*. Vol. 48. ISBN: 0-8133-4910-9.

Suetsugu, Shiro et al. (Oct. 2003). "Differential Roles of WAVE1 and WAVE2 in Dorsal and Peripheral Ruffle Formation for Fibroblast Cell Migration". In: *Dev. Cell* 5.4, pp. 595–609. ISSN: 1534-5807. DOI: 10.1016/S1534-5807(03)00297-1.

Swanson, Joel A (2008). "Shaping cups into phagosomes and macropinosomes." In: *Nat. Rev. Mol. Cell Biol.* 9.8, pp. 639–49. ISSN: 1471-0080. DOI: 10.1038/nrm2447.

Tallquist, Michelle and Andrius Kazlauskas (Aug. 2004). "PDGF signaling in cells and mice". en. In: *Cytokine & Growth Factor Reviews*. Platelet-derived Growth Factor 15.4, pp. 205–213. ISSN: 1359-6101. DOI: 10.1016/j.cytogfr.2004.03.003.

Ter-Pogossian, Michel M. (Apr. 1977). "Basic principles of computed axial tomography". en. In: *Seminars in Nuclear Medicine* 7.2, pp. 109–127. ISSN: 0001-2998. DOI: 10.1016/S0001-2998(77)80013-5.

Théry, Manuel and Matthieu Piel (July 2009). "Adhesive micropatterns for cells: A microcontact printing protocol". In: *Cold Spring Harb. Protoc.* 4.7, pdb.prot5255. ISSN: 15596095. DOI: 10.1101/pdb.prot5255.

Turing, Alan Mathison (Aug. 1952). "The chemical basis of morphogenesis". In: *Philosophical Transactions of the Royal Society of London. Series B, Biological Sciences* 237.641. Publisher: Royal Society, pp. 37–72. DOI: 10.1098/rstb.1952.0012.

Ukidave, Y. et al. (Apr. 2013). "Quantifying the energy efficiency of FFT on heterogeneous platforms". In: *2013 IEEE International Symposium on Performance Analysis of Systems and Software (ISPASS)*, pp. 235–244. DOI: 10.1109/ISPASS.2013.6557174.

Van Aelst, L. and C. D'Souza-Schorey (Sept. 1997). "Rho GTPases and signaling networks." In: *Genes Dev.* 11.18, pp. 2295–2322. ISSN: 0890-9369. DOI: 10.1101/gad.11.18.2295.

Vanag, Vladimir K. and Irving R. Epstein (Mar. 2004). "Stationary and Oscillatory Localized Patterns, and Subcritical Bifurcations". In: *Physical Review Letters* 92.12. Publisher: American Physical Society, p. 128301. DOI: 10.1103/PhysRevLett.92.128301.

Vicker, Michael G. (Apr. 2002). "Eukaryotic Cell Locomotion Depends on the Propagation of Self-Organized Reaction–Diffusion Waves and Oscillations of Actin Filament Assembly". en. In: *Experimental Cell Research* 275.1, pp. 54–66. ISSN: 0014-4827. DOI: 10.1006/excr.2001.5466.

Warrick, Jay et al. (Mar. 2007). "High-throughput microfluidics: improved sample treatment and washing over standard wells." en. In: *Lab Chip* 7.3, pp. 316–321. ISSN: 1473-0197. DOI: 10.1039/b613350a.

Welliver, Timothy P et al. (2011). "Ruffles limit diffusion in the plasma membrane during macropinosome formation." In: *J. Cell Sci.* 124.Pt 23, pp. 4106–14. ISSN: 1477-9137. DOI: 10.1242/jcs.091538.

Whitesides, George M (July 2006). "The origins and the future of microfluidics." In: *Nature* 442.7101, pp. 368–373. ISSN: 0028-0836. DOI: 10.1038/nature05058.

Xu, Chenyang and Jerry L. Prince (1998a). "Generalized gradient vector flow external forces for active contours". In: *Signal Processing* 71, pp. 131–139. DOI: 10.1016/S0165-1684(98)00140-6.

– (1998b). "Snakes, shapes, and gradient vector flow". In: *Image Process. IEEE Trans.* 7.3, pp. 359–369.

Xuan, L. and Z. Hong (Nov. 2017). "An improved canny edge detection algorithm". In: *2017 8th IEEE International Conference on Software Engineering and Service Science (ICSESS)*. ISSN: 2327-0594, pp. 275–278. DOI: 10.1109/ICSESS.2017.8342913.

Yoshida, Sei et al. (Nov. 2018). "Dorsal ruffles enhance activation of Akt by growth factors". en. In: *J Cell Sci* 131.22, jcs220517. ISSN: 0021-9533, 1477-9137. DOI: 10/gfpnn4.

Young, M. E., P. A. Carroad, and R. L. Bell (May 1980). "Estimation of diffusion coefficients of proteins". In: *Biotechnol. Bioeng.* 22.5, pp. 947–955. ISSN: 0006-3592. DOI: 10.1002/bit.260220504.

Zeng, Yukai et al. (Nov. 2011). "Investigating Circular Dorsal Ruffles through Varying Substrate Stiffness and Mathematical Modeling". In: *Biophys. J.* 101.9, pp. 2122–2130. ISSN: 0006-3495. DOI: 10.1016/J.BPJ.2011.09.047.